

LA-UR-11-11460
 NT@UW-11-16
 IFIC/11-57
 FTUV/11-1007
 NPAC-11-14

Probing Novel Scalar and Tensor Interactions from (Ultra)Cold Neutrons to the LHC

Tanmoy Bhattacharya¹, Vincenzo Cirigliano¹, Saul D. Cohen^{2,5},
 Alberto Filipuzzi³, Martín González-Alonso⁴,
 Michael L. Graesser¹, Rajan Gupta¹, Huey-Wen Lin⁵

¹ Theoretical Division, Los Alamos National Laboratory, Los Alamos, NM 87545, USA

²Center for Computational Science, Boston University, Boston, MA 02123, USA

³Departament de Física Teòrica, IFIC, Universitat de València – CSIC
 Apt. Correus 22085, E-46071 València, Spain

⁴Department of Physics, University of Wisconsin-Madison,
 1150 University Ave., Madison, WI, 53706, USA

⁵Department of Physics, University of Washington, Seattle, WA 98195, USA

November 1, 2011

Abstract

Scalar and tensor interactions were once competitors to the now well-established $V - A$ structure of the Standard Model weak interactions. We revisit these interactions and survey constraints from low-energy probes (neutron, nuclear, and pion decays) as well as collider searches. Currently, the most stringent limit on scalar and tensor interactions arise from $0^+ \rightarrow 0^+$ nuclear decays and the radiative pion decay $\pi \rightarrow e\nu\gamma$, respectively. For the future, we find that upcoming neutron beta decay and LHC measurements will compete in setting the most stringent bounds. For neutron beta decay, we demonstrate the importance of lattice computations of the neutron-to-proton matrix elements to setting limits on these interactions, and provide the first lattice estimate of the scalar charge and a new average of existing results for the tensor charge. Data taken at the LHC is currently probing these interactions at the 10^{-2} level (relative to the standard weak interactions), with the potential to reach the $\lesssim 10^{-3}$ level. We show that, with some theoretical assumptions, the discovery of a charged spin-0 resonance decaying to an electron and missing energy implies a lower limit on the strength of scalar interactions probed at low energy.

1 Introduction

Nuclear and neutron beta decays have historically played a central role in determining the $V-A$ structure of weak interactions and in shaping what we now call the Standard Model (SM) [1, 2]. Nowadays, precision measurements of low-energy processes such as neutron decay can be used to probe the existence of non-SM interactions, such as novel scalar and tensor structures. Considerable experimental efforts using both cold and ultracold neutrons are underway worldwide, with the aim to improve the precision of various neutron decay observables [3, 4]: lifetime [5, 6, 7, 8, 9], beta asymmetry A [10, 11, 12, 13] neutrino asymmetry B [14, 12], electron-neutrino correlation a [15, 16, 17], and Fierz interference term b [15, 18]. In some of the asymmetry measurements there are prospects to reach experimental sensitivities between 10^{-3} and 10^{-4} ; this makes these observables very interesting probes of new physics effects originating at the TeV scale that have expected size $(v/\Lambda_{\text{BSM}})^2$, where $v = (2\sqrt{2}G_F)^{-1/2} \approx 174$ GeV and Λ_{BSM} denotes the mass scale where physics beyond the Standard Model (BSM) appears.

The overall goal of this work is to assess the discovery potential and discriminating power of planned precision beta-decay measurements with cold and ultracold neutrons. In particular we wish to study the sensitivity of neutron decay to new physics in the context of and in competition with: (i) other low-energy precision measurements in nuclear beta decays and pion decays; and (ii) high-energy collider searches (Tevatron, LHC). In order to achieve our goal, we work within an effective field theory (EFT) setup, in which the dynamical effects of new heavy BSM degrees of freedom are parameterized by local operators of dimension higher than four built with SM fields. In the absence of a clear new-physics signal from collider searches, we find this way of proceeding the most attractive and general: all specific model analyses of beta decays (see Ref. [19] for a discussion within supersymmetry) can be cast in the EFT language and the constraints on effective operators that we will derive can be readily converted into constraints on the parameters of any SM extension.

Among various BSM contributions we identify new scalar and tensor operators involving left-handed neutrinos as the most promising to probe with neutron decay, because they interfere with the SM amplitude and thus contribute at *linear* order to decay parameters. Motivated by this, in the unified EFT framework we present a comprehensive analysis of constraints on such scalar and tensor BSM interactions from a broad range of low-energy probes (neutron decay, nuclear decays, pion decays) as well as collider searches.¹ To our knowledge such an analysis is missing in the literature, despite being essential to judging the relative merits of various low-energy experiments.

Extracting bounds on short-distance scalar and tensor couplings from neutron and nuclear beta decays requires knowledge of the nucleon scalar and tensor form factors at zero momentum transfer, denoted here by $g_{S,T}$. In previous beta-decay studies, g_S and g_T have been assumed to be $O(1)$ based on quark-model estimates (see, for example, Ref. [20]). The importance of the hadronic form factors can be appreciated by considering the extreme case in which $g_{S,T} \ll 1$, which would dilute the sensitivity of beta decays to new physics. Concerning the hadronic form factors, the main results of this work are:

¹The EFT analysis of collider searches is valid as long as the particles that mediate the new interactions are above threshold for production at colliders.

- We provide the first lattice-QCD estimate of g_S and a new average of existing g_T results. Current lattice uncertainties are at the level of 50% for g_S and 35% for g_T . This already enables much improved phenomenology (see for example Fig. 9).
- We show that a precision of 20% in g_S will be needed to take full advantage of 10^{-3} -level neutron-decay measurements. We identify and discuss the key systematic effects that need to be brought under control in order to achieve $\delta g_S/g_S \sim 20\%$.

Besides the new estimates of g_S and g_T with lattice QCD (LQCD), the main new findings of our analysis can be summarized as follows:

- Currently, the most stringent constraints on the scalar and tensor effective couplings (denoted by ϵ_S and ϵ_T) arise from low-energy probes. ϵ_S is constrained by $0^+ \rightarrow 0^+$ nuclear beta decays, while ϵ_T is constrained by the Dalitz-plot analysis of the radiative pion decay $\pi \rightarrow e\nu\gamma$. There are also potentially very strong constraints on $\epsilon_{S,T}$ from the ratio of $\pi \rightarrow e\nu$ to $\pi \rightarrow \mu\nu$ decay rates. This constraint arises from operator mixing: once a scalar or tensor interaction is generated by new physics, SM radiative corrections will generate an effective pseudoscalar operator that mediates the helicity-suppressed mode $\pi \rightarrow e\nu$. If the flavor structure of the SM extension is known, this constraint could be the strongest.
- Future neutron-decay measurements of the Fierz interference term b and the analogue term b_ν in the neutrino asymmetry B can greatly improve existing constraints on tensor interactions: precision levels $\delta b, \delta b_\nu \sim 10^{-3}$ would provide a four-fold or higher improvement in the bound (depending on the sign of ϵ_T), as shown in Figs. 2 and 9. On the other hand, $\delta b, \delta b_\nu \sim 10^{-4}$ -level measurements would improve current bounds on ϵ_T by one order of magnitude and current bounds on ϵ_S by a factor of two (see Fig. 3).
- Current collider bounds from the LHC are not yet competitive with low-energy constraints (see Fig. 10). Folding in the current uncertainty on g_S , the LHC bounds on ϵ_S and ϵ_T are weaker by a factor of about 4 and 3, respectively, than those obtained from nuclear decays and $\pi \rightarrow e\nu\gamma$.
- Future LHC results, based on higher center-of-mass energy and higher integrated luminosity, would definitely improve on current low-energy bounds on $\epsilon_{S,T}$, and would compete with improved low-energy constraints based on $\delta b, \delta b_\nu \sim 10^{-3}$ in future neutron-decay measurements (see Fig. 11).
- Finally, we have explored the possibility that a mediator of new scalar interactions can be produced at the LHC. In this case, the EFT approach breaks down at collider energies and we have derived a general correlation between production cross-section for a scalar resonance at colliders and new-physics signal in neutron decay. This correlation links the discovery of a scalar resonance in $pp \rightarrow e\nu + X$ at the LHC with a lower bound (i.e. guaranteed signal) on ϵ_S . This is illustrated in Figs. 12, 13, and 14.

The paper is organized as follows. In Section 2 we present the effective theory description of low-energy charged-current processes and briefly discuss how the coefficients may be constrained. In Section 3 we explain our notation for the matrix elements required to describe the neutron beta decay and discuss how this decay constrains the parameters in the effective field theory. In Section 4, we discuss the low-energy phenomenological constraints on chirality-violating scalar and tensor operators in the effective Lagrangian. Section 5 discusses current and planned lattice analyses for the matrix elements of the quark bilinear structures $\bar{u}\Gamma d$ between neutron and proton states, with special emphasis on the scalar and tensor structures. We provide the first estimate of g_S from lattice QCD and a new average of existing calculations of g_T . In Section 6 we summarize the impact of lattice estimates of $g_{S,T}$ on the phenomenology of scalar and tensor BSM interactions. In Section 7, we present the constraints on the short-distance couplings obtained from an analysis of high-energy scattering experiments and discuss the improvement expected in the next few years. We present our concluding remarks in Section 8. Two appendices provide details of the operators contributing to charged-current processes and of the neutron-decay differential decay distribution.

2 Effective theory description of low-energy charged-current processes

Following Ref. [21], we describe new physics contributions to low-energy charged-current (CC) processes in a model-independent effective-theory setup, paying special attention to neutron-decay observables and their interplay with other low-energy and collider measurements.

We parameterize the effect of new degrees of freedom and interactions beyond the SM via a series of higher-dimensional operators constructed with low-energy SM fields, assuming the existence of a mass gap between the SM and its ultraviolet completion. If the SM extension is weakly coupled, the resulting TeV-scale effective Lagrangian linearly realizes the electroweak (EW) symmetry $SU(2)_L \times U(1)_Y$ and contains a SM-like Higgs doublet [22]. We also assume that potential right-handed neutrino fields (sterile with respect to the SM gauge group) are heavy compared to the weak scale and therefore have been integrated out of the low-energy effective theory. This method is quite general and allows us to study the implications of precision measurements on a large class of models.

In our analysis we truncate the expansion of the effective Lagrangian to the lowest non-trivial order, given by dimension-six operators. The contribution from the dimension-six operators to physical amplitudes involves terms proportional to $v^2/\Lambda_{\text{BSM}}^2$ and $E^2/\Lambda_{\text{BSM}}^2$, where $v = \langle \varphi^0 \rangle \approx 174 \text{ GeV}$ is the vacuum expectation value (VEV) of the Higgs field and E is the characteristic energy scale of a given process. We will work to linear order in these ratios of scales.

2.1 Effective Lagrangian

In Ref. [21] a minimal basis of $SU(2) \times U(1)$ invariant dimension-six operators contributing to low-energy charged-current processes was identified (see Appendix A for details).

Denoting with Λ_i the effective dimensionful coupling associated with the operator O_i , we can write the effective Lagrangian as

$$\mathcal{L}^{(\text{eff})} = \mathcal{L}_{\text{SM}} + \sum_i \frac{1}{\Lambda_i^2} O_i \longrightarrow \mathcal{L}_{\text{SM}} + \frac{1}{v^2} \sum_i \hat{\alpha}_i O_i, \quad \text{with } \hat{\alpha}_i = \frac{v^2}{\Lambda_i^2}, \quad (1)$$

where in the last step we have set the correct dimensions by the Higgs VEV v and defined the dimensionless new-physics couplings $\hat{\alpha}_i$, which are $\mathcal{O}(10^{-3})$ for $\Lambda_i \sim \text{TeV}$.

In this framework one can derive the low-scale $\mathcal{O}(1 \text{ GeV})$ effective Lagrangian for semi-leptonic transitions. It receives contributions from both W -exchange diagrams (with modified W -fermion couplings) and the four-fermion operators $O_{lq}^{(3)}$, O_{qde} , O_{lq} , O_{lq}^t defined in Appendix A. This matching procedure leads to [21]

$$\begin{aligned} \mathcal{L}_{\text{CC}} = & \frac{-g^2}{2M_W^2} V_{ij} \left[\left(1 + [v_L]_{\ell\ell ij} \right) \bar{\ell}_L \gamma_\mu \nu_{\ell L} \bar{u}_L^i \gamma^\mu d_L^j + [v_R]_{\ell\ell ij} \bar{\ell}_L \gamma_\mu \nu_{\ell L} \bar{u}_R^i \gamma^\mu d_R^j \right. \\ & + [s_L]_{\ell\ell ij} \bar{\ell}_R \nu_{\ell L} \bar{u}_R^i d_L^j + [s_R]_{\ell\ell ij} \bar{\ell}_R \nu_{\ell L} \bar{u}_L^i d_R^j \\ & \left. + [t_L]_{\ell\ell ij} \bar{\ell}_R \sigma_{\mu\nu} \nu_{\ell L} \bar{u}_R^i \sigma^{\mu\nu} d_L^j \right] + \text{h.c.} . \end{aligned} \quad (2)$$

where we use $\sigma^{\mu\nu} = i[\gamma^\mu, \gamma^\nu]/2$. The SM effective Lagrangian corresponds to $v_L = v_R = s_L = s_R = t_L = 0$. The effective couplings $v_L, v_R, s_L, s_R, t_L \sim v^2/\Lambda_i^2$ are functions of the coupling $\hat{\alpha}_i$ of $SU(2) \times U(1)$ invariant weak-scale operators. While their explicit expressions can be found in Appendix A, here we simply point out two important features:

- v_L involves a linear combination of three weak-scale effective couplings: a quark-gauge boson vertex correction, a lepton-gauge boson vertex correction, and a four-fermion operator coupling left-handed quarks and leptons (same chirality structure as the SM). An important consequence is that by $SU(2) \times U(1)$ gauge invariance, v_L is related to Z^0 fermion-antifermion vertex corrections and neutral-current four-fermion vertices.
- v_R and s_L, s_R, t_L are in one-to-one correspondence with weak-scale effective couplings. v_R describes a right-handed charged-current quark coupling, while s_L, s_R, t_L correspond to scalar and tensor four-quark operators. Again, $SU(2)$ gauge invariance implies that these couplings mediate not only charged-current processes but also processes such as $\bar{e}e \leftrightarrow \bar{u}u, \bar{d}d$, with scalar or tensor Dirac structure.

In what follows, we will work in the limit in which the effective non-standard couplings $v_{L,R}$, $s_{L,R}$, and t_L are real and we will focus only on CP-even observables (for a discussion of CP-odd observables refer to Ref. [20]). To simplify the notation, we will omit flavor indices, e.g. $[v_L]_{eeud} \rightarrow v_L$. In addition, we will use the tree-level definition of the Fermi constant $g^2/(8M_W^2) \equiv G_F^{(0)}/\sqrt{2}$. Working to linear order in the non-standard couplings, and focusing on the $ij = ud$ component, the semi-leptonic effective Lagrangian can be

written in the following useful form:

$$\begin{aligned}\mathcal{L}_{\text{CC}} = & -\frac{G_F^{(0)} V_{ud}}{\sqrt{2}} \left(1 + \epsilon_L + \epsilon_R\right) \left[\bar{\ell} \gamma_\mu (1 - \gamma_5) \nu_\ell \cdot \bar{u} \left[\gamma^\mu - (1 - 2\epsilon_R) \gamma^\mu \gamma_5 \right] d \right. \\ & \left. + \bar{\ell} (1 - \gamma_5) \nu_\ell \cdot \bar{u} \left[\epsilon_S - \epsilon_P \gamma_5 \right] d + \epsilon_T \bar{\ell} \sigma_{\mu\nu} (1 - \gamma_5) \nu_\ell \cdot \bar{u} \sigma^{\mu\nu} (1 - \gamma_5) d \right] + \text{h.c.}, \quad (3)\end{aligned}$$

where we have defined the effective scalar, pseudoscalar, and tensor couplings as follows:

$$\epsilon_{L,R} \equiv v_{L,R} \quad \epsilon_S \equiv s_L + s_R \quad \epsilon_P \equiv s_L - s_R \quad \epsilon_T \equiv t_L. \quad (4)$$

While the physical amplitudes are renormalization scale and scheme independent, the individual effective couplings ϵ_i and hadronic matrix elements can display a strong scale dependence. Throughout the paper, we will quote estimates and bounds for the ϵ_i at the renormalization scale $\mu = 2$ GeV in the $\overline{\text{MS}}$ scheme, unless otherwise specified.

The Lagrangian (3) mediates all low-energy charged-current weak processes involving up and down quarks. For a recent analysis of flavor-dependent constraints, see Ref. [23]. In some of the charged-current processes involving first-generation quarks the theoretical and experimental precision has reached or will reach in the near future a level that allows stringent bounds on the new-physics effective couplings. In this work we are interested in assessing the sensitivity of neutron decay to new physics in the context of (i) other low-energy constraints from nuclear beta decays and pion decays; and (ii) constraints from high-energy colliders (LEP, Tevatron, LHC). To set the stage for the discussion, we summarize the observables that give us access to the couplings appearing in Eq. (3) (we will come back in detail to these in following sections):

- The combination $(\epsilon_L + \epsilon_R)$ affects the overall normalization of the effective Fermi constant. This is phenomenologically accessible through quark-lepton universality tests (precise determination of V_{ud} from $0^+ \rightarrow 0^+$ nuclear decays under the assumption that $G_F = G_\mu$, where G_μ is the Fermi constant extracted from muon decay). An extensive analysis of the constraints on $(\epsilon_L + \epsilon_R)$ from universality tests and precision electroweak observables from the Z -pole was performed in Ref. [21], within BSM scenarios with minimal flavor violation. In this context it was shown that constraints from low-energy are at the same level or stronger (depending on the operator) than from Z -pole observables and $e^+ e^- \rightarrow q\bar{q}$ cross-section measurements at LEP.
- The right-handed coupling ϵ_R affects the relative normalization of the axial and vector currents. In neutron decay ϵ_R can be reabsorbed in a redefinition of the axial coupling and experiments are only sensitive to the combination $(1 - 2\epsilon_R)g_A/g_V$ (g_V and g_A are the vector and axial form factors at zero momentum transfer, to be precisely defined below). Disentangling ϵ_R requires precision measurements of $(1 - 2\epsilon_R)g_A/g_V$ and precision calculations of g_A/g_V in LQCD.
- The effective pseudoscalar combination $\epsilon_P \equiv s_L - s_R$ contributes to leptonic decays of the pion. It is strongly constrained by the helicity-suppressed ratio

$R_\pi \equiv \Gamma(\pi \rightarrow e\nu[\gamma])/\Gamma(\pi \rightarrow \mu\nu[\gamma])$. Moreover, as discussed in Refs. [24, 25, 26], the low-energy coupling ϵ_P receives contributions proportional to $\epsilon_{S,T}$ through electroweak radiative corrections. We will discuss the resulting constraints on $\epsilon_{S,P,T}$ in Section 4.1.4.

- Both the scalar combination $\epsilon_S \equiv s_L + s_R$ and the tensor coupling $\epsilon_T \equiv t_L$ contribute at linear order to the Fierz interference terms in beta decays of neutrons and nuclei, and the neutrino-asymmetry correlation coefficient B in polarized neutron and nuclear decay (see Appendix B for notation). Because of the peculiar way in which the Fierz interference term appears in many asymmetry measurements, bounds on ϵ_S and ϵ_T can also be obtained by observation of the beta-asymmetry correlation coefficient A , electron-neutrino correlation a , and positron polarization measurements in various nuclear beta decays. Finally, the tensor coupling ϵ_T can also be constrained through Dalitz-plot studies of the radiative pion decay $\pi \rightarrow e\nu\gamma$.
- All of the above operators can provide signatures at colliders. Currently there are no competitive collider bounds on the chirality-flipping scalar and tensor couplings $\epsilon_{S,P,T}$, because their interference with the SM amplitude carries factors of m_f/E_f (where m_f is a light fermion mass, $f \in \{e, u, d\}$), which at collider energies strongly suppresses the whole effect. So we immediately see that low-energy physics provides a unique opportunity to probe these couplings, to which collider searches are sensitive only quadratically (i.e. via non-interference terms). We will derive in Section 7 the current bounds on $\epsilon_{S,T}$ from searches at the LHC, and we will show that with higher center-of-mass energy and integrated luminosity they will become competitive with low-energy searches.

Next, we review the analysis of neutron decay in the SM and beyond within the EFT framework described above.

3 Neutron β decay

The amplitude for neutron decay $n(p_n) \rightarrow p(p_p)e^-(p_e)\bar{\nu}_e(p_\nu)$ mediated by the effective Lagrangian (3) involves in principle the matrix elements between the neutron and proton of all possible quark bilinears. These can be parameterized in terms of Lorentz-invariant

form factors as follows [27]:

$$\langle p(p_p) | \bar{u} \gamma_\mu d | n(p_n) \rangle = \bar{u}_p(p_p) \left[g_V(q^2) \gamma_\mu + \frac{\tilde{g}_{T(V)}(q^2)}{2M_N} \sigma_{\mu\nu} q^\nu + \frac{\tilde{g}_S(q^2)}{2M_N} q_\mu \right] u_n(p_n) \quad (5a)$$

$$\langle p(p_p) | \bar{u} \gamma_\mu \gamma_5 d | n(p_n) \rangle = \bar{u}_p(p_p) \left[g_A(q^2) \gamma_\mu + \frac{\tilde{g}_{T(A)}(q^2)}{2M_N} \sigma_{\mu\nu} q^\nu + \frac{\tilde{g}_P(q^2)}{2M_N} q_\mu \right] \gamma_5 u_n(p_n) \quad (5b)$$

$$\langle p(p_p) | \bar{u} d | n(p_n) \rangle = g_S(q^2) \bar{u}_p(p_p) u_n(p_n) \quad (5c)$$

$$\langle p(p_p) | \bar{u} \gamma_5 d | n(p_n) \rangle = g_P(q^2) \bar{u}_p(p_p) \gamma_5 u_n(p_n) \quad (5d)$$

$$\begin{aligned} \langle p(p_p) | \bar{u} \sigma_{\mu\nu} d | n(p_n) \rangle &= \bar{u}_p(p_p) \left[g_T(q^2) \sigma_{\mu\nu} + g_T^{(1)}(q^2) (q_\mu \gamma_\nu - q_\nu \gamma_\mu) \right. \\ &\quad \left. + g_T^{(2)}(q^2) (q_\mu P_\nu - q_\nu P_\mu) + g_T^{(3)}(q^2) (\gamma_\mu \not{q} \gamma_\nu - \gamma_\nu \not{q} \gamma_\mu) \right] u_n(p_n) \end{aligned} \quad (5e)$$

where $u_{p,n}$ are the proton and neutron spinor amplitudes, $P = p_n + p_p$, $q = p_n - p_p$ is the momentum transfer, and $M_N = M_n = M_p$ denotes a common nucleon mass.² Note that all the above spinor contractions are $O(1)$, except for $\bar{u}_p \gamma_5 u_n$ which is $O(q/M_N)$. Moreover, as discussed below, second-class current contributions \tilde{g}_S and $\tilde{g}_{T(A)}$ affect the amplitude at levels below the expected experimental sensitivities.

Our goal here is to identify TeV-induced new physics contaminations to the amplitude of typical size $\epsilon_{P,S,T} \sim (v/\Lambda_{\text{BSM}})^2 \sim 10^{-3}$. The effect we are after is of the same size as recoil corrections $q/M_N \sim 10^{-3}$ as well as radiative corrections α/π . So in our analysis we perform a simultaneous expansion in new physics contributions, recoil, and radiative corrections keeping terms up to first order and neglecting higher-order terms, as they are smaller than the current and planned experimental sensitivity. In light of this simultaneous expansion in $\epsilon_{P,S,T}$, q/M_N , and α/π , we now discuss contributions from all quark-bilinear operators:

- **Vector current:** The form factor $g_V(0)$ contributes at $O(1)$ to the amplitude and $\tilde{g}_{T(V)}(0)$ contributes at first order in q/M_N . Also, up to isospin-breaking corrections of order $(M_n - M_p)/M_N \sim q/M_N$, the weak magnetism form factor $\tilde{g}_{T(V)}(0)$ can be related to the difference of proton and neutron magnetic moments, that are well known. On the other hand, the induced-scalar form factor $\tilde{g}_S(q^2)$ vanishes in the isospin limit [27], so it is of order $(M_n - M_p)/M_N \sim q/M_N$. Since it multiplies one power of q_μ/M_N , its contribution to the amplitude is effectively second order in the recoil expansion, so we drop it.
- **Axial current:** From the axial current only $g_A(0)$ contributes up to first order. The induced-tensor form factor $\tilde{g}_{T(A)}(q^2)$ vanishes in the isospin limit [27], and since it multiplies one power of q_μ/M_N its contribution to the amplitude is of

²In the case of vector and axial bilinears, the induced tensor term proportional to $\sigma_{\mu\nu} q^\nu$ can be traded for an independent “scalar” form factor proportional to P_μ . Here we choose to follow the parameterization of Ref. [27].

second order in q/M_N , so we drop it. Similarly, the contribution associated with the induced-pseudoscalar form factor \tilde{g}_P is quadratic in our counting, because the pseudoscalar bilinear is itself of order q/M_N , and it comes with an explicit q/M_N suppression, so we neglect it.³

- **Pseudoscalar bilinear:** The pseudoscalar bilinear $\bar{u}_p \gamma_5 u_n$ is itself of order q/M_N . Since it necessarily multiplies a new-physics effective coupling ϵ_P (there is no pseudoscalar coupling in the SM), this term is also of second order in our expansion, and we drop it.
- **Scalar and tensor bilinears:** These bilinears enter into the analysis multiplied by new-physics effective couplings $\epsilon_{S,T}$. So we need the matrix elements to zeroth order in the recoil expansion, which leaves us with $g_S(0)$ and $g_T(0)$. $g_T^{(1,2,3)}(q^2)$ are all multiplied by one power of q and $g_T^{(3)}$ vanishes in the isospin limit [27].

In summary, to the order we are working, the amplitudes depend only on $g_i \equiv g_i(0)$ ($i \in \{V, A, S, T\}$) and $\tilde{g}_{T(V)}(0)$. Up to second-order corrections in isospin breaking, one has $g_V = 1$ [29, 30]. For notational convenience, it is also useful to define the ratio of the axial to vector form factors as $\lambda \equiv g_A/g_V$. As noted earlier, in presence of non-standard right-handed interactions the axial form factor is always multiplied by the correction factor $(1 - 2\epsilon_R)$, so that the neutron-decay amplitude is actually a function of $\tilde{\lambda} \equiv \lambda(1 - 2\epsilon_R)$.

Finally, in order to make contact with the existing standard references on neutron and nuclear beta-decay phenomenology [31, 32, 2], let us note here that Eq. (5) can be viewed as the matching conditions from our quark-level effective theory Eq. (3) to a nucleon-level effective theory, such as the one originally written down by Lee and Yang [31]. The Lee-Yang effective couplings C_i, C'_i ($i \in \{V, A, S, T\}$) can be expressed in terms of our parameters as

$$C_i = \frac{G_F}{\sqrt{2}} V_{ud} \bar{C}_i \quad (6a)$$

$$\bar{C}_V = g_V (1 + \epsilon_L + \epsilon_R) \quad (6b)$$

$$\bar{C}_A = -g_A (1 + \epsilon_L - \epsilon_R) \quad (6c)$$

$$\bar{C}_S = g_S \epsilon_S \quad (6d)$$

$$\bar{C}_T = 4 g_T \epsilon_T , \quad (6e)$$

with $C'_i = C_i$, since we only have left-handed neutrinos in our low-energy effective theory. Operators involving right-handed neutrinos do not interfere with the SM amplitude and therefore contribute at second order to all observables. An analysis involving such operators will be presented elsewhere [33]. Finally, notice that Ref. [20] defines the couplings $C_A, C'_{V,S,T}$ with an overall minus sign compared to ours.

³This effect is, however, enhanced. Using partially conserved axial current one can show that the form factor \tilde{g}_P is of order $M_N/m_q \sim 100$, making the contribution to the amplitude of order 10^{-4} . In Section 5.4 we review the status of experimental data and LQCD calculations showing this enhancement. The effect of \tilde{g}_P on the neutron beta-decay rate has been worked out in Ref. [28], and it should be included when the experiments reach that level of precision.

3.1 Differential decay distribution

Including the effect of recoil corrections, radiative corrections, and BSM couplings, the differential decay rate for polarized neutrons reads [34, 35, 36, 37]

$$\frac{d\Gamma}{dE_e d\Omega_e d\Omega_\nu} = \frac{(G_F^{(0)})^2 |V_{ud}|^2}{(2\pi)^5} (1 + 2\epsilon_L + 2\epsilon_R) \left(1 + 3\tilde{\lambda}^2\right) \cdot w(E_e) \cdot D(E_e, \mathbf{p}_e, \mathbf{p}_\nu, \boldsymbol{\sigma}_n), \quad (7)$$

where \mathbf{p}_e and \mathbf{p}_ν denote the electron and neutrino three-momenta, while $\boldsymbol{\sigma}_n$ denotes the neutron polarization. The bulk of the electron spectrum is described by

$$w(E_e) = p_e E_e (E_0 - E_e)^2 F(Z=1, E_e) \left(1 + \frac{\alpha}{2\pi} e_V^R + \frac{\alpha}{2\pi} \delta_\alpha^{(1)}(E_e)\right) \quad (8)$$

where $E_0 = \Delta - (\Delta^2 - m_e^2)/(2M_n)$ (with $\Delta = M_n - M_p$) is the electron endpoint energy, m_e is the electron mass, and $F(Z, E_e)$ is the Fermi function that captures the Coulomb radiative corrections (Z denotes the charge of the daughter nucleus, which coincides with the proton in this case). The function $\delta_\alpha^{(1)}(E_e)$ [36, 37] captures model-independent (“outer”) radiative corrections, while the coupling e_V^R is sensitive to the short-distance (“inner”) radiative correction [38, 36]. The differential decay distribution function $D(E_e, \mathbf{p}_e, \mathbf{p}_\nu, \boldsymbol{\sigma}_n)$ is given by [36, 37]

$$\begin{aligned} D(E_e, \mathbf{p}_e, \mathbf{p}_\nu, \boldsymbol{\sigma}_n) &= 1 + c_0 + c_1 \frac{E_e}{M_N} + \frac{m_e \bar{b}}{E_e} + \bar{a}(E_e) \frac{\mathbf{p}_e \cdot \mathbf{p}_\nu}{E_e E_\nu} + \bar{A}(E_e) \frac{\boldsymbol{\sigma}_n \cdot \mathbf{p}_e}{E_e} \\ &+ \bar{B}(E_e) \frac{\boldsymbol{\sigma}_n \cdot \mathbf{p}_\nu}{E_\nu} + \bar{C}_{(aa)}(E_e) \left(\frac{\mathbf{p}_e \cdot \mathbf{p}_\nu}{E_e E_\nu}\right)^2 + \bar{C}_{(aA)}(E_e) \frac{\mathbf{p}_e \cdot \mathbf{p}_\nu}{E_e E_\nu} \frac{\boldsymbol{\sigma}_n \cdot \mathbf{p}_e}{E_e} \\ &+ \bar{C}_{(aB)}(E_e) \frac{\mathbf{p}_e \cdot \mathbf{p}_\nu}{E_e E_\nu} \frac{\boldsymbol{\sigma}_n \cdot \mathbf{p}_\nu}{E_\nu}, \end{aligned} \quad (9)$$

where \bar{b} is an effective Fierz interference term and $\bar{a}(E_e)$, $\bar{A}(E_e)$, $\bar{B}(E_e)$ and $\bar{C}_{aa,aA,aB}(E_e)$ are effective energy-dependent correlation coefficients, whose full expressions [36, 37, 39] we report in Appendix B, where one can also find the coefficients $c_{0,1}$ generated by recoil corrections.⁴ In absence of radiative corrections, recoil corrections and BSM contributions, the effective correlation coefficients $\bar{a}(E_e)$, $\bar{A}(E_e)$ and $\bar{B}(E_e)$ reduce to the following well-known leading-order expressions

$$\bar{a}(E_e) \rightarrow \frac{1 - \lambda^2}{1 + 3\lambda^2}, \quad \bar{A}(E_e) \rightarrow \frac{2\lambda(1 - \lambda)}{1 + 3\lambda^2}, \quad \bar{B}(E_e) \rightarrow \frac{2\lambda(1 + \lambda)}{1 + 3\lambda^2}, \quad (10)$$

with the rest of coefficients ($c_{0,1}, \bar{b}, \bar{C}_{aa,aA,aB}(E_e)$) vanishing in this limit.

The impact of new-physics contributions can be summarized as follows:

- The effect of $\epsilon_{L/R}$ was already evident from the effective Lagrangian of Eq. 3: they induce (i) an overall correction proportional to $(1 + 2\epsilon_L + 2\epsilon_R)$, and (ii) the shift $\lambda \rightarrow \tilde{\lambda} = \lambda(1 - 2\epsilon_R)$. As a consequence of this second effect, working to linear order

⁴ See also Ref. [40] for a discussion of recoil corrections to the proton asymmetry.

in new-physics contributions, the measurements of different correlation coefficients by themselves cannot disentangle λ and ϵ_R ; they simply provide independent measures of $\tilde{\lambda}$. In order to probe ϵ_R from correlation measurements, one needs to independently know g_A/g_V from LQCD calculations.

- The scalar and tensor interactions $\epsilon_{S,T}$ appear to linear order only through the Fierz interference term \bar{b} and the analogue term b_ν in the neutrino-asymmetry parameter (b_ν is the part of $\bar{B}(E_e)$ proportional to m_e/E_e , see Appendix B for a precise definition)

$$b^{\text{BSM}} = \frac{2}{1+3\lambda^2} \left[g_S \epsilon_S - 12\lambda g_T \epsilon_T \right] \approx 0.34 g_S \epsilon_S - 5.22 g_T \epsilon_T , \quad (11a)$$

$$b_\nu^{\text{BSM}} = \frac{2}{1+3\lambda^2} \left[g_S \epsilon_S \lambda - 4g_T \epsilon_T (1+2\lambda) \right] \approx 0.44 g_S \epsilon_S - 4.85 g_T \epsilon_T . \quad (11b)$$

To the order we are working, in the above expressions we can use either λ or $\tilde{\lambda}$.

Experimentally, one can probe the new-physics contributions in $\tilde{\lambda}$, b^{BSM} , and b_ν^{BSM} through (i) measurements of the electron spectrum, aimed to isolate the term \bar{b} in Eq. (9); or (ii) correlation measurements, aimed to isolate $\bar{a}(E_e)$, $\bar{A}(E_e)$, and $\bar{B}(E_e)$ in Eq. (9). Correlation measurements involve the construction of asymmetry ratios [35]. For example, in order to isolate $\bar{A}(E_e)$ one constructs the ratio $A_{\text{exp}}(E_e) = (N_+(E_e) - N_-(E_e))/(N_+(E_e) + N_-(E_e))$ where $N_\pm(E_e)$ are the spectra corresponding to events with $\boldsymbol{\sigma}_n \cdot \mathbf{p}_e > 0$ and $\boldsymbol{\sigma}_n \cdot \mathbf{p}_e < 0$. Similarly, in order to isolate $\bar{B}(E_e)$ one can use the simple ratio $B_{\text{exp}}(E_e) = (Q_{++}(E_e) - Q_{--}(E_e))/(Q_{++}(E_e) + Q_{--}(E_e))$, where $Q_{++}(E_e)$ and $Q_{--}(E_e)$ are the spectra of events with $\boldsymbol{\sigma}_n \cdot \mathbf{p}_e > 0$, $\boldsymbol{\sigma}_n \cdot \mathbf{p}_p > 0$ and $\boldsymbol{\sigma}_n \cdot \mathbf{p}_e < 0$, $\boldsymbol{\sigma}_n \cdot \mathbf{p}_p < 0$, respectively. One can immediately see that through the total spectra in the denominator, both $A_{\text{exp}}(E_e)$ and $B_{\text{exp}}(E_e)$ are sensitive to the Fierz interference term \bar{b} , so that asymmetry measurements involving simple ratios as described above really measure

$$\tilde{Y}(E_e) = \frac{\bar{Y}(E_e)}{1 + \bar{b} m_e/E_e} , \quad (12)$$

where $Y \in \{A, B, a, \dots\}$. Moreover, each individual experiment applies optimization cuts in E_e , thus measuring a specific weighted average of Eq. (12).

The above observation has important consequences for the phenomenology of neutron decay: (i) The m_e/E_e component of $B_{\text{exp}}(E_e)$ is sensitive not to b_ν^{BSM} but rather to the combination $(1+3\lambda^2)/(2\lambda(1+\lambda)) b_\nu^{\text{BSM}} - b^{\text{BSM}} \approx b_\nu^{\text{BSM}} - b^{\text{BSM}}$. Besides $B_{\text{exp}}(E_e)$, it might be possible to construct a set of observables that disentangle the contribution of b^{BSM} and b_ν^{BSM} [41]. In this case the BSM sensitivity of b_ν^{BSM} alone is of interest. In our phenomenological analysis we will study both cases (constraints from $b_\nu^{\text{BSM}} - b^{\text{BSM}}$ and b_ν^{BSM}). (ii) More generally, correlation coefficients measurements traditionally used to determine $\lambda = g_A/g_V$ within the SM ($\epsilon_{L/R} = 0, b = b_\nu = 0$), provide information on three independent parameters in our EFT setup: $\tilde{\lambda} = \lambda(1-2\epsilon_R)$, b^{BSM} , and b_ν^{BSM} .⁵

⁵ In other words, if $\epsilon_{S,T}$ are larger than the experimental errors, one has to observe an unexpected

A fit to the current data [42, 43, 44, 45] (with precision $\delta A/A \sim 0.005$, $\delta a/a \sim 0.05$, $\delta B/B \sim 0.005$) yields $-0.3 < b^{\text{BSM}}, b_\nu^{\text{BSM}} < 0.5$ at the 95% C.L. [4], which, as we will see, is not competitive with other bounds. It will be interesting, however, to explore the implications of future experimental improvements in the combined extraction of $\tilde{\lambda}$, b^{BSM} and b_ν^{BSM} from a , A , and B measurements, along the lines described in Refs. [4, 46].

The main conclusion from the above discussion is that measurements of the differential neutron-decay distribution are mostly sensitive to new physics through b^{BSM} and b_ν^{BSM} , which depend on the scalar and tensor couplings, ϵ_S and ϵ_T , to linear order. Therefore, apart from the next section, which we include for completeness, in the rest of this paper we restrict our discussion on these exotic scalar and tensor interactions, comparing the physics reach of neutron decay to other low-energy and collider probes.

3.2 Total decay rate and determination of V_{ud}

For completeness, we discuss here the BSM corrections to the neutron decay rate and the extraction of V_{ud} from neutron decay. Expressing $G_F^{(0)}$ in terms of the Fermi constant determined in muon decay G_μ (this involves non-standard contributions to the purely leptonic charged-current interaction encoded in the coefficient \tilde{v}_L [21]) and performing the phase-space integrations, the total decay rate reads

$$\Gamma = \frac{G_\mu^2 |V_{ud}|^2 m_e^5}{2\pi^3} \left(1 + 3\tilde{\lambda}^2\right) \cdot f \cdot (1 + \Delta_{\text{RC}}) \left[1 + 2\epsilon_L - 2\tilde{v}_L + 2\epsilon_R + b^{\text{BSM}} \frac{I_1(x_0)}{I_0(x_0)}\right]. \quad (13)$$

In the above expression, the corrections from BSM physics are encoded in $\tilde{\lambda}$ and the terms in square brackets. $\Delta_{\text{RC}} = 3.90(8) \times 10^{-2}$ is the SM electroweak radiative correction [38], and the phase-space integrals are defined by

$$I_k(x_0) = \int_1^{x_0} x^{1-k} (x_0 - x)^2 \sqrt{x^2 - 1} dx \quad f = I_0(x_0)(1 + \Delta_f), \quad (14)$$

where $x_0 = E_0/m_e$ and Δ_f encodes Coulomb and recoil corrections that are numerically quite important, $I_0(x_0) = 1.629$, $f = 1.6887$, $I_1(x_0)/I_0(x_0) = 0.652$ (See Ref. [38] for details). In order to extract V_{ud} from neutron decays one needs (see Eq. 13) experimental input on the neutron lifetime $1/\Gamma$ [47, 48] and $\tilde{\lambda}$, which is usually extracted from beta-asymmetry $A_{\text{exp}}(E_e)$ measurements [42, 43] (after accounting for recoil and radiative corrections). Taking into account Eq. (12), the usual method for extracting $\tilde{\lambda}$ actually determines $\tilde{\lambda}(1 + c b^{\text{BSM}})$, where c is a certain $O(1)$ number that depends on the specific experimental analysis. In summary what we really extract from neutron beta decay is

energy dependence of the form m/E in the measurements of the correlation coefficients (in addition to the various expected energy dependences due to sub-leading standard effects that are detailed in Appendix B). Thus, for a certain energy, a determination of λ from $a(A)$ would be actually extracting the quantity $\tilde{\lambda}(1 + n_{a(A)} b^{\text{BSM}} m/E)$, whereas in a B -based determination of λ , we would have $\tilde{\lambda}(1 + n_B(b_\nu^{\text{BSM}} - b^{\text{BSM}})m/E)$, where $n_a = \frac{(1-\lambda^2)(1+3\lambda^2)}{8\lambda^2} \approx -0.28$, $n_A = -\frac{(1-\lambda)(1+3\lambda^2)}{(1+\lambda)(1-3\lambda)} \approx -0.25$ and $n_B = \frac{(1+\lambda)(1+3\lambda^2)}{(1-\lambda)(1+3\lambda)} \approx -10.2$.

not V_{ud} but the combination

$$\begin{aligned} |V_{ud}|^2 \Big|_{n \rightarrow p e \bar{\nu}} &= |V_{ud}|^2 \left[1 + 2\epsilon_L - 2\tilde{v}_L + 2\epsilon_R + b^{\text{BSM}} \left(\frac{I_1(x_0)}{I_0(x_0)} - \frac{6\lambda^2}{1+3\lambda^2} c \right) \right] \\ &\approx |V_{ud}|^2 \left[1 + 2\epsilon_L - 2\tilde{v}_L + 2\epsilon_R + b^{\text{BSM}} (0.65 - 1.66 c) \right]. \end{aligned} \quad (15)$$

4 Low-energy phenomenology of scalar and tensor interactions

4.1 Other probes of scalar and tensor interactions

In order to assess the discovery potential of experiments planning to measure \bar{b} and \tilde{B} at the level of 10^{-3} and 10^{-4} , it is crucial to identify existing constraints on new scalar and tensor operators. As we discuss below in some detail, the most stringent constraint on the scalar coupling ϵ_S arises from $0^+ \rightarrow 0^+$ nuclear beta decays. On the other hand, the most stringent bound on the tensor effective coupling ϵ_T arises from the Dalitz-plot study of the radiative pion decay $\pi \rightarrow e\nu\gamma$. For completeness, we will also briefly review (i) constraints on $\epsilon_{S,T}$ from other nuclear beta-decay observables, showing that they are not competitive at the moment; and (ii) constraints on $\epsilon_{S,P,T}$ arising from the helicity-suppressed $\pi \rightarrow e\nu$ decay. As we will show, the latter provides potentially the strongest constraints on $\epsilon_{S,T}$, once the flavor structure of the underlying theory is known. This provides very stringent constraints on model building.

4.1.1 $0^+ \rightarrow 0^+$ transitions and scalar interactions

At leading order within the SM and new physics, the differential decay rate for an unpolarized nucleus is [32]

$$\begin{aligned} \frac{d\Gamma_{0^+ \rightarrow 0^+}}{dE_e d\Omega_e d\Omega_\nu} &= 2 \frac{(G_F^{(0)})^2 |V_{ud}|^2}{(2\pi)^5} (1 + 2\epsilon_L + 2\epsilon_R) p_e E_e (\tilde{E}_0 - E_e)^2 F(-Z, E_e) \\ &\times \left\{ 1 + a_{0^+} \frac{\mathbf{p}_e \cdot \mathbf{p}_\nu}{E_e E_\nu} + b_{0^+} \frac{m_e}{E_e} \right\} \end{aligned} \quad (16)$$

where $\tilde{E}_0 = M_P - M_D$ is the electron endpoint energy expressed in terms of the masses of parent and daughter nuclei, $F(-Z, E_e)$ is the Fermi function, Z is the atomic number of the daughter nucleus (the minus sign applies to β^+ emitters for which the most precise measurements exist). For $0^+ \rightarrow 0^+$ transitions the coefficients a, b are

$$a_{0^+} = 1 \quad (17a)$$

$$b_{0^+} = -2\gamma g_S \epsilon_S \quad \gamma = \sqrt{1 - \alpha^2 Z^2}, \quad (17b)$$

and the total rate is given by

$$\Gamma_{0^+ \rightarrow 0^+} = \frac{G_\mu^2 |V_{ud}|^2 m_e^5}{\pi^3} f_{0^+ \rightarrow 0^+} \left(1 + \Delta_{\text{RC}}^{(0^+ \rightarrow 0^+)} \right) \left[1 + 2\epsilon_L - 2\tilde{v}_L + 2\epsilon_R + b_{0^+} \frac{I_1(\tilde{x}_0)}{I_0(\tilde{x}_0)} \right] \quad (18)$$

where $\tilde{x}_0 = \tilde{E}_0/m_e$. In this last expression, the SM sub-effects have been included through $\Delta_{\text{RC}}^{(0^+ \rightarrow 0^+)}$ and also inside $f_{0^+ \rightarrow 0^+}$, that up to Coulomb, nuclear distortion and recoil effects, is $f_{0^+ \rightarrow 0^+} = I_0(\tilde{x}_0)$, similarly to what happens in the neutron-decay case. The various radiative corrections (including $\Delta_{\text{RC}}^{(0^+ \rightarrow 0^+)}$) are discussed in detail in Refs. [49, 50]. Comparing the values of V_{ud} as extracted from neutron and nuclear decays, we find (see Eq. (15) and the preceding discussion)

$$\frac{|V_{ud}^{0^+ \rightarrow 0^+}|^2}{|V_{ud}^{n \rightarrow p e \bar{\nu}}|^2} = 1 + b_{0^+}^{\text{BSM}} \frac{I_1(\tilde{x}_0)}{I_0(\tilde{x}_0)} - b_n^{\text{BSM}} \left(\frac{I_1(x_0)}{I_0(x_0)} - \frac{6\lambda^2}{1+3\lambda^2} c \right), \quad (19)$$

which in principle provides another handle on scalar and tensor interactions.

Let us now come to the point of greatest interest for this paper's discussion. From a comparison of precisely known half-lives corrected by phase-space factors $f_{0^+ \rightarrow 0^+}$, Hardy and Towner [50] found $b_{0^+} = -0.0022(26)$, which translates into the following bound on the product of nucleon scalar form factor and short-distance scalar coupling:

$$-1.0 \times 10^{-3} < g_S \epsilon_S < 3.2 \times 10^{-3} \quad (90\% \text{ C.L.}) . \quad (20)$$

This is the most stringent bound on scalar interactions from low-energy probes.

4.1.2 Radiative pion decay and the tensor interaction

An analysis of the Dalitz plot of the radiative pion decay $\pi^+ \rightarrow e^+ \nu_e \gamma$ is sensitive to the same tensor operator that can be probed in beta decays. The experimental results from the PIBETA collaboration [51] put constraints on the product $\epsilon_T \times f_T$ of the short-distance coupling ϵ_T and the hadronic form factor f_T defined by [52]

$$\langle \gamma(\epsilon, p) | \bar{u} \sigma_{\mu\nu} \gamma_5 d | \pi^+ \rangle = -\frac{e}{2} f_T (p_\mu \epsilon_\nu - p_\nu \epsilon_\mu) , \quad (21)$$

where p_μ and ϵ_μ are the photon four-momentum and polarization vector, respectively. The analysis of Ref. [52], based on a large- N_c -inspired resonance-saturation model provides $f_T = 0.24(4)$ at the renormalization scale $\mu = 1$ GeV, with parametric uncertainty induced by the uncertainty in the quark condensate. The 90%-C.L. experimental constraint⁶ $-2.0 \times 10^{-4} < \epsilon_T \times f_T < 2.6 \times 10^{-4}$, when combined with the above estimate for f_T run to 2 GeV implies

$$-1.1 \times 10^{-3} < \epsilon_T < 1.36 \times 10^{-3} \quad (90\% \text{ C.L.}) . \quad (22)$$

Again, this is the most stringent constraint on the tensor coupling from low-energy experiments. The next best constraints, which we report in the next section, arise from measurements of nuclear beta decays.

⁶Note that there is a factor of 2 difference in the normalization of the tensor coupling ϵ_T compared to what was used in Refs. [25, 51].

4.1.3 Bounds on scalar and tensor structures from other nuclear beta decays

Bounds on scalar and tensor interactions can be obtained from a number of observables in nuclear beta decays, other than $0^+ \rightarrow 0^+$ transitions. Although these bounds are currently not competitive, we summarize them here for completeness.

The leading sensitivity to scalar and tensor operators appears through the Fierz interference term b , which in the limit of pure Gamow-Teller transitions is proportional to the tensor coupling ($b_{\text{GT}} = -(8\gamma g_T \epsilon_T)/\lambda$), while in pure Fermi transitions is proportional to the scalar coupling ($b_F = 2\gamma g_S \epsilon_S$). Significant constraints on b arise from electron-polarization observables [32] as well as in measurements of \tilde{A} and \tilde{a} in both Fermi and Gamow-Teller transitions. Here is a summary of current bounds on $\epsilon_{S,T}$:

- The most stringent constraint from the beta asymmetry in pure Gamow-Teller transitions (\tilde{A}_{GT}) arises from ${}^{60}\text{Co}$ measurements and implies [53]

$$-2.9 \times 10^{-3} < g_T \epsilon_T < 1.5 \times 10^{-2} \quad (90\% \text{ C.L.}) . \quad (23)$$

Similar bounds can be obtained from measurements of \tilde{A}_{GT} in ${}^{114}\text{In}$ decay [54]: $-2.2 \times 10^{-2} < g_T \epsilon_T < 1.3 \times 10^{-2}$ (90 % C.L.).

- Measurements of the ratio P_F/P_{GT} of longitudinal polarization in the positron emitted in pure Fermi and Gamow-Teller transitions [55, 56] imply

$$-0.76 \times 10^{-2} < g_S \epsilon_S + \frac{4}{\lambda} g_T \epsilon_T < 1.0 \times 10^{-2} \quad (90\% \text{ C.L.}) . \quad (24)$$

- Preliminary results have been reported on the measurement of the longitudinal polarization of positrons emitted by polarized ${}^{107}\text{In}$ nuclei [57]. The corresponding 90 % C.L. sensitivity to tensor interactions, $|g_T \epsilon_T| < 3.1 \times 10^{-3}$, is quite promising although not yet competitive with the radiative pion decay.
- Finally, the beta-neutrino correlation a has been measured in a number of nuclear transitions [58, 59, 60, 61]. The resulting constraints on scalar and tensor interactions are nicely summarized in Fig. 7 of Ref. [58]. In terms of the coupling constants used here, the 90 % C.L. combined bound on the tensor interaction reads $|g_T \epsilon_T| < 5 \times 10^{-3}$, again not competitive with the radiative pion decay.

We observe that in order to improve on the existing bound on ϵ_T from $\pi \rightarrow e\nu\gamma$, future measurements sensitive to b_{GT} should aim at sensitivities of $\delta b_{\text{GT}} \lesssim 6.3 \times g_T \times 10^{-3}$. For example, a 10^{-3} measurement of b_{GT} would probe $g_T \epsilon_T$ at the 2×10^{-4} -level, providing a very competitive bound.

4.1.4 Constraints on $\epsilon_{S,P,T}$ from $\pi \rightarrow e\nu$

The ratio $R_\pi \equiv \Gamma(\pi \rightarrow e\nu[\gamma])/\Gamma(\pi \rightarrow \mu\nu[\gamma])$ probes more than just the effective low-energy pseudoscalar coupling ϵ_P defined earlier as the coefficient of the operator $\bar{e}(1 - \gamma_5)\nu_e \cdot \bar{u}\gamma_5 d$. In fact, since (i) R_π is defined as the ratio of electron-to-muon decay and

(ii) the neutrino flavor in both the decays is not observed, this observable is sensitive to the whole set of parameters $\epsilon_P^{\alpha\beta}$ defined by

$$\mathcal{L}_{\text{eff}} \supset \frac{G_F}{\sqrt{2}} V_{ud} \epsilon_P^{\alpha\beta} \bar{e}_\alpha (1 - \gamma_5) \nu_\beta \cdot \bar{u} \gamma_5 d , \quad (25)$$

where $\alpha \in \{e, \mu\}$ refers to the flavor of the charged lepton and $\beta \in \{e, \mu, \tau\}$ refers to the neutrino flavor. One generically expects SM extensions to generate non-diagonal components in $\epsilon_{P,S,T}^{\alpha\beta}$. In the new notation the previously defined pseudoscalar, scalar, and tensor couplings reads $\epsilon_{P,S,T} \equiv \epsilon_{P,S,T}^{ee}$. It is important to note here that only ϵ_P^{ee} and $\epsilon_P^{\mu\mu}$ can interfere with the SM amplitudes, while the remaining $\epsilon_P^{\alpha\beta}$ contribute incoherently to both the numerator and denominator in R_π .⁷ In summary, allowing for non-standard interactions and factoring out the SM prediction for R_π , one can write⁸:

$$\frac{R_\pi}{R_\pi^{\text{SM}}} = \frac{\left[\left(1 - \frac{B_0}{m_e} \epsilon_P^{ee} \right)^2 + \left(\frac{B_0}{m_e} \epsilon_P^{e\mu} \right)^2 + \left(\frac{B_0}{m_e} \epsilon_P^{e\tau} \right)^2 \right]}{\left[\left(1 - \frac{B_0}{m_\mu} \epsilon_P^{\mu\mu} \right)^2 + \left(\frac{B_0}{m_\mu} \epsilon_P^{\mu e} \right)^2 + \left(\frac{B_0}{m_\mu} \epsilon_P^{\mu\tau} \right)^2 \right]} . \quad (26)$$

In the above equation the factors of $B_0/m_{e,\mu} \epsilon_P$ represent the ratio of new-physics amplitude over SM amplitude. The latter is proportional to the charged-lepton mass due to angular-momentum conservation arguments, while the former is proportional to $\langle 0 | \bar{u} \gamma_5 d | \pi \rangle$, characterized by the scale- and scheme-dependent parameter⁹

$$B_0(\mu) \equiv \frac{M_\pi^2}{m_u(\mu) + m_d(\mu)} . \quad (27)$$

Since $B_0^{\overline{\text{MS}}}(1 \text{ GeV}) = 1.85 \text{ GeV}$ and consequently $B_0/m_e = 3.6 \times 10^3$, R_π has enhanced sensitivity to $\epsilon_P^{\alpha\beta}$, and one needs to keep quadratic terms in these new physics coefficients.¹⁰

Inspection of Eq. (26) reveals that if the new-physics couplings respect $\epsilon_P^{e\alpha}/m_e = \epsilon_P^{\mu\alpha}/m_\mu$, then $R_\pi/R_\pi^{\text{SM}} = 1$, and there are no constraints on these couplings. On the other hand, if the effective couplings $\epsilon_P^{\alpha\beta}$ are all of similar size, one can neglect the entire denominator in Eq. (26), as it is suppressed with respect to the numerator by powers of m_e/m_μ . We will assume to be in this second scenario. In this case the constraint in Eq. (26) forces the couplings $\epsilon_P^{ee}, \epsilon_P^{e\mu}, \epsilon_P^{e\tau}$ to live in a spherical shell of radius $m_e/B_0 \sqrt{R_\pi^{\text{exp}}/R_\pi^{\text{SM}}} \approx 2.75 \times 10^{-4}$ centered at $\epsilon_P^{ee} = m_e/B_0 \approx 2.75 \times 10^{-4}$, $\epsilon_P^{e\mu} = \epsilon_P^{e\tau} = 0$.

⁷ While in our setup the incoherent contribution arises from “wrong-flavor” neutrinos, in general it could have a different nature. For example, the incoherent contribution to R_π discussed in Refs. [25, 20] is due to a right-handed light neutrino.

⁸Here we are neglecting the overall effect of $v_{L/R}$, not enhanced by helicity arguments.

⁹Note that the scale and scheme dependence of $B_0(\mu)$ is compensated in physical quantities by the scale and scheme dependence of the Wilson coefficients $\epsilon_P^{\alpha\beta}$.

¹⁰This feature is specific to purely leptonic decays of pseudoscalar mesons. In beta decays one never encounters relative enhancement factors such as B/m_e , because ϵ_P is always multiplied by nucleon velocity factors and the SM amplitude does not suffer anomalous suppression (as the helicity argument implies in the case of $\pi \rightarrow e\nu$).

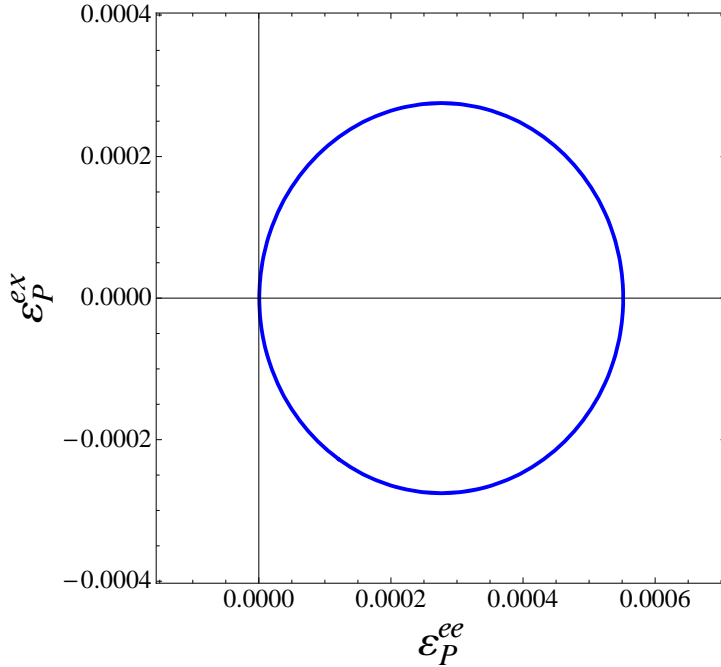


Figure 1: The allowed region in the two-dimensional plane ϵ_P^{ee} - ϵ_P^{ex} determined by R_π is given by an annulus of thickness 1.38×10^{-6} . In the absence of information on ϵ_P^{ex} , the 90 % C.L. bound on ϵ_P^{ee} is $-1.4 \times 10^{-7} < \epsilon_P^{ee} < 5.5 \times 10^{-4}$.

The thickness of the shell is numerically 1.38×10^{-6} and is determined by the current combined uncertainty in R_π^{exp} [62, 63] and R_π^{SM} [64, 65]: $R_\pi^{\text{exp}}/R_\pi^{\text{SM}} = 0.996(5)$ (90% C.L.). This is illustrated in Fig. 1, where we plot the allowed region in the two-dimensional plane given by ϵ_P^{ee} and a generic “wrong-flavor” coupling denoted by ϵ_P^{ex} . Note that the allowed region is given by the thickness of the curve in the figure, thus enforcing a strong correlation between ϵ_P^{ee} and ϵ_P^{ex} . Since $\epsilon_P^{\alpha \neq \beta}$ are essentially unconstrained by other measurements and can be of order 10^{-3} , we can marginalize over either one of the couplings to obtain a bound on the other. The resulting 90%-C.L. bounds are

$$-1.4 \times 10^{-7} < \epsilon_P^{ee} < 5.5 \times 10^{-4}, \quad \text{or} \quad -2.75 \times 10^{-4} < \epsilon_P^{e\alpha} < 2.75 \times 10^{-4} \quad (\alpha \neq e), \quad (28)$$

in qualitative agreement with the findings of Refs. [25, 20].

As originally discussed in Refs. [24, 25, 26], the pseudoscalar coupling ϵ_P^{ee} can be radiatively generated starting from nonzero $\epsilon_{S,T}$. Hence, the stringent constraint in Eq. (28) puts constraints on the same $\epsilon_{S,T}$ that can be probed in beta decays. The physics of this effect is very simple: once the scalar, pseudoscalar, and tensor operators are generated by some non-standard physics at the matching scale Λ , electroweak radiative corrections induce mixing among these three operators. So even if one engineers a small pseudoscalar contribution $\epsilon_P(\Lambda)$ at the matching scale, known SM physics generates a nonzero $\epsilon_P(\mu)$ at some lower energy scale μ via loop diagrams. The general form of the constraint can be worked out by using the three-operator mixing results from Ref. [26]¹¹.

¹¹The authors of Ref. [26] focused only on the phenomenology of scalar-to-pseudoscalar mixing.

The leading-order result is

$$\epsilon_P^{\alpha\beta}(\mu) = \epsilon_P^{\alpha\beta}(\Lambda) \left(1 + \gamma_{PP} \log \frac{\Lambda}{\mu} \right) + \epsilon_S^{\alpha\beta}(\Lambda) \gamma_{SP} \log \frac{\Lambda}{\mu} + \epsilon_T^{\alpha\beta}(\Lambda) \gamma_{TP} \log \frac{\Lambda}{\mu} \quad (29a)$$

$$\gamma_{PP} = \frac{3}{4} \frac{\alpha_2}{\pi} + \frac{113}{72} \frac{\alpha_1}{\pi} \approx 1.3 \times 10^{-2} \quad (29b)$$

$$\gamma_{SP} = \frac{15}{72} \frac{\alpha_1}{\pi} \approx 6.7 \times 10^{-4} \quad (29c)$$

$$\gamma_{TP} = -\frac{9}{2} \frac{\alpha_2}{\pi} - \frac{15}{2} \frac{\alpha_1}{\pi} \approx -7.3 \times 10^{-2}, \quad (29d)$$

where $\alpha_1 = \alpha / \cos^2 \theta_W$ and $\alpha_2 = \alpha / \sin^2 \theta_W$ are the $U(1)$ and $SU(2)$ weak couplings, expressed in terms of the fine-structure constant and the weak mixing angle. Setting $\epsilon_P^{ee}(\Lambda) = 0$ and neglecting the small $O(\alpha/\pi)$ fractional difference between $\epsilon_{S,T}(\Lambda)$ and the observable $\epsilon_{S,T}(\mu)$ at the low scale, the 90% C.L. constraint on the ϵ_S - ϵ_T plane reads

$$\frac{-1.4 \times 10^{-7}}{\log(\Lambda/\mu)} < \gamma_{SP} \epsilon_S + \gamma_{TP} \epsilon_T < \frac{5.5 \times 10^{-4}}{\log(\Lambda/\mu)}. \quad (30)$$

Even assuming $\log(\Lambda/\mu) \sim 10$ (e.g. $\Lambda \sim 10$ TeV and $\mu \sim 1$ GeV), using the numerical values of $\gamma_{SP,TP}$, one can verify that the individual constraints are at the level of $|\epsilon_S| \lesssim 8 \times 10^{-2}$ and $|\epsilon_T| \lesssim 10^{-3}$, implying that this constraint on ϵ_T is roughly equivalent to the one arising from $\pi \rightarrow e\nu\gamma$. Of course, these bounds become logarithmically more stringent as the new-physics scale Λ grows.

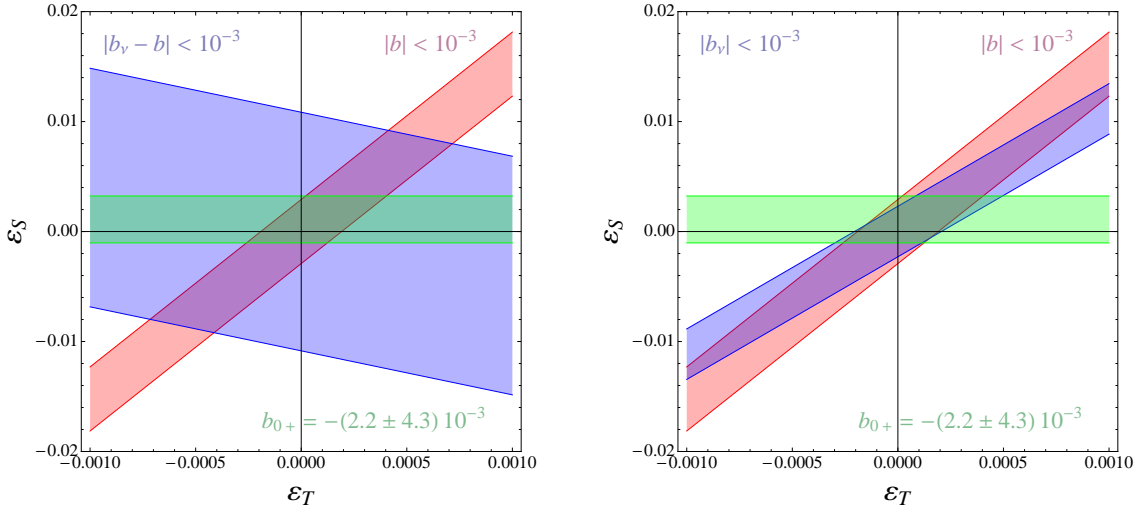


Figure 2: 90% C.L. allowed regions in the ϵ_S - ϵ_T plane implied by (i) the existing bound on b_{0+} (green horizontal band); (ii) projected 10^{-3} -level limits on b (red band), $b_\nu - b$ (blue band, left panel), and b_ν (blue band, right panel). The hadronic form factors are taken to be $g_S = g_T = 1$ in the ideal scenario of no uncertainty. The impact of hadronic uncertainties is discussed in Section 6.

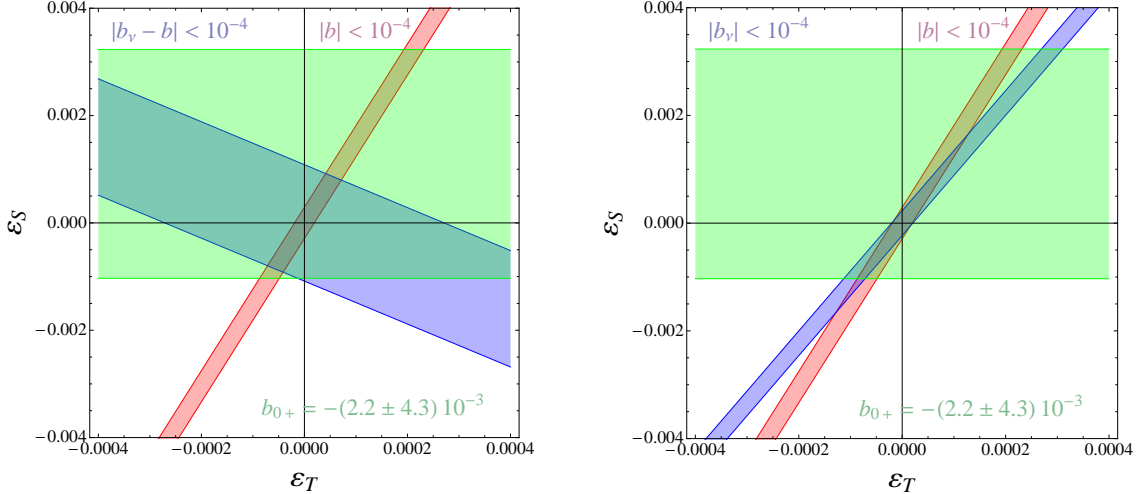


Figure 3: 90% C.L. allowed regions in the ϵ_S - ϵ_T plane implied by (i) the existing bound on b_{0+} (green horizontal band); (ii) projected 10^{-4} -level limits on b (red band), $b_\nu - b$ (blue band, left panel), and b_ν (blue band, right panel). The hadronic form factors are taken to be $g_S = g_T = 1$ in the ideal scenario of no uncertainty. The impact of hadronic uncertainties is discussed in Section 6.

4.2 The impact of future b and B neutron measurements

The discussion in the preceding subsection has shown that currently the most stringent low-energy constraints on novel scalar and tensor interactions arise, respectively, from the Fierz interference term in $0^+ \rightarrow 0^+$ nuclear beta decays (Eq. (20)) and from the radiative pion decay $\pi \rightarrow e\nu\gamma$ (Eq. (22)). It is important to realize that the allowed ϵ_S interval derived from Eq. (20) depends on the nucleon form factor g_S (as do all the constraints arising from neutron and nuclear beta decays). For a given experimental accuracy, the constraint on the short-distance couplings $\epsilon_{S,T}$ becomes stronger as $\delta g_{S,T}/g_{S,T} \rightarrow 0$. In this section, we will first explore the maximal constraining power of nuclear and neutron measurements in the ideal scenario of *no uncertainty* on $g_{S,T}$, and for illustrative purposes we assume the central values $g_S = g_T = 1$. We will quantify the implications of finite uncertainties on $g_{S,T}$ on the $\epsilon_{S,T}$ constraints in Section 6.

With the above assumptions on $g_{S,T}$, the currently allowed region (at 90% C.L.) on the ϵ_S - ϵ_T plane is given by the green horizontal band in Figs. 2 and 3. The vertical (ϵ_S) boundaries of this region are determined by the constraint from b_{0+} , while essentially the entire horizontal (ϵ_T) range on the scale of these plots is allowed by the $\pi \rightarrow e\nu\gamma$ limit (see Eq. (22)).

In this ideal scenario of no uncertainty on $g_{S,T}$, we can quantify the impact of future neutron measurements by plotting the 90% C.L. allowed region in the ϵ_S - ϵ_T plane implied by projected limits on b , $b_\nu - b$, and b_ν . The neutron constraints are derived using Eqs. (11) and in generating the plots we use the central value $\lambda = 1.269$. In Fig. 2 we focus on the case in which the experimental sensitivity on b , $b_\nu - b$, and b_ν is at the 10^{-3} level. In the left panel we show the constraints from the existing b_{0+} limit (green horizontal band) and 10^{-3} -level limits on b and $b_\nu - b$, (red and blue bands, respectively).

In the right panel we replace the 10^{-3} -level limit on $b_\nu - b$ with the 10^{-3} limit on b_ν , which in principle can be isolated experimentally [41]. In Fig. 3 we plot the constraints resulting from projected limits on b , $b_\nu - b$, and b_ν at the 10^{-4} level. The intersection of the various bands in Figs. 2 and 3 denotes the combined allowed region in the ϵ_S - ϵ_T plane that would result after future neutron measurements. Two important remarks are in order here:

- For a given experimental sensitivity, the combination $b_\nu - b$ gives weaker constraints on $\epsilon_{S,T}$ than b or b_ν . This is easily understood: by taking the difference of Eqs. (11) one sees that $b_\nu - b \propto \lambda - 1$, which for $\lambda \approx 1.27$ provides a suppression factor.
- There is an almost exact “degeneracy” in the constraints from b and b_ν , again controlled by the form of Eqs. (11) and the numerical value of λ . For the purposes of constraining $\epsilon_{S,T}$, an upper limit on b is essentially equivalent to an upper limit on b_ν . This provides strong motivation to pursue experimental determinations of both $b_\nu - b$ and b_ν via neutrino asymmetry (B) measurements. From the theoretical point of view, we can use either b or b_ν , and in subsequent sections we will use b for illustrative purposes.

Fig. 2 clearly illustrates that with experimental sensitivity in neutron decay at the 10^{-3} level, the most stringent constraint arises from a combination of b_{0+} and b or b_{0+} and b_ν . The complementarity of these measurements would lead to a significant (four-fold) improvement in the bound on ϵ_T , compared to Eq. (22). The impact of 10^{-4} measurements of b , b_ν , and $b_\nu - b$ in neutron decay is even more dramatic (Fig. 3), as in that case the constraint from b_{0+} would become irrelevant and the combination of b and $b_\nu - b$ or b and b_ν would imply an improvement of one order of magnitude in the bound on ϵ_T and a factor of two in ϵ_S .

In Section 6 we will revisit the impact of proposed neutron measurements on $\epsilon_{S,T}$ in light of nonzero uncertainties in the hadronic matrix elements $g_{S,T}$.

5 Lattice calculation of matrix elements

To connect the measurements of b and b_ν in neutron decays to new physics at the TeV scale requires precision measurements of the matrix elements of isovector bilinear quark operators between an initial neutron and final proton state, in particular of the scalar and tensor operators. Lattice QCD is a path-integral formulation of QCD on a discrete, four-dimensional Euclidean spacetime, and numerical simulations of it provide the best nonperturbative method for evaluating these matrix elements. It has been successfully employed to calculate hadron masses and their decay properties, such as matrix elements, with control over statistical and all systematic errors, in many cases at higher precision than can be measured experimentally [66, 67].

To obtain continuum results, estimates from LQCD obtained at a number of values of lattice spacing a and spacetime volume $L^3 \times T$ are extrapolated to $a \rightarrow 0$ and $L \rightarrow \infty$ to eliminate the artifacts introduced by formulating QCD in a finite discretized box. Another source of systematic uncertainty is introduced when estimates obtained at multiple values of u and d quark masses heavier than in nature are extrapolated to the physical

point. One typically uses chiral perturbation theory to carry out this extrapolation, with low-energy constants determined by over-constraining the fits using experimental and lattice data [68]. Current state-of-the-art simulations are beginning to provide results at physical light-quark masses obviating the need for a chiral extrapolation. Recent calculations by the BMW collaboration [69, 70] at multiple lattice spacings, volumes and pion masses as light as 120 MeV provide an excellent demonstration of how hadronic properties can be extracted with fully understood and controlled systematics.

In this section we review current LQCD calculations of the nucleon isovector matrix elements in order to highlight what needs to be done to obtain the precision required to probe new physics at the TeV scale in neutron-decay experiments. We also present our current best estimates of g_S and g_T , which are used in the phenomenological analysis presented in Sec. 6.

5.1 Lattice methodology

A lattice calculation proceeds in two steps: First, a Monte-Carlo sampling of the QCD vacuum, called an “ensemble of gauge-field configurations”, is generated using an appropriate discretization of the gauge and fermion actions. The particular choices of the actions have important implications for the computational cost of the calculation, for the size of the discretization errors and for which symmetries are violated at finite lattice spacing. We will review the existing calculations, summarized in Table 1, with two light flavors (2-flavor) and two light and one strange flavor (2+1-flavor) as these are close approximations to the real world.

The second step is to calculate expectation values on these ensembles of gauge configurations and from these extract estimates of the desired observables. For hadronic observables, the fermion action used at this stage may differ from the one used in producing the gauge configurations, in which case it is called a “mixed-action” calculation. Further details on the domain-wall fermion (DWF) formulation are given in Refs. [71, 72, 73, 74, 75]; clover fermions in Ref. [76]; twisted-mass fermions in Ref. [77]; and improved staggered fermions in Refs. [78, 79, 80].

Calculation of the isovector nuclear matrix elements requires two separate optimizations in addition to the choice of the actions. The first is to tune the size of smearing applied to the local interpolating operator with the correct quantum numbers of the nucleon

$$\chi^N(x) = \epsilon_{abc}[\psi_1^{a\text{T}}(x)C\gamma_5\psi_2^b(x)]\psi_1^c(x), \quad (31)$$

where a, b, c are color indices, C is the charge-conjugation matrix, and ψ_1 and ψ_2 are u or d quarks; for example, to create a proton, we want $\psi_1 = u$ and $\psi_2 = d$. This local operator, unfortunately, couples to the nucleon and all its excited states with the same quantum numbers. To improve the overlap with the desired ground state, the quark fields in this operator may be “smeared” around the point x . The goal of this smearing is to approximate the ground-state nucleon wavefunction. We adopt the commonly used application of the three-dimensional gauge-invariant Laplacian to smear around the source point x and tune the smearing size to improve the overlap with the ground-state nucleon in the two- and three-point correlation functions. The two-point

function, projected to a definite momentum at either the source or sink time by making a three-dimensional Fourier transformation, is given by

$$\begin{aligned}\Gamma_{AB}^{(2)}(t; \mathbf{p}) &= \langle \chi_A^N(t, \mathbf{p}) (\chi_B^N)^\dagger(\mathbf{p}) \rangle \\ &= \sum_n \langle 0 | \chi_A^N(t, \mathbf{p}) | n \rangle \langle n | (\chi_B^N)^\dagger(0) | 0 \rangle \frac{1}{2E_n(\mathbf{p})} e^{-E_n(\mathbf{p})t},\end{aligned}\quad (32)$$

where the indices A and B indicate the choice of operator smearing. The nucleon states are normalized as $\langle 0 | (\chi_A^N)^\dagger | p, s \rangle = X_A u_s(\mathbf{p})$ where X_A is the overlap of the operator with the state, and the spinors satisfy $\sum_s u_s(\mathbf{p}) \bar{u}_s(\mathbf{p}) = E(\mathbf{p}) \gamma^t - i \boldsymbol{\gamma} \cdot \mathbf{p} + m$. In the limit of large time separation t , the correlator is dominated by the ground-state nucleon, and the above form simplifies to

$$\Gamma_{AB}^{(2)}(t; \mathbf{p}) = \frac{E(\mathbf{p}) + M_n}{2E(\mathbf{p})} X_A(\mathbf{p}) X_B(\mathbf{p}) e^{-E(\mathbf{p})t}. \quad (33)$$

To calculate the nucleon matrix elements, we also need to construct nucleon three-point functions with insertion operators $O_\Gamma(x) \equiv Z_\Gamma O_\Gamma^b = Z_\Gamma \bar{u}(x) \Gamma d(x)$, where O^b is the bare operator, Γ represents one of the sixteen Dirac matrices and Z_Γ is the associated renormalization constant of the operator. The three-point functions take the form

$$\Gamma_{AB}^{(3)}(t_i, t, t_f; \mathbf{p}_i, \mathbf{p}_f) = Z_\Gamma \left\langle \chi_B^N(t_f, \mathbf{p}_f) O_\Gamma^b(t) \overline{\chi_A^N}(t_i, \mathbf{p}_i) \right\rangle. \quad (34)$$

By inserting a complete set of states $\{n, n'\}$ between the operators, this three-point function can be written as

$$\begin{aligned}\Gamma_{AB}^{(3),T}(t_i, t, t_f, \mathbf{p}_i, \mathbf{p}_f) &= a^3 Z_\Gamma \sum_n \sum_{n'} \frac{X_{n',B}(p_f) X_{n,A}(p_i)}{4E'_n(\mathbf{p}_f) E'_n(\mathbf{p}_i)} e^{-(t_f-t)E'_n(\mathbf{p}_f)} e^{-(t-t_i)E_n(\mathbf{p}_i)} \\ &\times \sum_{s,s'} T_{\alpha\beta} u_{n'}(\mathbf{p}_f, s')_\beta \langle N_{n'}(\mathbf{p}_f, s') | O_\Gamma^b | N_n(\mathbf{p}_i, s) \rangle \bar{u}_n(\mathbf{p}_i, s)_\alpha,\end{aligned}\quad (35)$$

where T is an appropriate projection on the baryon spinors. At sufficiently large source-sink separation ($t_{\text{sep}} = t_f - t_i$), the signal due to excited states dies out exponentially, and the sum over states reduces to just the ground states $n = n' = 0$. The operator overlap factors $X_{A,B}$ and the exponential time dependence can be canceled out by constructing a ratio of three- and two-point functions, which for the simple case of $\mathbf{p}_i = \mathbf{p}_f = 0$ is

$$R_O = \frac{\Gamma_{AB}^{(3),T}(t_i, t, t_f; \mathbf{p}_i = 0, \mathbf{p}_f = 0)}{\Gamma_{AB}^{(2),T}(t_i, t_f; \mathbf{p} = 0)}. \quad (36)$$

In practice, choosing a sufficiently large source-sink separation t_{sep} to make the excited-state contamination negligible is challenging because the statistical signal in both the two- and three-point functions involving nucleons degrades exponentially with t_{sep} . Thus, the second optimization required is over t_{sep} . In ongoing LQCD calculations we are exploring multiple values of t_{sep} and will explicitly include excited states in our analysis to understand and reduce this systematic error.

Collaboration	Action	N_f	M_π (MeV)	L (fm)	$(M_\pi L)_{\min}$	a (fm)	g_Γ	Calculated
QCDSF[81]	clover	2	595–1000	1.0–2.0	4.6	0.07–0.116	g_A	
QCDSF[82]	clover	2	170–270	2.1–3.0	2.6	0.08–0.116	g_A, g_T	
CLS[83]	clover	2	290–575	1.7–3.4	4.2	{0.05, 0.07, 0.08}	g_A	
ETMC[84]	twisted Wilson	2	260–470	{2.1, 2.8}	3.3	{0.056, 0.070, 0.089}	g_A	
RBC[85]	DWF	2	490–695	1.9	4.75	0.117	g_A, g_P^*, g_T, g_V	
RBC/UKQCD[86, 87]	DWF	2+1	330–670	{1.8, 2.7}	3.8	0.114	g_A, g_T	
LHPC[88, 89, 90]	DWF on staggered	2+1	290–870	{2.5, 2.7}	3.68	0.1224	g_A, g_P^*, g_T	
QCDSF[91]	clover	2+1	350–480	1.87	3.37	0.078	g_A	
HSC[92]	anisotropic clover	2+1	450–840	2.0	4.57	0.125 ($a_t = 0.036$)	g_A	

Table 1: A summary of recent LQCD calculations of g_A , g_P^* and g_T by different collaborations using two and three flavors of dynamical quarks and $O(a)$ -improved actions. For brevity, we use g_P^* for the induced-pseudoscalar charge discussed in Sec. 5.4 and $(M_\pi L)_{\min}$ for the minimum value of $M_\pi L$ used in that set of calculations.

5.2 Issues in extracting the matrix elements

The matrix elements of most interest to us are those of the scalar and tensor bilinear operators, $\bar{u}d$ and $\bar{u}\sigma_{\mu\nu}d$; however, we are calculating all five Lorentz structures as the additional cost is negligible. There is independent interest in high-precision measurements of g_A , and it provides a cross-check of the lattice systematics. The three-point correlation functions of the vector operator will be used to construct ratios of matrix elements and renormalization constants to reduce systematic errors. In this section we summarize issues relevant to the LQCD calculations of these matrix elements.

The desired matrix elements of isovector bilinear operators $O_\Gamma(x) = Z_\Gamma \bar{u}(x)\Gamma d(x)$ have a number of simplifying features and allow us to make certain approximations:

- There are no disconnected Feynman diagrams contributing to the three-point functions. These typically arise when quark fields in composite operators can be contracted between themselves.
- There are no lower-dimensional operators with which isovector bilinear operators mix, so there are no power-law divergences. Only multiplicative renormalization factors Z_Γ need to be calculated.
- Current lattice simulations are done with degenerate u , d quarks, at zero momentum transfer, and do not include electromagnetic effects. The momentum transfer in neutron decay, $q^2 = 1.7$ MeV 2 is sufficiently small that the matrix elements can be calculated at $q_\mu = 0$. Also, the isospin-breaking and electromagnetic contributions are expected to be smaller than the statistical errors.
- Protons and neutrons are both stable asymptotic states of strong interactions, so there are no other hadronic final states that complicate the calculations.

The issues that need to be addressed to obtain precision results are the following:

- The signal-to-noise ratio in both two- and three-point correlators decreases rapidly with the time separation t_{sep} between the source and the sink in Eq. 36. It is, therefore, necessary to improve the signal by increasing the overlap of the operators

used as sources/sinks with the nucleon ground state. As discussed in Sec. 5.1, our current approach is to (i) smear the quark fields in the interpolating operator given in Eq. 31 and tune the smearing size, and (ii) explicitly include excited states in the analysis.

- A careful optimization of the Euclidian time interval t_{sep} between the source and sink in the three-point functions has to be carried out for each lattice spacing a and light-quark mass. On the one hand, this interval should be as large as possible to isolate the nucleon ground state on either side of the operator insertion, and on the other hand the statistical noise limits the time separation. While there is no *a priori* minimum value of t_{sep} as it depends on how well the source and sink operators are tuned, in Sec. 5.3 we show that current data suggest that asymptotic estimates are obtained with $t_{\text{sep}} \geq 1.2$ fm for the operators used. Our focus will be on improving the operators and investigating 2–3 values of t_{sep} to reduce and quantify this systematic error.
- One needs to demonstrate that the lattices are large enough that finite-size effects are under control, especially for proposed calculations with pions masses below 350 MeV. When the spatial volume used is too small, finite-volume effects arise due to the coarseness of the available lattice momenta, squeezing of the wavefunction due to the interaction of a spatially extended particle with itself and contamination from partons wrapping around the lattice. Previous studies have shown, as a rule of thumb, that finite-size effects are smaller than statistical errors for $M_\pi L \gtrsim 4$. The detailed form of the finite-volume corrections is quantity-dependent.
- Very high-statistics measurements, typically on a few thousand gauge configurations, will be needed to improve the signal in the two- and three-point correlation functions to overcome the rapid growth in noise with t_{sep} . Our ongoing calculations show that the statistics needed will be determined by g_S as it has the smallest signal-to-noise ratio.
- The calculations need to be performed at a sufficient number of values of the light-quark mass to extrapolate results to the physical value $m_l = 0.037m_s$, and at sufficient number of values of the lattice spacing a to extrapolate to the continuum limit.
- The renormalization constants Z_Γ depend on the choice of both the gauge and fermion actions and have to be calculated for each ensemble of gauge configurations. In past calculations, Z_A typically varied between 0.75–0.9 for the lattice spacings that have been simulated. The scale-dependent Z_S , Z_P , and Z_T (given in the $\overline{\text{MS}}$ scheme at 2 GeV) show larger variations and dependence on the lattice action. One-loop tadpole improved perturbation theory can underestimate corrections to $|1 - Z_\Gamma|$ by 50%. Nonperturbative methods, such as calculating Z_Γ in the RI-MOM scheme [93, 94, 95], are preferred as they reduce this uncertainty to a few percent, and we will use them in our calculations.

In the next four sub-sections we summarize the extent to which these issues are under control in current calculations of each of the matrix elements in order to highlight what

needs to be done to achieve the desired precision of 10–20%. The analyses of g_A , g_P and g_T are reviews of existing calculations, and the new estimate of g_S we present is preliminary.

5.3 Nucleon axial charge g_A

The axial charge of the nucleon $g_A \equiv g_A(q^2 = 0)$, defined in Eq. 5, is a fundamental hadronic observable, well measured in neutron beta-decay experiments: $g_A = 1.2695(29) \times g_V$ [96], where the vector charge $g_V = 1$ since V_{ud} has been factored out in the Lagrangian given in Eq. (3). Since the axial charge is experimentally well known, it has long served as a benchmark quantity for LQCD calculations, particularly for estimating systematic errors in other nucleon matrix elements that are either poorly measured in experiments or completely unknown.

Many groups worldwide have calculated g_A using various gauge ensembles and fermion actions as summarized in Table 1 and shown in the first two panels of Fig. 4 for two- and three-flavor simulations, respectively. The results from each study, after a chiral extrapolation to the physical pion mass, are shown in the third panel of Fig. 4.

The overall observations are: (i) The central values vary between $1.12 < g_A < 1.26$, and the errors are much larger than the experimental uncertainty. The deviations from the experimental value are large, considering that corrections due to strong interactions determine $g_A - 1$. (ii) There is no significant difference between 2- and 2+1-flavor estimates or dependence on the light-quark mass at these unphysically large $M_\pi^2 \propto m_q$. More high-precision calculations are needed to determine whether the chiral behavior changes at smaller quark masses and to gain control over the extrapolation to the physical M_π . (iii) Within errors, the lattice data are consistent between the different groups (with different lattice actions), different lattice spacings and between 2- and 2 + 1-flavor theories. Our understanding of systematic errors, discussed in Sec. 5.2, are summarized next.

Investigations of finite-volume effects have been carried out by the RBC/UKQCD collaboration [86]. They used domain-wall fermions at a fixed lattice spacing of $1/a = 1.73(3)$ GeV (equivalently, $a = 0.114(2)$ fm) on two lattice sizes $L = 1.8$ and 2.7 fm. They found that at fixed $M_\pi^2 \sim 0.1$ GeV 2 there are significant finite-volume effects for $L < 2.5$ fm, and these lower the value of g_A . They also analyzed g_A as a function of $M_\pi L$ and found that the data scale in this variable; *i.e.* data from a given action and for a given number of flavors collapse onto a single curve. For small $M_\pi L$, the value of g_A is underestimated and to get within 1% of the infinite-volume result requires $M_\pi L \gtrsim 6$.

The QCDSF collaboration [81] analyzed g_A at four lattice spacings ranging from 0.07 to 0.116 fm, and found no significant dependence on the lattice spacing. They, and the ETMC collaboration [84], have also analyzed their data using finite-volume corrections suggested by heavy-baryon chiral perturbation theory (HB χ PT) with small-scale expansion. They find that correcting their data for finite-volume effects at each lattice spacing improves their extrapolation to the physical pion mass. On the other hand, the RBC collaboration [85] finds that such corrections do not account for their data either qualitatively or quantitatively. An understanding of finite-volume effects, therefore, needs more work.

A source of potentially large systematic error is excited-state contamination when the source-sink separation ($t_{\text{sep}} = t_f - t_i$) is insufficient. The 2008 RBC 2-flavor study [85] used $t \approx 1.0$ and 1.2 fm to check whether there is any significant dependence of g_A on t_{sep} . In this case, the values of g_A were consistent within statistical error, and the central values increase by less than 5% between $t_{\text{sep}} = 1.0$ and 1.2 fm. Similarly, LHPC [90] observe a tiny shift of the central value when changing t_{sep} from 1.1 to 1.2 fm. The recent work by the CLS collaboration [83] investigated smaller source-sink separations, $t_{\text{sep}} \approx 0.56, 0.70$ and 1.05 fm, on their $a \approx 0.07$ fm lattices. They find that the value of g_A increases by about 10% with t_{sep} , and at the same time the statistical error increases by a factor of 5. They use a linear extrapolation in t_{sep} to reduce the effect of excited-state contamination and conclude that for the interpolating operators used $t_{\text{sep}} > 1.1$ fm is needed to approximate the asymptotic value. In any case, one should include the excited states explicitly in the analysis of the matrix elements as demonstrated in Refs. [92, 83].

The uncertainty in the lattice determinations of g_A , which still do not fully include all systematic errors discussed in Sec. 5.2, is much larger than the experimental one, limiting its utility as a probe for physics beyond the Standard Model. Our conclusion is that a combination of high statistics, use of multiple t_{sep} and investigation of correlators with different overlap of source with ground versus excited states will be needed to extract the matrix elements with high precision. A promising direction for reducing the statistical error in g_A is to use a simultaneous chiral extrapolation of the octet baryons since the axial charges of the Σ and Ξ baryons are calculated with significantly smaller errors [97]. A major limitation to testing whether excited-state contamination is a significant factor in the underestimate of g_A is the computational resources needed to simulate close to (and eventually at) the physical light-quark masses, high statistics and extrapolations to the continuum limit. The U.S. national report on the future of extreme-scale computing [98] has made the high-precision calculation of g_A a milestone to achieve, so we anticipate steady improvement in lattice estimates of all such matrix elements with increasing computational power.

5.4 Nucleon induced-pseudoscalar charge g_P^*

There has been renewed interest in the induced-pseudoscalar form factor $\tilde{g}_P(q^2)$, defined in Eq. 5b, due to the recent MuCap Collaboration [99] high-precision experiment studying ordinary muon capture (OMC) by protons, $\mu^- p \rightarrow \nu_\mu n$. We define the induced-pseudoscalar coupling as

$$g_P^* = \frac{m_\mu}{2M_N} \tilde{g}_P(q^2 = 0.88m_\mu^2), \quad (37)$$

where m_μ is the muon mass. Improved calculations of electroweak radiative corrections [100] allow precise extraction of the form factor from these experiments. The new MuCap experiment yields $g_P^* = 7.3 \pm 1.1$ [99, 100], which is consistent with the value predicted by heavy-baryon chiral perturbation theory $g_P^{*\chi\text{PT}} = 8.26 \pm 0.16$ [101]. However, it is much smaller than the earlier world average for OMC, $[g_P^{*\text{OMC}}]_{\text{ave}} = 10.5 \pm 1.8$ given in Ref. [102], and the value obtained from a TRIUMF experiment with radiative muon capture (RMC), $\mu^- p \rightarrow \nu_\mu n \gamma$, which gave $g_P^{*\text{RMC}} = 12.4 \pm 1.0$ [103]. After reanalyzing the TRIUMF data, Clark et al. [104] found $g_P^* = 10.6 \pm 1.1$. When combined with the

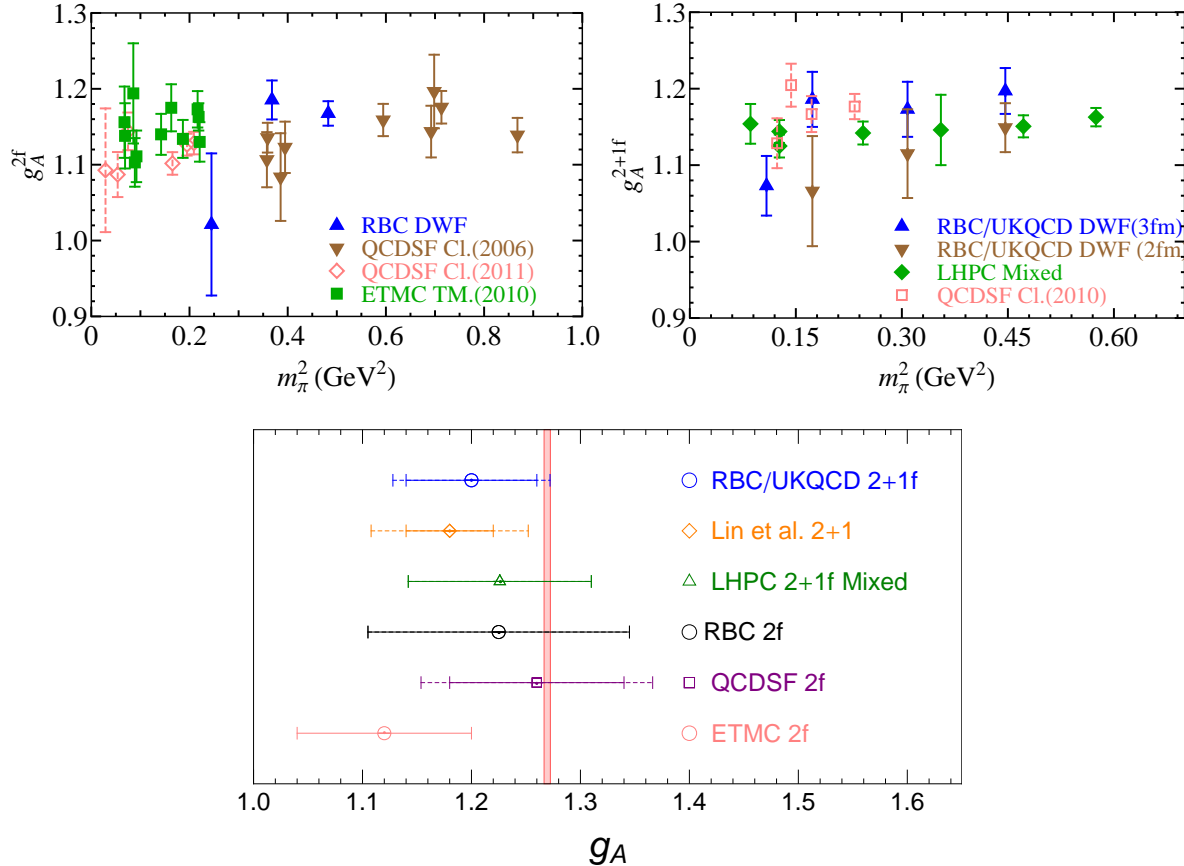


Figure 4: (Upper row) The axial charge versus M_π^2 from $N_f = 2$ [81, 82, 83, 84, 85] (left) and $N_f = 2 + 1$ [86, 90, 88, 91, 92] (right) calculations with different types of $O(a)$ -improved fermion actions. The filled symbols and solid errorbar (open symbols and dashed errorbar) denote results taken from published papers (the latest lattice proceedings). (Lower panel) Comparison of the published values of g_A after chiral and continuum extrapolations with experimental measurements [96] (vertical band). The solid lines indicate statistical error while the dashed lines include systematic errors. Lin et al. [97] find that an SU(3)-constrained fit to the g_A for octet baryons reduces the statistical error in the chiral extrapolation. This is illustrated by the larger errors in the LHPC result [90] compared to those in Ref. [97], which are obtained using similar lattice parameters.

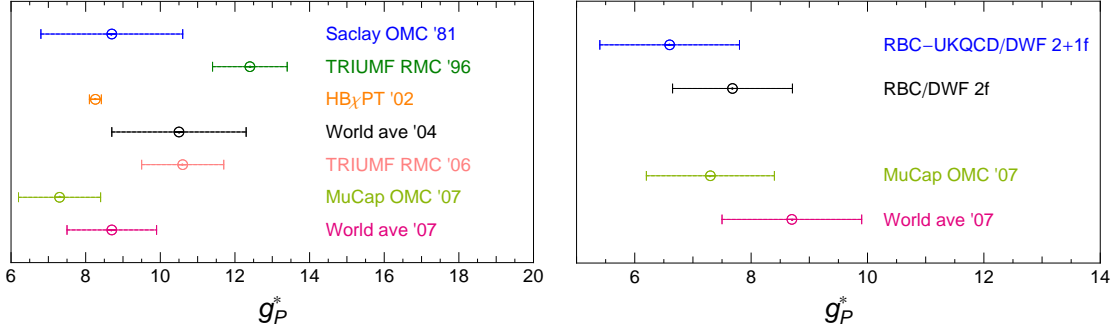


Figure 5: (Left) The induced-pseudoscalar charge of the nucleon g_P^* from experimental measurements [103, 102, 104, 99, 100] and an earlier estimation from $\text{HB}\chi\text{PT}$ [101]. (Right) Comparison of lattice estimates of g_P^* using the DWF fermion action [85, 105, 106] with MuCap data.

new MuCap result, the world average is 8.7 ± 1.0 [100].

There have been few calculations of the induced charge g_P^* in lattice QCD. Unlike g_A , we need to calculate the form-factor at several q^2 to extrapolate $\tilde{g}_P(q^2)$ to the same q^2 as those probed in experiments. The $N_f = 2$ [85] and $2 + 1$ -flavor [106] DWF calculations (Table 1) of g_P^* evaluated at ($q^2 = 0.88m_\mu^2$) by studying the momentum dependence of the axial matrix elements give $7.7(1.0)$ and $6.6(1.2)$, respectively. These central values are about 1σ smaller than the world-averaged MuCap estimate, as shown on the right-hand side of Fig. 5.

Direct calculations of the pseudoscalar charge g_P defined in Eq. 5d have not been done using LQCD due to the lack of experimental motivation. One technical challenge has been removing the contribution of the pion pole to the amputated vertex in the calculation of Z_P in RI-MOM schemes. This has recently been overcome by using non-exceptional momenta in the external quark legs. We, therefore, expect to provide estimates for g_P at the same level of precision as g_T .

5.5 Nucleon tensor charge g_T

The tensor charge g_T is the zeroth moment of transversity, and can be studied through processes such as SIDIS (semi-inclusive deep inelastic scattering). The HERMES and COMPASS experiments [107, 108, 109] presented their first estimates of g_T from data collected at $Q^2 = 2.4 \text{ GeV}^2$. Experimentally, to estimate g_T one first extracts the contribution of individual quarks as a function of the quark momentum fraction x at a particular Q^2 . To obtain the contribution of each quark, the results, estimated from measurements at a finite number of values of x , are integrated over the full range $0 \leq x \leq 1$. The isovector tensor charge is then given by the difference between the up and down quark contributions. Since this analysis requires data over the full range of x , and the low- x and high- x values are not well known, improvements in precision await future experiments. Current extracted numbers are highly model-dependent. Combining SIDIS (HERMES and COMPASS) results with Belle e^+e^- analysis [110, 107] of data collected

at $Q^2 = 110$ GeV 2 , the best experimental estimate of g_T at $Q^2 = 0.8$ GeV 2 (instead of $Q^2 = 0$) is $0.77^{+0.18}_{-0.36}$.

There are also estimates from purely theoretical models. These include the Nambu–Jona-Lasinio model [111] and the chiral-quark soliton model [112]; unfortunately, they are not consistent with each other. Estimates from QCD sum rules [113] have a large uncertainty.

There are several LQCD estimates of g_T , and we review those listed in Table 1. The QCDSF collaboration’s 2-flavor calculations with clover fermions [82, 114], over a large range of pion masses (170–1170 MeV) and 3 lattice spacings [82], show a mild increase in g_T with M_π^2 . RBC’s 2-flavor DWF calculation [85] shows a similar trend and gave $g_T(\overline{\text{MS}}, 2 \text{ GeV}) = 0.93(6)$ after extrapolation to the physical pion mass and using Z_T calculated nonperturbatively in the RI-MOM scheme. These results are summarized on the top of Fig. 6.

The 2+1-flavor results from the LHPC [89, 90] and RBC/UKQCD [87] collaborations are summarized in the second of Fig. 6. RBC/UKQCD used DWF for both dynamical and valence quarks, while LHPC used the mixed-action approach, DWF on a 2+1-flavor staggered (asqtad) gauge ensemble. The lattice spacings in the two calculations are similar, 0.1224 fm and 0.114 fm; thus, we expect similar lattice-discretization errors. The range of pion masses explored is also comparable, 290–760 MeV by LHPC and 330–670 MeV by RBC/UKQCD. Both find the dependence on the pion-mass to be small except at the lightest pion-mass points, 290 and 330 MeV, respectively. At these points, the observed downward dip could be indicative of the onset of chiral logs; however, it is not yet clear whether these points suffer from finite-volume and excited-state effects. Further studies at lighter pion masses are needed to resolve these issues.

To extrapolate the tensor charge to the physical pion mass, we employed the heavy-baryon chiral perturbation theory formulation [115, 116]. The resulting formula for g_T contains one low-energy constant and two scales at lowest order in chiral logs [116]. Analogous formulae for the other twist-two matrix elements, the quark momentum fraction $\langle x \rangle$ and helicity distribution function $\langle \Delta x \rangle$, which can be obtained from x -dependent measurements of polarized and unpolarized form factors, work well in describing the lattice data. We, therefore, analyzed the combined RBC/UKQCD and LHPC g_T data using the HB χ PT ansatz. The fits are highly sensitive to the data points selected, since the chiral log is sensitive to only one point at the lightest M_π . This lack of sensitivity to chiral logs is illustrated by the linear fit to the 2 + 1-flavor data shown in Fig. 6. It fits all points except the one at lowest M_π and gives $g_T = 1.05(2)$. Given this lack of sensitivity to the chiral-log term and the high pion masses used relative to the expected range of validity of this order of HB χ PT, we have little reason to believe that such an extrapolation is well controlled. We include in Fig. 6 a HB χ PT extrapolation consistent with the data in order to illustrate the relative size of the chiral log, which may be quite large and appear at pion masses not much smaller than those currently available. For our best estimate we use $g_T = 1.05(35)$ where the central value is from the linear fit and the uncertainty includes the systematic error associated with the extrapolation in M_π^2 . Clearly data at smaller M_π^2 are needed.

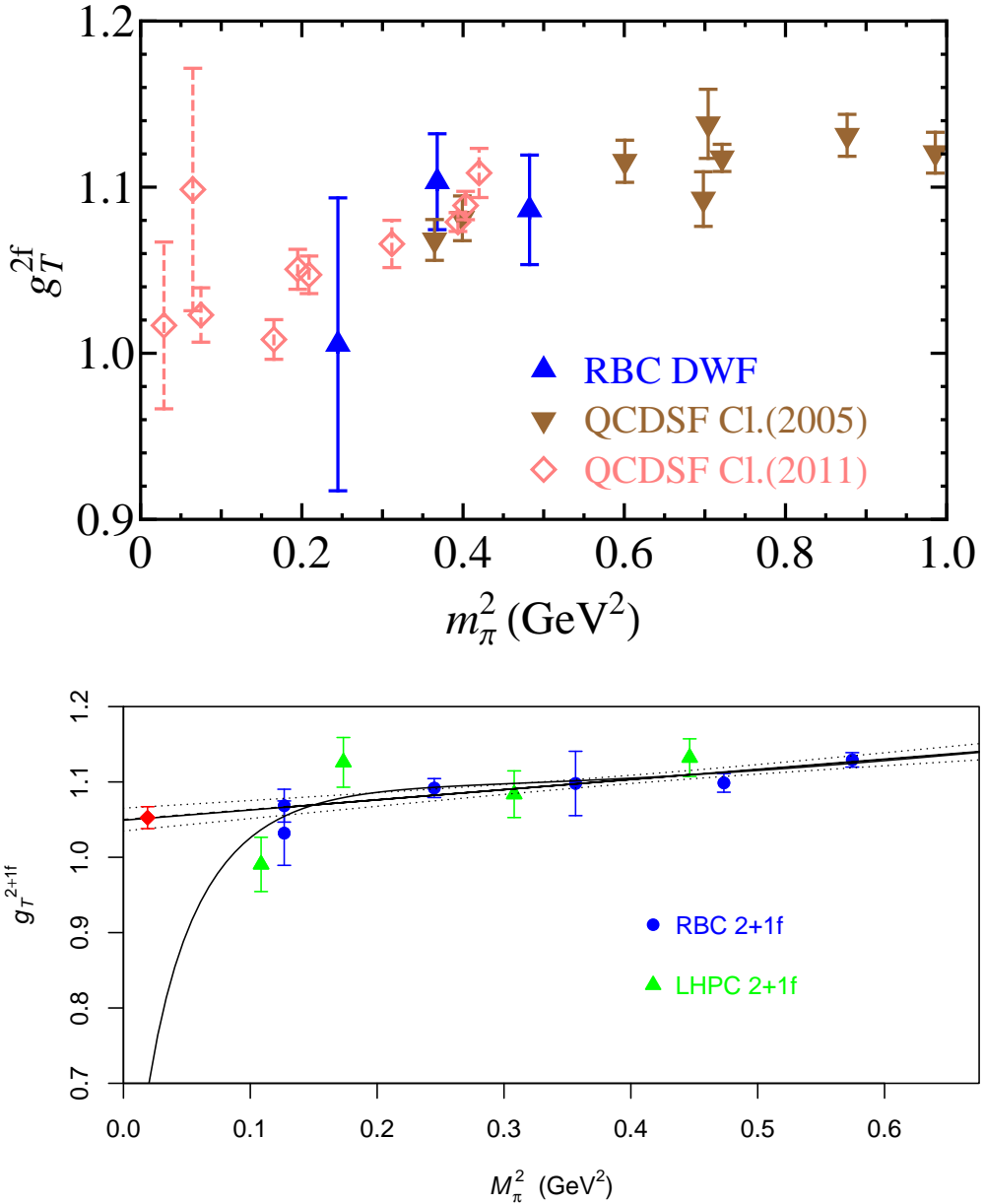


Figure 6: Summary of LQCD estimates of g_T using $N_f = 2$ [114, 82, 85] (top) and $N_f = 2+1$ [87, 90] (bottom) $O(a)$ -improved fermion actions. Two chiral extrapolations of g_T are shown using the combined RBC/UKQCD DWF data on their 2.7-fm ensemble [87] and the LHPC mixed-action data [90]. The value at the physical pion mass from the linear fit is shown by the red diamond. Fits using the HB χ PT ansatz are very sensitive to removing points at large M_π so no error band is shown. For the g_T^{2f} data, the filled symbols and solid error bars (open symbols and dashed error bars) denote results taken from the published papers (the latest lattice proceedings).

5.6 Nucleon scalar charge g_S

The nucleon isovector scalar charge g_S has not been analyzed in lattice calculations, in contrast to its isoscalar partner, the scalar density (or the nucleon- σ term). There are no experimental measurements of this quantity, and theoretical estimates [117] (from different model approximations) give rather loose bounds: $0.25 \leq g_S \leq 1$. Our preliminary lattice calculations show that g_S has the noisiest signal compared to the other matrix elements discussed previously and will, therefore, drive the size of the statistical ensemble required for precision studies of all the matrix elements.

To get a first estimate of g_S , we have performed calculations on two sets of gauge ensembles. The first uses the anisotropic clover lattices generated by the Hadron Spectrum Collaboration (HSC) [118, 119] with pion masses ranging from 390 to 780 MeV. The second uses $N_f = 2 + 1$ asqtad ensembles but calculates matrix elements with domain-wall valence quarks with $M_\pi \in \{350, 700\}$ MeV. The number of configurations analyzed range between 200 and 650. These results are summarized in Fig. 7. The error bars shown are statistical.

There is no clear guidance on how to perform a chiral extrapolation to the physical pion mass since the data show no evidence for chiral logs. We, therefore, made fits assuming a behavior linear or constant in M_π^2 on the full and different subsets of the data. In Fig. 7, we show two fits, a linear one using all the data and a constant fit to the five lightest M_π^2 values. The extrapolated value from such fits to different subsets of data obtained by removing the points corresponding to the heaviest and lightest M_π varies between 0.6–1.0. We take the mean as the central value and 0.2 as an estimate of the error associated with the mass extrapolation.

In addition to the large statistical error, there is significant uncertainty in the estimate of the renormalization constant Z_S . We have used the tadpole-improved tree-level value $Z_S = u_0$, where the tadpole factor u_0 is the fourth root of the expectation value of the 1×1 Wilson loop. For the HSC and DWF ensembles, $u_0 = 0.945$ and 0.938 , respectively. A recent nonperturbative estimate of Z_S for the DWF action on lattices with a similar cutoff a as in our calculations, converted to the $\overline{\text{MS}}$ scheme at 2 GeV, gives 0.65 [120]. We expect a value closer to unity due to the smearing of links in the formulation of the lattice actions we use. Nevertheless, based on current nonperturbative estimates with different actions and link smearings, our estimate is $Z_S = 0.7(2)$ in the $\overline{\text{MS}}$ scheme at 2 GeV. Using this value would lower g_S by about 25%. We take the uncertainty in Z_S into account by doubling the error estimate, and use $g_S = 0.8(4)$.

5.7 Lattice estimates of tensor and scalar charges for $\epsilon_{S,T}$

LQCD calculations of g_S and g_T discussed in the previous sections, while theoretically clean, require reducing a number of systematic errors. Our current understanding is that finite-volume effects are small for $M_\pi L \gtrsim 4$, and there is little evidence for discretization errors at current statistics; contributions due to excited states are smaller than statistical errors once the time separation $t_{\text{sep}} > 1.2$ fm for the current source operators and lattice parameters; and chiral extrapolations gives rise to the biggest uncertainty in the current data as shown in Figs. 6 and 7. Thus, we need high-statistics calculations on large

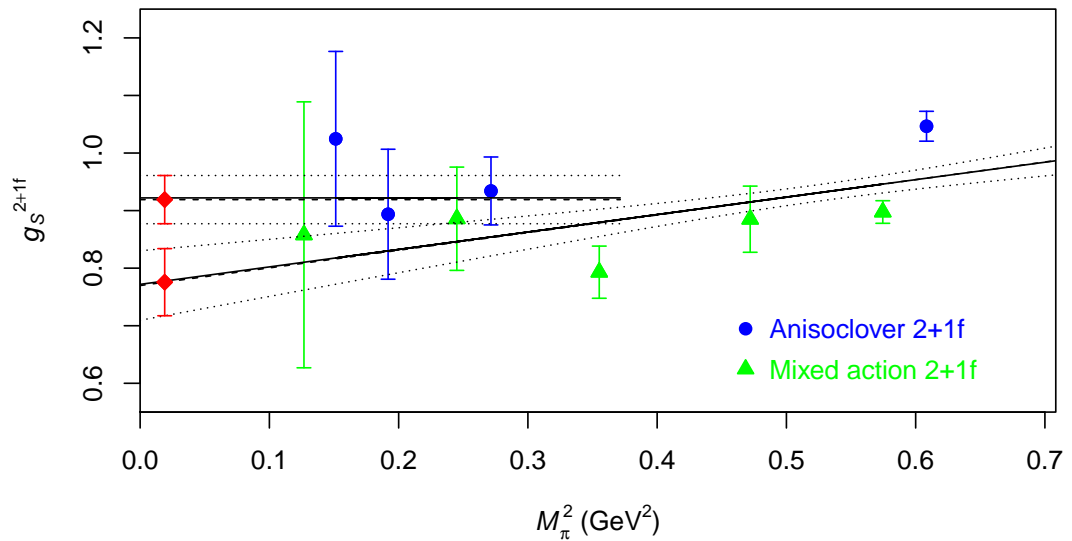


Figure 7: The scalar charge g_S from $N_f = 2 + 1$ anisotropic clover and DWF/asqtad lattices. We also show a linear fit to the full data set and a constant fit to the data at the five smallest values of M_π^2 . The extrapolated values are shown using red diamonds.

lattices with light-quark masses close to the physical values. Lastly, nonperturbative calculations of renormalization constants are essential.

Based on the above analysis, preliminary LQCD estimates are

$$g_T(\overline{\text{MS}}, \mu=2 \text{ GeV}) = 1.05(35), \quad g_S(\overline{\text{MS}}, \mu=2 \text{ GeV}) = 0.8(4). \quad (38)$$

These are used in the next section to explore bounds on new physics at the TeV scale. We emphasize that our focus at this point, given the preliminary nature of the estimates, is on the variation in the bounds under different scenarios of reduction of errors in lattice calculations.

6 Impact of lattice results on phenomenology

In Section 4.2, while studying the low-energy phenomenology of $\epsilon_{S,T}$, we ignored the uncertainty in the charges $g_{S,T}$. Clearly, the impact on $\epsilon_{S,T}$ of future 10^{-3} -level neutron measurements of b , b_ν , and $b_\nu - b$ depends on how well we know the nucleon matrix elements $g_{S,T}$. Since $g_{S,T}$ always multiply factors of the short-distance couplings in physical amplitudes, they determine the slope of the bands on the ϵ_S - ϵ_T plane represented in Figs. 2 and 3. Moreover, if one accounts for the uncertainty in $g_{S,T}$ the bands Figs. 2 and 3 acquire additional theory-induced thickness and their boundaries are mapped into characteristic “bow-tie” shapes. We illustrate this in Fig. 8, assuming experimental sensitivities in b and $b_\nu - b$ at the 10^{-3} level. For the scalar and tensor charges we use in the left panel the ranges quoted in Ref. [20] (based on earlier quark-model estimates): $0.25 < g_S < 1.0$, $0.6 < g_T < 2.3$; while in the right panel we use the lattice estimates $g_S = 0.8(4)$ and $g_T = 1.05(35)$, corresponding to $\delta g_S/g_S \sim 50\%$ and $\delta g_T/g_T \sim 35\%$. Comparing these plots to the ones in Fig. 2 the loss of constraining power is quite evident. Especially in the left panel one sees that the impact of neutron measurements is greatly diluted.

In Fig. 9 we summarize the low-energy constraints on $\epsilon_{S,T}$, taking into account the effects of hadronic uncertainties. We plot the combined 90% C.L. regions in the ϵ_S - ϵ_T plane allowed by the current limit on b_{0+} and future 10^{-3} -level measurements of b and $b_\nu - b$ in neutron decay. The different curves reflect four different scenarios for the hadronic matrix elements: the outer-most curve corresponds the range of Ref. [20], while the three inner curves correspond to lattice results with current central values from Eq. (38) and three different uncertainties: $\delta g_S/g_S \in \{50\%, 20\%, 10\%\}$ with $\delta g_T/g_T = 2/3 \delta g_S/g_S$ (this choice assumes that the ratio of fractional uncertainties in g_S and g_T will remain approximately constant as these uncertainties decrease).

The confidence intervals on $\epsilon_{S,T}$ are obtained using the so-called R-Fit method, as described in Ref. [121]. In this approach the QCD parameters $g_{S,T}$ are bound to remain within allowed ranges determined by the lattice calculations and estimates of systematic uncertainties (in the case at hand the ranges are $0.4 \leq g_S \leq 1.2$ and $0.7 \leq g_T \leq 1.4$). The chi-squared function

$$\chi^2(\epsilon_S, \epsilon_T, g_S, g_T) = \sum_{i=1}^{N_{\text{obs}}} \left(\frac{O_i^{\text{exp}} - O_i^{\text{th}}(\epsilon_S, \epsilon_T, g_S, g_T)}{\sigma_i^{\text{exp}}} \right)^2 \quad (39)$$

is then minimized with respect to $g_{S,T}$ (varying $g_{S,T}$ in their allowed ranges), leading to

$$\bar{\chi}^2(\epsilon_S, \epsilon_T) = \min_{g_{S,T}} \chi^2(\epsilon_S, \epsilon_T, g_S, g_T). \quad (40)$$

Finally, the confidence intervals on $\epsilon_{S,T}$ are deduced applying the standard procedure [96] to $\bar{\chi}^2(\epsilon_S, \epsilon_T)$, with an effective number of degrees of freedom given by $\min(N_{\text{obs}} - N_g, N_\epsilon)$, where N_{obs} is the number of experimental constraints, $N_g = 2$ is the number of QCD parameters ($g_{S,T}$), and $N_\epsilon = 2$ is the number of parameters we wish to constrain ($\epsilon_{S,T}$).

From Fig. 9 several clear messages emerge:

- Hadronic uncertainties in $g_{S,T}$ strongly dilute the significance of new 10^{-3} -level experiments. Experimental progress without theoretical progress will not lead to competitive constraints on the short-distance scalar and tensor interactions.
- Our preliminary lattice results (curve labeled by $\delta g_S/g_S = 50\%$) already provide a significant improvement over previous knowledge of $g_{S,T}$ summarized in Ref. [20].
- In order to fully exploit the constraining power of planned 10^{-3} measurements of b and b_ν , the uncertainty on g_S should be reduced to 20%. Improvement beyond this level would not significantly increase the constraining power (see difference between the curves labeled as $\delta g_S/g_S = 20\%$ and $\delta g_S/g_S = 10\%$).

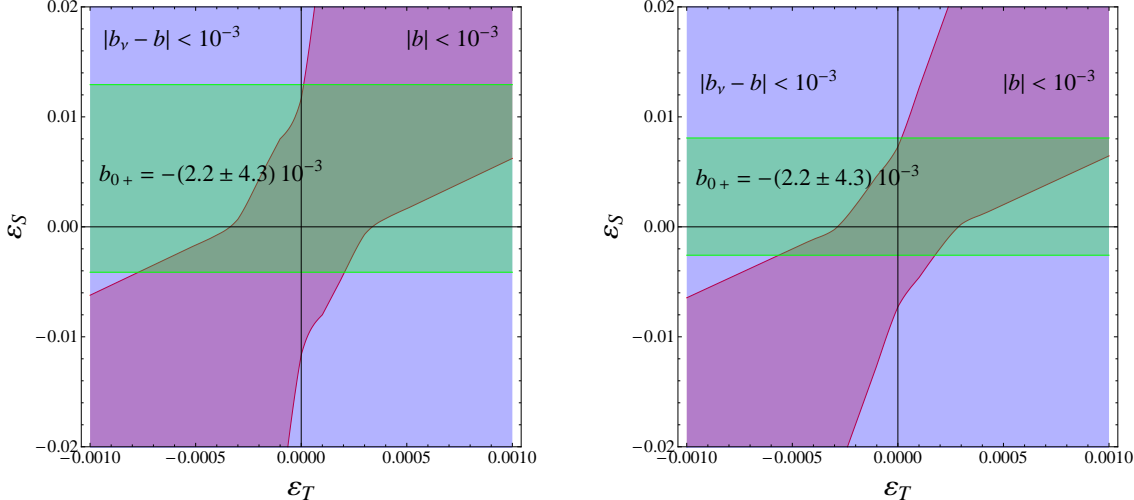


Figure 8: Left panel: 90% C.L. allowed regions in the ϵ_S - ϵ_T plane implied by (i) the existing bound on b_{0+} (green horizontal band); (ii) projected measurements of b and $b_\nu - b$ in neutron decay (red and blue bow-tie shapes) at the 10^{-3} level; (iii) hadronic matrix elements taken in the ranges $0.25 < g_S < 1.0$, $0.6 < g_T < 2.3$ [20]. Right panel: same as left panel but with scalar and tensor charges taken from lattice QCD: $g_S = 0.8(4)$ and $g_T = 1.05(35)$. The effective couplings $\epsilon_{S,T}$ are defined in the $\overline{\text{MS}}$ scheme at 2 GeV.

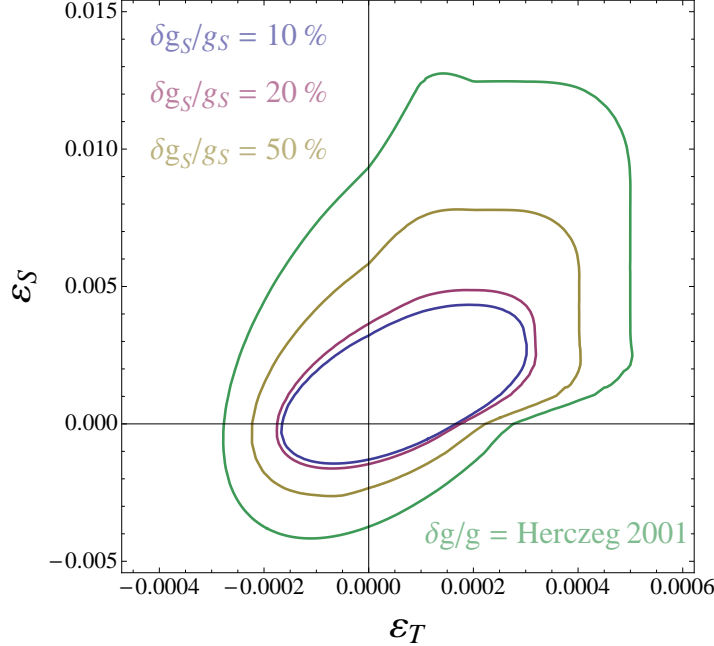


Figure 9: Combined 90% C.L. allowed regions in the ϵ_S - ϵ_T plane based on: (i) existing limit on b_{0^+} from $0^+ \rightarrow 0^+$ nuclear decays; (ii) future neutron decay measurements with projected sensitivity of 10^{-3} in b and $b_\nu - b$. The four curves correspond to four different scenarios for the hadronic matrix elements: $0.25 < g_S < 1.0$, $0.6 < g_T < 2.3$ as quoted in Ref. [20]; lattice results with current central values from Eq. (38) and $\delta g_S/g_S = 50\%, 20\%, 10\%$ with $\delta g_T/g_T = 2/3 \delta g_S/g_S$ (this choice assumes that the ratio of fractional uncertainties in g_S and g_T will remain approximately constant as these uncertainties decrease). The effective couplings $\epsilon_{S,T}$ are defined in the $\overline{\text{MS}}$ scheme at 2 GeV.

7 Collider limits

The contact interactions probed at low energy can also be directly probed at high-energy colliders. The rate, however, depends on whether the particles that generate the 4-fermi interaction are kinematically accessible at the collider energies. We begin in Section 7.1 under the assumption that the scalar and tensor interactions remain point-like at TeV scale energies. Then in Section 7.2 we derive a relation between ϵ_S and the production cross-section, Eq. 54, when the scalar interaction is generated by the exchange of a resonance that is kinematically accessible at the LHC.

7.1 Model-independent limits

Assuming that the scalar and tensor interactions remain point-like at TeV-scale energies, we can employ the operator formalism to put bounds on $\epsilon_{S,T,P}$ from collider physics. $SU(2)$ gauge invariance implies that $\epsilon_{S,T,P}$ control not only charged-current processes but also the corresponding neutral-current versions, as the weak-scale effective Lagrangian includes terms proportional to $(\epsilon_S - \epsilon_P)\bar{e}_R e_L \bar{d}_L d_R$, $(\epsilon_S + \epsilon_P)\bar{e}_R e_L \bar{u}_R u_L$, and

$\epsilon_T \bar{e}_R \sigma^{\mu\nu} e_L \bar{u}_R \sigma_{\mu\nu} u_L$. Exploiting this property, from an early CDF analysis [122] of contact interactions in $p\bar{p} \rightarrow e^+e^- + X$, after matching the different conventions for the effective couplings, we obtain the 90% C.L. limit $|\epsilon_S| < 0.135$. There are a number of LHC searches for contact interactions, specifically in dijet [123, 124, 125] and dimuon [126] final states. All of these studies, however, focus only on specific vector-like interactions and do not consider scalar (i.e. helicity flipping) contact interactions.

Here we focus for definiteness on the charged-current part of the scalar and tensor effective operators. These contact interactions fall into the signature class of collider searches for an exotic W' gauge boson, since they both can contribute to the signature $p\bar{p} \rightarrow e\nu + X$. We will use the analyses and results of searches for this process to obtain bounds on ϵ_S and ϵ_T . In the limit $m_l = 0$ the analysis is simplified, since these operators do not interfere with SM processes. We do include the interference between the scalar and tensor interactions, which does not vanish in the chiral limit. The relevant part of the effective Lagrangian is given by

$$\mathcal{L} = -\frac{\eta_S}{\Lambda_S^2} V_{ud}(\bar{u}d)(\bar{e}P_L\nu_e) - \frac{\eta_T}{\Lambda_T^2} V_{ud}(\bar{u}\sigma^{\mu\nu}P_Ld)(\bar{e}\sigma_{\mu\nu}P_L\nu_e) \quad (41)$$

where $\sigma^{\mu\nu} = i[\gamma^\mu, \gamma^\nu]/2$, and $\eta_S, \eta_T = \pm$ denotes the sign of the coefficients of the scalar and tensor operators. The relations between $\Lambda_{S,T}$ and the effective couplings $\epsilon_{S,T}$ at $\mu = 1$ TeV are given by $\epsilon_S \equiv 2\eta_S v^2/\Lambda_S^2$ and $\epsilon_T \equiv \eta_T v^2/\Lambda_T^2$. Note that since collider searches set limits on the effective couplings $\epsilon_{S,T}$ at the high renormalization scale $\mu = 1$ TeV, a direct comparison with the low-energy constraints requires an appropriate rescaling down to the hadronic scale. Using the one-loop anomalous dimensions for scalar and tensor operators (see [127] and references therein), the one-loop beta function for the strong coupling constant, and including the appropriate heavy quark thresholds, we find in the $\overline{\text{MS}}$ scheme $\epsilon_S(1 \text{ TeV})/\epsilon_S(2 \text{ GeV}) = 0.56$ and $\epsilon_T(1 \text{ TeV})/\epsilon_T(2 \text{ GeV}) = 1.21$. We will use these factors to rescale the collider limits and compare them to low-energy limits in Figs. 10 and 11.

To determine the transverse mass distribution of the electron–neutrino pair we start with [128]

$$\frac{d^3\sigma}{dy dy' dm_T^2} = \frac{1}{64\pi s^2} \sum_{ij} \frac{f_i(x_1)}{x_1} \frac{f_j(x_2)}{x_2} \langle |\mathcal{M}|^2 \rangle \quad (42)$$

where i and j are summed over the initial partons (with parton distribution functions (PDF) $f_{i,j}$ and momentum fractions $x_{1,2}$), and y, y' are the rapidities of the electron and neutrino. One finds $x_1 = m_T(e^y + e^{y'})/2\sqrt{s}$, $x_2 = m_T(e^{-y} + e^{-y'})/2\sqrt{s}$. We also used the observation that the transverse mass of the electron and neutrino, $m_T \equiv \sqrt{2E_T^e E_T^\nu (1 - \cos \Delta\phi_{e\nu})}$ (where $E_T^{e,\nu}$ is the transverse energy of the electron or neutrino, and $\Delta\phi_{e\nu}$ is the azimuthal angle between the two leptons), is simply $m_T = 2p_T$ at leading order, where p_T is the transverse momentum of the electron.

To leading order (LO), the contributions of the color- and spin-averaged scalar and

tensor matrix elements to $pp \rightarrow e\nu + X$, including the interference term, is

$$\begin{aligned} \frac{\langle |\mathcal{M}|^2 \rangle}{|V_{ud}|^2} &= \frac{2}{3} \frac{1}{\Lambda_S^4} (p \cdot p')(k \cdot k') - \frac{8}{3} \frac{\eta_S \eta_T}{\Lambda_S^2 \Lambda_T^2} [(p \cdot k)(p' \cdot k') - (p \cdot k')(p' \cdot k)] \\ &\quad + \frac{16}{3} \frac{1}{\Lambda_T^4} [2(p \cdot k)(p' \cdot k') + 2(p \cdot k')(p' \cdot k) - (p \cdot p')(k \cdot k')] \end{aligned} \quad (43)$$

where p, p' are the momenta of the incoming partons, and k, k' are the momenta of the electron and neutrino. The interference term is antisymmetric under $k \longleftrightarrow k'$, so it does not contribute to the transverse mass distribution obtained by integrating over y and y' . After some substitutions this expression becomes

$$\frac{\langle |\mathcal{M}|^2 \rangle}{|V_{ud}|^2} = \frac{1}{6} \frac{\hat{s}^2}{\Lambda_S^4} - \frac{\eta_S \eta_T}{3} \frac{m_T^2 \hat{s}}{\Lambda_S^2 \Lambda_T^2} \sinh(y - y') + \frac{4}{3} \frac{\hat{s}^2}{\Lambda_T^4} \left(1 - \frac{m_T^2}{\hat{s}}\right) \quad (44)$$

with $\hat{s} = x_1 x_2 s$ and m_T is the transverse mass of the lepton-neutrino pair.

Next we need the cross-section with m_T greater than a threshold $m_{T,\text{cut}}$. Using (42) and (44), one finds

$$\begin{aligned} \sigma(m_T > m_{T,\text{cut}}) &= \frac{s}{48\pi} \int_{m_{T,\text{cut}}^2/s}^1 d\tau \sqrt{\tau} \left[\frac{|V_{ud}|^2}{\Lambda_S^4} \sqrt{\tau - m_{T,\text{cut}}^2/s} + \frac{8}{3} \frac{|V_{ud}|^2}{\tau \Lambda_T^4} \left(\tau - \frac{m_{T,\text{cut}}^2}{s}\right)^{3/2} \right] \\ &\times \int_{\frac{1}{2} \ln \tau}^{-\frac{1}{2} \ln \tau} dy_P [f_{\bar{u}}(\sqrt{\tau} e^{y_P}) f_d(\sqrt{\tau} e^{-y_P}) + (\bar{u}, d) \rightarrow (u, \bar{d})] , \end{aligned} \quad (45)$$

where the sum over $i, j = \bar{u}, d$ and $i, j = u, \bar{d}$ has been done, $\tau = x_1 x_2$, and $y_P = 0.5 \ln(x_1/x_2)$.

The ATLAS and CMS experiments have searched for new physics in $pp \rightarrow e\nu + X$ by looking for an excess of events at large transverse mass [129, 130]. The CMS study analyzes 1.03 fb^{-1} of data for the electron final state, and we begin by following their analysis in setting limits on the scalar and tensor interactions. The CMS search window is defined by specifying a cut on m_T and counting the number of events detected with transverse mass larger than the cut. Specifically, they looked for the production of a heavy W' with decay $W' \rightarrow e\nu$ by searching for events having transverse mass above a variable threshold $m_{T,\text{cut}}$, finding 1 event for $m_{T,\text{cut}} = 1 \text{ TeV}$ and 1 event for $m_{T,\text{cut}} = 1.1 \text{ TeV}$. In general the limit on the number of expected signal events depends on the expected background, n_b , which for this search is quoted to be $n_b = 2.2 \pm 1.1$ events for $m_{T,\text{cut}} = 1 \text{ TeV}$ and $n_b = 1.4 \pm 0.80$ events for $m_{T,\text{cut}} = 1.1 \text{ TeV}$ ¹².

To set a limit we follow Ref. [130] and use Bayesian statistics with a flat prior in the signal n_s . The likelihood function $L(n|n_s)$ is given by the Poisson distribution for n detected events with n_s signal and n_b background events expected. The expected number of signal events is given by $n_s = \epsilon \sigma \mathcal{L}$, where σ is given by (45), \mathcal{L} is the integrated luminosity, and ϵ is the detection efficiency times the geometric acceptance. Ref. [130]

¹² These n_b values are taken from Table 1 of Ref. [130]. Different central values for n_b appear in Figure 2 of Ref. [130]: for example $n_b = 1.15$ for $m_{T,\text{cut}} = 1 \text{ TeV}$. The two sets of n_b are consistent within the quoted error bars and lead to minor (5%) differences in the bounds on $\epsilon_{S,T}$.

quotes the signal efficiency for a W' to be 80%. Their earlier analysis (Ref. [131]), based on 36 pb^{-1} of data, quotes the product of the geometric acceptance and detection efficiency as being greater than 64% in the W' mass range of interest. In the absence of a detector simulation for our signal, in what follows we will assume our signal has a 80% detection times geometric acceptance efficiency.

The credibility level $1 - \alpha$ for a flat prior in the signal is then derived from [96]

$$1 - \alpha = \frac{\int_0^{s_{\text{up}}} dn_s L(n|n_s)}{\int_0^{\infty} dn_s L(n|n_s)} \quad (46)$$

which is equivalent to [96]

$$\alpha = e^{-s_{\text{up}}} \frac{\sum_{m=0}^n \frac{1}{m!} (s_{\text{up}} + n_b)^m}{\sum_{m=0}^n \frac{1}{m!} n_b^m} \quad (47)$$

To set a limit on s_{up} , we choose the lower value of $m_{T,\text{cut}} = 1 \text{ TeV}$ in order to maximize the signal rate. Then for $n_b = 2.2$ expected background events and $n = 1$ event detected, one finds that $s_{\text{up}} = 3.0$ at the 90% credibility level. Dividing by ϵ , we obtain a 90% upper credibility limit of 3.7 produced signal events.

In Fig. 10 we show the corresponding limits on ϵ_S and ϵ_T (red, solid curve), using Eq. (45) with 1.03 fb^{-1} of integrated luminosity at $\sqrt{s} = 7 \text{ TeV}$. LO MSTW 2008 [132] PDFs are used and evaluated at $Q^2 = 1 \text{ TeV}^2$. We also checked that limits obtained using the CTEQ6 PDF set [133] are quantitatively in good agreement. When only one of these operators is present, the bounds on $\epsilon_{S,T}$ correspond to $\Lambda_S > 2.5 \text{ TeV}$ and $\Lambda_T > 2.7 \text{ TeV}$. As illustrated by Fig. 10, our LHC bound on ϵ_S is a factor of 7 stronger than the old CDF limit, but about 4 times weaker than the bound from nuclear beta decay. Similarly, our new collider bound on ϵ_T is a factor of 3 weaker than the bound from radiative pion decay.

We have performed a parallel analysis using the ATLAS results [129] on W' search. Use of the ATLAS results requires an extra step, since their quoted efficiency for a given $m_{T,\text{cut}}$ includes the fraction of total $W' \rightarrow e\nu$ events with $m_T > m_{T,\text{cut}}$. After determining this fraction with a leading-order calculation, we infer the ATLAS detection times geometric acceptance efficiency for $m_{T,\text{cut}} = 1 \text{ TeV}$ to be 80%, the same as quoted by CMS for their experiment. Using then the fact that for $m_T > 1 \text{ TeV}$ ATLAS observes $n = 1$ event with an expected number of background events $n_b = 0.89(20)$, we find that the ATLAS limits on $\epsilon_{S,T}$ differ from the CMS ones only at the 5% level, well within the uncertainties of our leading order calculation. We also estimate that the bounds on $\epsilon_{S,T}$ can be reduced by at least a factor of 2 once the full data set collected at $\sqrt{s} = 7 \text{ TeV}$ is analyzed (see dotted, gold line in Fig. 10). We expect that stronger limits can be obtained by a combined analysis of the ATLAS and CMS data, which goes beyond the scope of this work.

To obtain projected limits at higher luminosities and $\sqrt{s} = 7 \text{ TeV}$ or $\sqrt{s} = 14 \text{ TeV}$, we repeat the same LO analysis, assuming the same 80% detection times acceptance efficiency for the signal as before. We choose an aggressive cut to make the expected background small. The location of the cut on the transverse mass $m_{T,\text{cut}} \sim \text{TeV}$ is estimated by computing at tree-level the transverse mass distribution of the dominant

SM physics background, due to the production of a high- p_T lepton from an off-shell W , and finding the value above which the expected background is less than 1 event. At $\sqrt{s} = 7$ TeV and with an integrated luminosity of 10 fb^{-1} , we find that the number of background events drops below one for $m_{T,\text{cut}} = 1.5 \text{ TeV}$. At $\sqrt{s} = 14 \text{ TeV}$, with $m_{T,\text{cut}} = 2.5 \text{ TeV}$ and an integrated luminosity of 10 fb^{-1} we find 0.5 background events expected above the cut. We also consider an ultimate luminosity of 300 fb^{-1} , finding that for $m_T > 4 \text{ TeV}$ there are 0.3 expected background events. We therefore impose $m_{T,\text{cut}} = 2.5 \text{ TeV}$ (4 TeV), and assume an integrated luminosity of 10 fb^{-1} (300 fb^{-1}). To set a limit we will assume that no events are found, which is consistent with less than 1 background event expected. From Eqs. (46) and (47) we then obtain a 90% Credibility Limit of 3 produced events. The anticipated joint 90% credibility level limits on ϵ_S and ϵ_T from LHC at $\sqrt{s} = 14 \text{ TeV}$ are shown in Fig. 11.

From an inspection of Fig. 11 we find that at high luminosity and center-of-mass energy the expected improvement in the limits are nearly an order of magnitude compared to the existing collider limits. Even with only 10 fb^{-1} taken at 14 TeV we expect the limits to improve substantially from the current collider limit. At these energies and luminosities the bound on ϵ_S from the LHC will become stronger than anticipated future bounds from low-energy experiments. This conclusion is illustrated in Fig. 11, where we also overlay the projected low-energy bounds presented in Fig. 9.

We expect these projected limits can be tightened, since we have chosen hard cuts to reduce the expected leading background to below one event, at the cost of significantly cutting into the signal. Optimizing the choice of the cut to maximize the sensitivity to the contact interactions will require including additional backgrounds, such as QCD and top quarks, and more generally, a better understanding of the systematic errors involved.

Our analyses can certainly be improved. Our estimate of the detection times acceptance efficiency was borrowed from the estimate for a W' signal from [130]. Obviously a detector simulation of the signal will provide a better estimate of this factor. The theoretical error on the signal rate will be further reduced once the next-leading-order QCD contributions are known.

Finally, the interaction Lagrangian (41) can be generalized to include interactions of the electron with neutrinos of all flavors, with a corresponding generalization of $\epsilon_{S,T} \rightarrow \epsilon_{S,T}^\alpha$ where $\alpha \in \{e, \mu, \tau\}$. Because the final states with different neutrino flavors do not interfere and neither do the scalar and tensor interactions after integrating over the rapidity distributions, the derived and projected bounds shown in Figs. 10 and 11 now apply to the quantities $\sqrt{\sum_\alpha (\epsilon_{S,T}^\alpha)^2}$.

7.2 Scalar resonance

A larger signal rate is obtained if the particle that generates the scalar interaction is kinematically accessible at the LHC. In this case there can be a direct relationship between ϵ_S and the production cross-section and mass of the resonance, as we now demonstrate.

We assume that after electroweak symmetry breaking there is a charged scalar ϕ^+ of

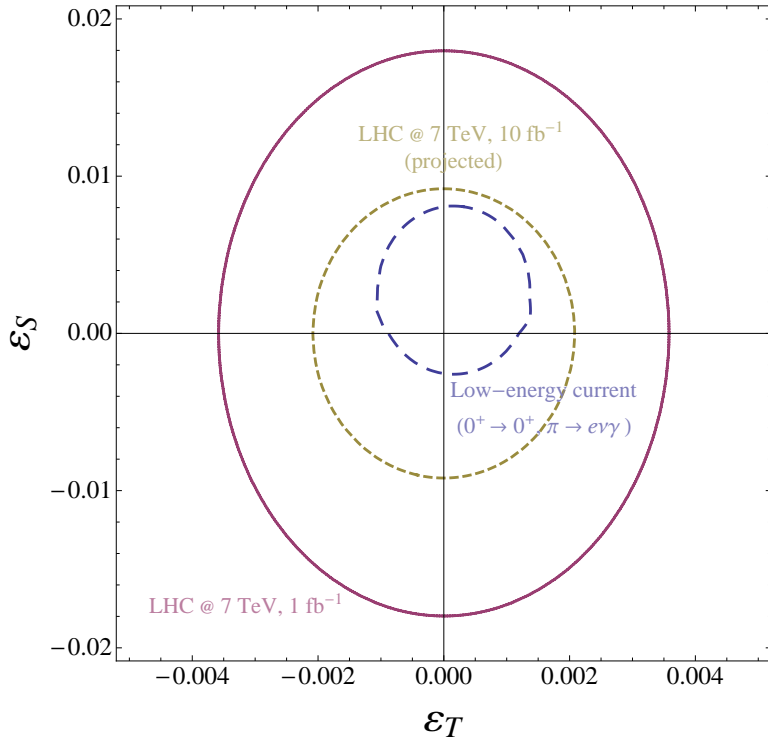


Figure 10: Joint 90% CL limit on ϵ_S and ϵ_T implied by: (i) current bounds from nuclear β decay $0^+ \rightarrow 0^+$ and radiative pion decay (blue, dashed); (ii) CMS search [130] in the channel $pp \rightarrow e\nu + X$ at $\sqrt{s} = 7$ TeV with 1.03 fb^{-1} of data. The limit is obtained by requiring less than 3.7 $e\nu$ -produced events having $m_T > 1$ TeV (red, solid). LO MSTW 2008 [132] parton distribution functions are used; (iii) projected LHC searches in the channel $pp \rightarrow e\nu + X$ at $\sqrt{s} = 7$ TeV with 10 fb^{-1} of data (gold, dotted). The limit is obtained by requiring less than 3 $e\nu$ -produced signal events with $m_T > 1.5$ TeV and assuming that no events are observed. The cut is chosen to reduce the expected leading background to be below 1 event. The effective couplings $\epsilon_{S,T}$ are defined in the $\overline{\text{MS}}$ scheme at 2 GeV.

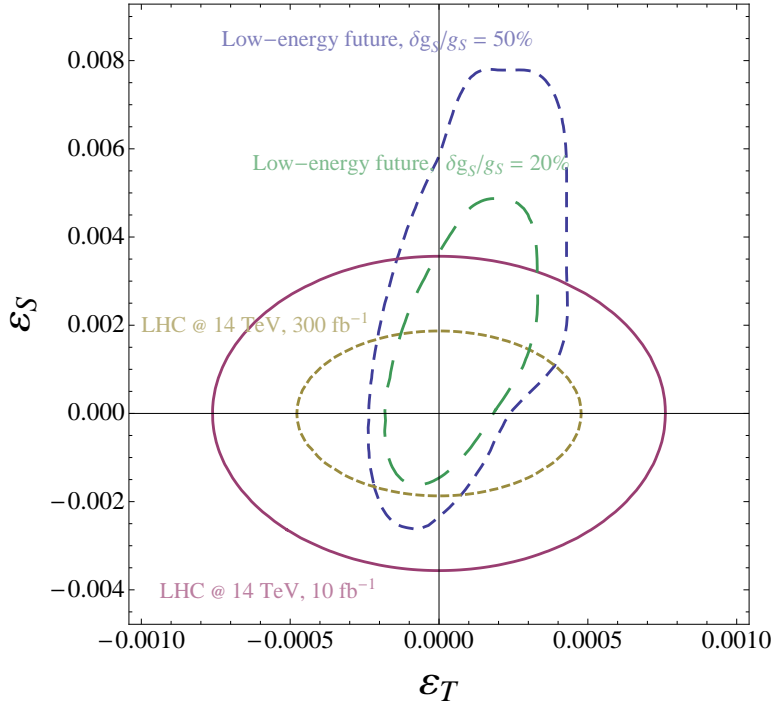


Figure 11: Projected joint 90% credibility level limit on ϵ_S and ϵ_T from the LHC at $\sqrt{s} = 14$ TeV, obtained from requiring less than 3 $e\nu$ -produced signal events with: (i) $m_T > 2.5$ TeV and 10 fb^{-1} of integrated luminosity (solid, red ellipse); and (ii) $m_T > 4$ TeV and 300 fb^{-1} (dashed, yellow ellipse). Cuts are chosen to reduce the expected leading background to be below 1 event. To obtain the projection it is assumed no events are found. Same PDFs are used as in Fig. 10. Note the change in scale between these two figures. Anticipated bounds from low-energy experiments and reduced LQCD uncertainties, redrawn from Fig. 9, are shown for comparison. The effective couplings $\epsilon_{S,T}$ are defined in the $\overline{\text{MS}}$ scheme at 2 GeV.

mass m , with the following couplings to first-generation quarks and leptons:

$$\mathcal{L} = \lambda_S V_{ud} \phi^+ \bar{u}d + \lambda_P V_{ud} \phi^+ \bar{u} \gamma_5 d + \lambda_l \phi^- \bar{e} P_L \nu_e + \text{h.c.} , \quad (48)$$

where $\phi^- \equiv (\phi^+)^*$. At low energies the exchange of ϕ^+ generates a scalar operator with

$$\epsilon_S = 2\lambda_S \lambda_l \frac{v^2}{m^2} \quad (49)$$

and a pseudoscalar operator with

$$\epsilon_P = 2\lambda_P \lambda_l \frac{v^2}{m^2} . \quad (50)$$

To proceed, at leading order the cross-section for the on-shell production of ϕ , which then decays to $l\nu$ (of a given sign), is given in the narrow-width approximation by

$$\sigma \cdot \text{BR} = \lambda_l^2 (\lambda_S^2 + \lambda_P^2) |V_{ud}|^2 \frac{m}{48s\Gamma_\phi} L(\tau) \quad (51)$$

with $\tau = m^2/s$, $L(\tau) = \int_\tau^1 dx f_q(x) f'_q(\tau/x)/x$, and where Γ_ϕ is the total decay width of ϕ . Next, note that since ϕ may decay to other particles (not just to $l\nu$ and ud) ,

$$\Gamma_\phi \geq \Gamma_l + \Gamma_q = (\lambda_l^2 + 2N_c(\lambda_S^2 + \lambda_P^2)|V_{ud}|^2) \frac{m}{16\pi} \quad (52)$$

with $N_c = 3$. Next note that $m/\Gamma_\phi \leq 16\pi/(\lambda_l^2 + 2N_c(\lambda_S^2 + \lambda_P^2)|V_{ud}|^2)$, and then use the arithmetic-geometric inequality $\sqrt{2N_c}\lambda_\phi\lambda_l < \frac{1}{2}(\lambda_l^2 + 2N_c(\lambda_S^2 + \lambda_P^2)|V_{ud}|^2)$, where $\lambda_\phi = \sqrt{\lambda_S^2 + \lambda_P^2}|V_{ud}|$, to finally obtain our main result of this subsection,

$$\sigma \cdot \text{BR} \leq \frac{|V_{ud}|}{12v^2} \frac{\pi}{\sqrt{2N_c}} \left(\sqrt{\epsilon_S^2 + \epsilon_P^2} \right) \tau L(\tau) \quad (53)$$

Because of the severe constraint imposed by $\pi \rightarrow e\nu$, the coupling λ_P of ϕ to the pseudoscalar quark scalar density must be significantly suppressed. In the limit $\epsilon_P \ll \epsilon_S$ one then has

$$\sigma \cdot \text{BR} \leq \frac{|V_{ud}|}{12v^2} \frac{\pi}{\sqrt{2N_c}} |\epsilon_S| \tau L(\tau) \quad (54)$$

This expression can be rearranged to obtain a lower bound on ϵ_S , that is stronger after summing in L over both charged-particle final states. The bound depends only on τ and $\sigma \cdot \text{BR}$. Figure 12 shows the bound as a function of τ for several choices of $\sigma \cdot \text{BR}$ that will be probed by the LHC. Equivalent limits are shown in Figs. 13 and 14, where we show the dependence of the bound on the mass of the resonance, for several values of $\sigma \cdot \text{BR}$ and at $\sqrt{s} = 7$ and 14 TeV. LO CTEQ6 [133] parton distribution functions are used for all these figures.

We have shown that if a signal is observed in $pp \rightarrow e + \text{missing energy (MET)} + X$, then a lower bound on ϵ_S can be obtained, provided the signal is due to the on-shell production of a scalar, which decays to an electron and missing energy provided by an electron

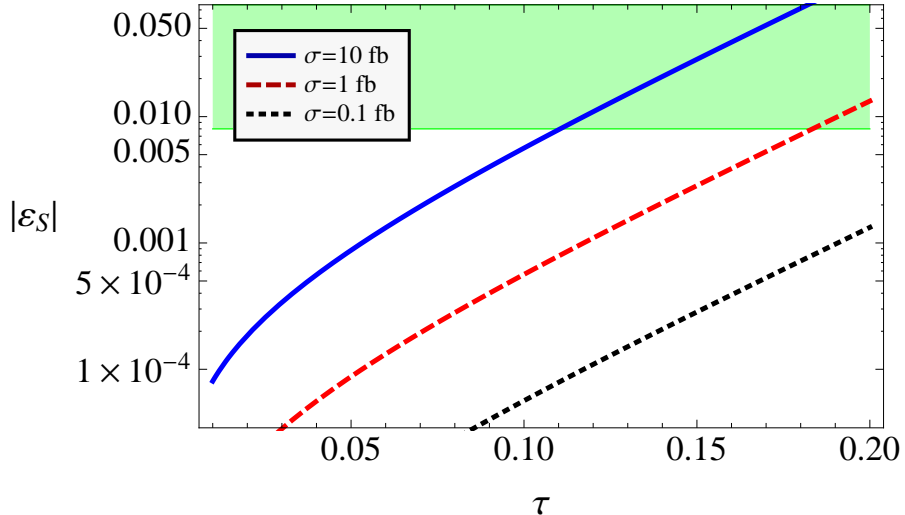


Figure 12: Projected lower bound on $|\epsilon_S|$ (at $\mu = 2$ GeV), for a discovery cross-section of $\sigma(pp \rightarrow e + \text{MET} + X) = 10$ fb (blue, solid), 1 fb (red, dashed) and 0.1 fb (black, dotted), as a function of $\tau = m^2/s$. Shaded region (green) shows the current experimental exclusion on ϵ_S from $0^+ \rightarrow 0^+$ nuclear β decay.

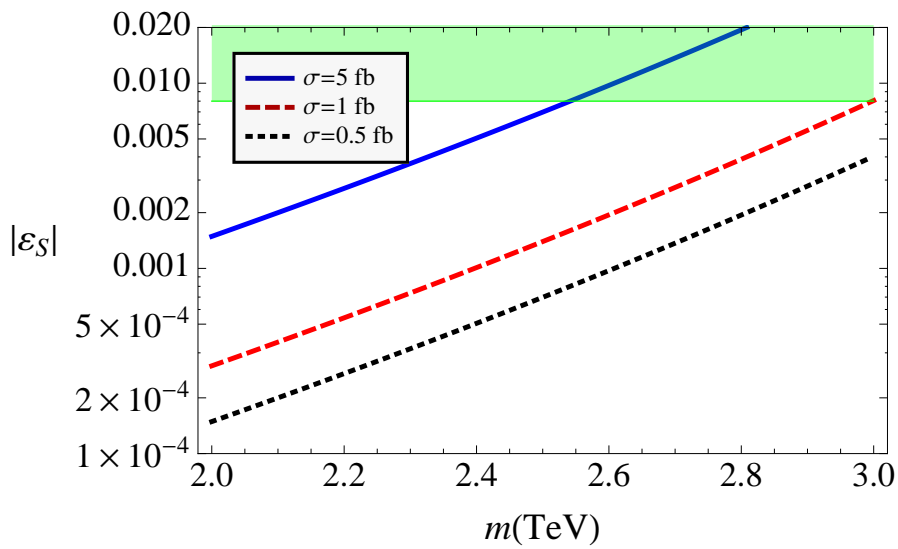


Figure 13: Projected lower bound on $|\epsilon_S|$ (at $\mu = 2$ GeV) for $\sqrt{s} = 7$ TeV and a discovery cross-section of $\sigma(pp \rightarrow e + \text{MET} + X) = 5$ fb (blue, solid), 1 fb (red, dashed) and 0.5 fb (black, dotted). Shaded region (green) shows the current experimental exclusion on ϵ_S from $0^+ \rightarrow 0^+$ nuclear β decay. The bound scales linearly with $\sigma \cdot \text{BR}$.

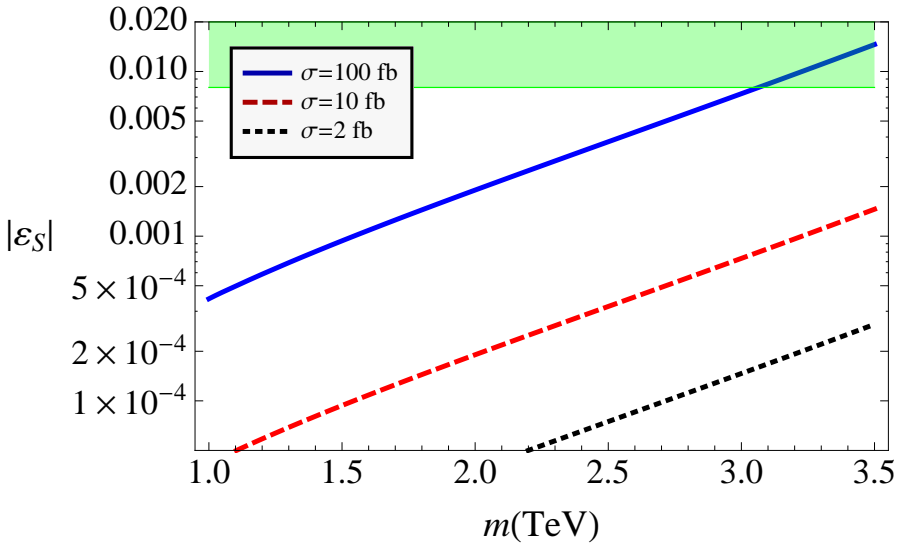


Figure 14: Same as Fig. 13 but for $\sqrt{s} = 14$ TeV and $\sigma \cdot \text{BR} = 100$ fb (blue, solid), 10 fb (red, dashed) and 2 fb (black, dotted).

neutrino, and whose pseudoscalar coupling to quarks is suppressed compared to its scalar coupling. That the resonance couples to an electron neutrino is important in deriving the above relation to ϵ_S , since at linear order in the ϵ 's, neutron-decay experiments do not probe couplings to other neutrino flavors $\epsilon_S^{\alpha \in \{\mu, \tau\}}$.

Further confidence that the signal is due to the production of an on-shell particle can be established by the detection of an edge in the transverse electron-neutrino mass distribution, and through the detection of a resonance in dijets. The only additional theoretical assumption used to obtain the lower limit (54) is that the charged resonance ϕ is interpreted as a scalar and not as a vector or a tensor. Measurements of the rapidity distribution of the electron should determine the spin of ϕ .

If a signal is discovered in $pp \rightarrow e + \text{MET} + X$ then neutron and nuclear β -experiments will be crucial in order to pin down the properties of the resonance and of the MET. As an illustration, suppose the measured cross-section and mass imply an ϵ_S in excess of existing neutron decay bounds, then either: (i) the resonance does not have spin 0; or (ii) as already described above, since the outgoing neutrino flavor is not identified, the relationship between the cross-section and ϵ_S can be undone simply if the scalar ϕ couples preferentially to muon and tau neutrinos rather than to the electron neutrino; or (iii) there are additional scalars at the TeV scale or a scalar contact interaction, such that partial cancellations occur in summing the multiple contributions to ϵ_S .

8 Discussion

It is anticipated that the next generation of neutron β -decay experiments will increase their sensitivity to BSM scalar and tensor interactions by an order of magnitude, through improved measurements of the neutrino asymmetry parameter B and the Fierz inter-

ference term b (see Figs. 2, 3, and 9). In order to assess the impact of these future experiments, we have performed a comprehensive analysis of constraints on scalar and tensor BSM interactions from a broad range of low-energy probes (neutron decay, nuclear decays, pion decays) as well as collider searches.

Extracting bounds on scalar and tensor BSM couplings from neutron and nuclear beta decays requires knowledge of the nucleon scalar and tensor form factors at zero momentum transfer. In this paper we have provided the first lattice-QCD estimate of the scalar form-factor, $g_S = 0.8(4)$, and a new average of existing tensor form-factor results, $g_T = 1.05(35)$. We find that to fully exploit the increased experimental sensitivity will require understanding the lattice-QCD estimates of the proton-to-neutron matrix elements at the level of 10–20% (see Fig. 9). To do that will require analyzing a few thousand samples at each value of the simulation parameters using a combination of decorrelated lattices and multiple source points on each lattice, improvements in source and sink interpolating operators for nucleons, and simulations close to physical light-quark masses. With the anticipated increase in computing power and resources, we estimate calculations will reach this precision in 2–4 years.

In our survey of probes of BSM scalar and tensor interactions, we have found that the currently strongest bounds arise from nuclear β decay (ϵ_S) and radiative pion decay (ϵ_T), probing effective scales $\Lambda_S > 4.7$ TeV and $\Lambda_T > 5$ TeV, respectively. We also find that within a specific model for the lepton flavor structure of the scalar and tensor interactions, significantly stronger bounds arise from $\pi \rightarrow e\nu$ decay, a conclusion in agreement with previous literature.

We have used LHC data to obtain constraints on the scalar and tensor interactions, finding bounds within sight of current limits obtained from low-energy measurements (see Fig. 10). We have also provided a preliminary estimate of expected future bounds from the LHC, finding that an order of magnitude improvement should ultimately be achievable and that the future collider constraints (associated with effective scales $\Lambda_{S,T} \sim 7$ TeV) will compete with improved neutron-decay constraints based on experimental sensitivities $\delta b, \delta b_\nu \sim 10^{-3}$ (see Fig. 11). Finally, if a charged resonance decaying to an electron plus missing energy is discovered at the LHC, we have shown how, with some theoretical assumptions, the production cross-section provides a lower bound on the scalar interaction probed at low energy (see Figs. 12, 13, and 14).

Our analysis shows that in order to compete with upcoming collider bounds on scalar and tensor interactions, future neutron-decay experiments should aim at the very least to sensitivities $\delta b, \delta b_\nu \sim 10^{-3}$ in the Fierz interference term and neutrino asymmetry. Moreover, experiments aiming for $\delta b, \delta b_\nu \sim 10^{-4}$ would provide an unmatched discovery potential for new scalar and tensor interactions, and therefore should be vigorously pursued.

Acknowledgments

The lattice tensor- and scalar-charge calculations were done on Hyak cluster (NSF MRI PHY-0922770) at University of Washington. (We thank MILC and HSC for their dynamical lattices, and LHPC and NPLQCD collaborations for the light DWF propagators).

TB and RG are supported in part by DOE grant No. DE-KA-1401020. HWL and SDC are supported in part by the U.S. Dept. of Energy under grant No. DE-FG02-97ER4014. SDC was also supported by DOE grant No. DE-FG02-91ER40676 and DE-FC02-06ER41440 and NSF grant No. 0749300. TB, VC, MG, and RG are supported by DOE grant No. DE-AC52-06NA25396 and by the LDRD program at LANL. MGA was supported by the U.S. DOE contract DE-FG02-08ER41531 and by the Wisconsin Alumni Research Foundation. The work of AF is supported by an FPU Grant (MICINN, Spain). This work has been supported in part by MEC (Spain) under Grant FPA2007-60323, by the Spanish Consolider Ingenio 2010 Programme CPAN (CSD2007-00042) and by CSIC under grant PII-200750I026. We thank Joe Carlson, Sacha Davidson, Anosh Joseph, Greg Landsberg, and Michael Ramsey-Musolf for discussions and correspondence.

A $SU(2) \times U(1)$ invariant operators contributing to charged-current processes

The building blocks to construct gauge-invariant local operators are the gauge fields G_μ^A , W_μ^a , B_μ , corresponding to $SU(3) \times SU(2)_L \times U(1)_Y$, the five fermionic gauge multiplets,

$$l^i = \begin{pmatrix} \nu_L^i \\ e_L^i \end{pmatrix} \quad e^i = e_R^i \quad q^i = \begin{pmatrix} u_L^i \\ d_L^i \end{pmatrix} \quad u^i = u_R^i \quad d^i = d_R^i , \quad (55)$$

the Higgs doublet φ

$$\varphi = \begin{pmatrix} \varphi^+ \\ \varphi^0 \end{pmatrix} , \quad (56)$$

and the covariant derivative

$$D_\mu = I \partial_\mu - ig_s \frac{\lambda^A}{2} G_\mu^A - ig \frac{\sigma^a}{2} W_\mu^a - ig' Y B_\mu . \quad (57)$$

In the above expression λ^A are the $SU(3)$ Gell-Mann matrices, σ^a are the $SU(2)$ Pauli matrices, g_s, g, g' are the gauge couplings and Y is the hypercharge of a given multiplet.

The minimal set of operators contributing to low-energy charged current processes can be divided into two groups: four-fermion operators

$$O_{lq}^{(3)} = (\bar{l}\gamma^\mu\sigma^a l)(\bar{q}\gamma_\mu\sigma^a q) \quad (58a)$$

$$O_{qde} = (\bar{l}e)(\bar{d}q) + \text{h.c.} \quad (58b)$$

$$O_{lq} = (\bar{l}_a e)\epsilon^{ab}(\bar{q}_b u) + \text{h.c.} \quad (58c)$$

$$O_{lq}^t = (\bar{l}_a \sigma^{\mu\nu} e)\epsilon^{ab}(\bar{q}_b \sigma_{\mu\nu} u) + \text{h.c.} \quad (58d)$$

and vertex corrections

$$O_{\varphi\varphi} = i(\varphi^T \epsilon D_\mu \varphi)(\bar{u}\gamma^\mu d) + \text{h.c.} , \quad (59a)$$

$$O_{\varphi q}^{(3)} = i(\varphi^\dagger D^\mu \sigma^a \varphi)(\bar{q}\gamma_\mu\sigma^a q) + \text{h.c..} \quad (59b)$$

Moreover, the extraction of the Fermi constant from muon decay (needed for weak universality tests) is affected by two more operators (four-lepton and lepton-gauge vertex correction):

$$O_{ll}^{(3)} = \frac{1}{2}(\bar{l}\gamma^\mu\sigma^a l)(\bar{l}\gamma_\mu\sigma^a l) \quad (60a)$$

$$O_{\varphi l}^{(3)} = i(\varphi^\dagger D^\mu\sigma^a \varphi)(\bar{l}\gamma_\mu\sigma^a l) + \text{h.c.} \quad (60b)$$

In terms of the coefficients of the above operators, the low-energy effective couplings appearing in \mathcal{L}_{CC} (see Eq. 2) are given by

$$V_{ij} \cdot [v_L]_{\ell\ell ij} = 2V_{ij} \left[\hat{\alpha}_{\varphi l}^{(3)} \right]_{\ell\ell} + 2V_{im} \left[\hat{\alpha}_{\varphi q}^{(3)} \right]_{jm}^* - 2V_{im} \left[\hat{\alpha}_{lq}^{(3)} \right]_{\ell\ell m j} \quad (61a)$$

$$V_{ij} \cdot [v_R]_{\ell\ell ij} = -[\hat{\alpha}_{\varphi\varphi}]_{ij} \quad (61b)$$

$$V_{ij} \cdot [s_L]_{\ell\ell ij} = -[\hat{\alpha}_{lq}]_{\ell\ell ji}^* \quad (61c)$$

$$V_{ij} \cdot [s_R]_{\ell\ell ij} = -V_{im} [\hat{\alpha}_{qde}]_{\ell\ell jm}^* \quad (61d)$$

$$V_{ij} \cdot [t_L]_{\ell\ell ij} = -[\hat{\alpha}_{lq}^t]_{\ell\ell ji}^* \quad (61e)$$

B Details of neutron decay distribution

The effective Fierz interference term \bar{b} and effective energy-dependent correlation coefficients $\bar{a}(E_e)$, $\bar{A}(E_e)$, $\bar{B}(E_e)$ and $\bar{C}_{(aa,aA,aB)}(E_e)$ introduced in Eq. 9 are [36, 37]:

$$\bar{b} = b^{\text{SM}} + b^{\text{BSM}} \quad (62a)$$

$$\bar{a}(E_e) = \left(a_{\text{LO}}(\tilde{\lambda}) + c_0^{(a)} + c_1^{(a)} \frac{E_e}{M_N} \right) \left(1 + \frac{\alpha}{2\pi} \delta_\alpha^{(2)}(E_e) \right) \quad (62b)$$

$$\bar{A}(E_e) = \left(A_{\text{LO}}(\tilde{\lambda}) + c_0^{(A)} + c_1^{(A)} \frac{E_e}{M_N} \right) \left(1 + \frac{\alpha}{2\pi} \delta_\alpha^{(2)}(E_e) \right) \quad (62c)$$

$$\bar{B}(E_e) = B_{\text{LO}}(\tilde{\lambda}) + c_0^{(B)} + c_1^{(B)} \frac{E_e}{M_N} + \frac{m_e}{E_e} (b_\nu^{\text{SM}} + b_\nu^{\text{BSM}}) \quad (62d)$$

$$\bar{C}_{(aa)}(E_e) = c_1^{(aa)} \frac{E_e}{M_N} \quad (62e)$$

$$\bar{C}_{(aA)}(E_e) = c_1^{(aA)} \frac{E_e}{M_N} \quad (62f)$$

$$\bar{C}_{(aB)}(E_e) = \left(c_0^{(aB)} + c_1^{(aB)} \frac{E_e}{M_N} \right) . \quad (62g)$$

In these expressions the subscript LO indicates the well-known leading-order contributions that survive if we neglect the radiative corrections, recoil effects and new-physics contributions¹³

$$a_{\text{LO}}(\lambda) = \frac{1 - \lambda^2}{1 + 3\lambda^2}, \quad A_{\text{LO}}(\lambda) = \frac{2\lambda(1 - \lambda)}{1 + 3\lambda^2}, \quad B_{\text{LO}}(\lambda) = \frac{2\lambda(1 + \lambda)}{1 + 3\lambda^2}. \quad (63)$$

¹³In that limit, of course $\tilde{\lambda} \rightarrow \lambda$ in a_{LO} , A_{LO} and B_{LO} .

As discussed in the main text, the linear new-physics effect due to the ϵ_R coupling has been included in the replacement $\lambda \rightarrow \tilde{\lambda} = \lambda(1 - 2\epsilon_R)$. The only other linear BSM effects in the differential distribution are b^{BSM} and b_ν^{BSM} , whose expressions are shown in the main text, Eqs. (11).

Radiative corrections are encoded in the function $\delta_\alpha^{(2)}(E_e)$ [36], while recoil corrections are encoded in the coefficients $c_{0,1}^{a,A,B,aa,aA,aB}$, b^{SM} and b_ν^{SM} , whose explicit expressions are [37]

$$c_0 = -\frac{2\lambda(\lambda + \mu_V)}{1 + 3\lambda^2} \frac{E_0}{M_N} \quad (64)$$

$$c_1 = \frac{3 + 4\lambda\mu_V + 9\lambda^2}{1 + 3\lambda^2} \quad (65)$$

$$c_0^{(a)} = \frac{2\lambda(\lambda + \mu_V)}{1 + 3\lambda^2} \frac{E_0}{M_N} \quad (66)$$

$$c_1^{(a)} = -\frac{4\lambda(3\lambda + \mu_V)}{1 + 3\lambda^2} \quad (67)$$

$$c_0^{(A)} = \frac{(\lambda - 1)(\lambda + \mu_V)}{1 + 3\lambda^2} \frac{E_0}{M_N} \quad (68)$$

$$c_1^{(A)} = \frac{\mu_V(1 - 3\lambda) + \lambda(7 - 5\lambda)}{1 + 3\lambda^2} \quad (69)$$

$$c_0^{(B)} = -\frac{2\lambda(\lambda + \mu_V)}{1 + 3\lambda^2} \frac{E_0}{M_N} \quad (70)$$

$$c_1^{(B)} = \frac{\mu_V(1 + 3\lambda) + \lambda(5 + 7\lambda)}{1 + 3\lambda^2} \quad (71)$$

$$c_0^{(aB)} = \frac{(1 + \lambda)(\lambda + \mu_V)}{1 + 3\lambda^2} \frac{E_0}{M_N} \quad (72)$$

$$c_1^{(aB)} = -\frac{(\mu_V + 7\lambda)(1 + \lambda)}{1 + 3\lambda^2} \quad (73)$$

$$c_1^{(aa)} = -\frac{3(1 - \lambda^2)}{1 + 3\lambda^2} \quad (74)$$

$$c_1^{(aA)} = \frac{(\lambda - 1)(\mu_V + 5\lambda)}{1 + 3\lambda^2} \quad (75)$$

$$b^{\text{SM}} = -\frac{m_e}{M_N} \frac{1 + 2\mu_V\lambda + \lambda^2}{1 + 3\lambda^2} \quad (76)$$

$$b_\nu^{\text{SM}} = -\frac{m_e}{M_N} \frac{(1 + \lambda)(\mu_V + \lambda)}{1 + 3\lambda^2} \quad (77)$$

In the above relations μ_V represents the difference between the proton and neutron magnetic moments. Numerically, one has $b^{\text{SM}} = -1.35(1) \times 10^{-3}$ and $b_\nu^{\text{SM}} = -1.27(1) \times 10^{-3}$.

References

- [1] Steven Weinberg. V-A was the key. *J. Phys. Conf. Ser.*, 196:012002, 2009, doi:10.1088/1742-6596/196/1/012002.
- [2] Nathal Severijns, Marcus Beck, and Oscar Naviliat-Cuncic. Tests of the standard electroweak model in beta decay. *Rev. Mod. Phys.*, 78:991–1040, 2006, doi:10.1103/RevModPhys.78.991, [arXiv:nucl-ex/0605029](https://arxiv.org/abs/nucl-ex/0605029).
- [3] Hartmut Abele. The neutron. Its properties and basic interactions. *Prog. Part. Nucl. Phys.*, 60:1–81, 2008, doi:10.1016/j.ppnp.2007.05.002.
- [4] Dirk Dubbers and Michael G. Schmidt. The neutron and its role in cosmology and particle physics. 2011, [arXiv:1105.3694](https://arxiv.org/abs/1105.3694).
- [5] M. Dewey, K. Coakley, D. Gilliam, G. Greene, A. Laptev, J. Nico, W. Snow, F. Wietfeldt, and A. Yue. Prospects for a new cold neutron beam measurement of the neutron lifetime. *Nucl. Instr. Meth.*, A611(2–3):189–192, 2009, doi:10.1016/j.nima.2009.07.069.
- [6] S. Arzumanov, L. Bondarenko, P. Geltenbort, V. Morozov, V.V. Nesvizhevsky, Yu. Panin, and A. Strepetov. A new project to measure the neutron lifetime using storage of ultracold neutrons and detection of inelastically scattered neutrons. *Nucl. Instr. Meth.*, A611(2–3):186–188, 2009, doi:10.1016/j.nima.2009.07.070.
- [7] P.L. Walstrom, J.D. Bowman, S.I. Penttila, C. Morris, and A. Saunders. A magneto-gravitational trap for absolute measurement of the ultra-cold neutron lifetime. *Nucl. Instr. Meth.*, A599(1):82–92, 2009, doi:10.1016/j.nima.2008.11.010.
- [8] S. Materne, R. Picker, I. Altarev, H. Angerer, B. Franke, E. Gutzmiedl, F.J. Hartmann, A.R. Müller, S. Paul, and R. Stoepler. PENeLOPE—on the way towards a new neutron lifetime experiment with magnetic storage of ultra-cold neutrons and proton extraction. *Nucl. Instr. Meth.*, A611(2–3):176–180, 2009, doi:10.1016/j.nima.2009.07.055.
- [9] K.K.H. Leung and O. Zimmer. Proposed neutron lifetime measurement using a hybrid magnetic trap for ultra-cold neutrons. *Nucl. Instr. Meth.*, A611(2–3):181–185, 2009, doi:10.1016/j.nima.2009.07.087.
- [10] B. Markisch et al. The new neutron decay spectrometer PERKEO III. *Nucl. Instrum. Meth.*, A611:216–218, 2009, doi:10.1016/j.nima.2009.07.066.
- [11] B. Plaster, R. Carr, B.W. Filippone, D. Harrison, J. Hsiao, et al. A Solenoidal electron spectrometer for a precision measurement of the neutron β -asymmetry with ultracold neutrons. *Nucl. Instrum. Meth.*, A595:587–598, 2008, doi:10.1016/j.nima.2008.07.143, [arXiv:0806.2097](https://arxiv.org/abs/0806.2097).
- [12] R. Alarcon et al. Precise Measurement of Neutron Decay Parameters, 2007, http://nab.phys.virginia.edu/abba_proposal_2007.pdf.

- [13] D. Dubbers, H. Abele, S. Baessler, B. Maerkisch, M. Schumann, et al. A Clean, bright, and versatile source of neutron decay products. *Nucl. Instrum. Meth.*, A596:238–247, 2008, doi:10.1016/j.nima.2008.07.157, [arXiv:0709.4440](https://arxiv.org/abs/0709.4440).
- [14] W.S. Wilburn et al. Measurement of the neutrino-spin correlation Parameter b in neutron decay using ultracold neutrons. *Rev. Mex. Fis.*, Suppl. 55(2):119, 2009.
- [15] Dinko Pocanic et al., Nab Collaboration. Nab: Measurement Principles, Apparatus and Uncertainties. *Nucl. Instrum. Meth.*, A611:211–215, 2009, doi:10.1016/j.nima.2009.07.065, [arXiv:0810.0251](https://arxiv.org/abs/0810.0251).
- [16] S. S. Baeßler et al. First measurements with the neutron decay spectrometer aSPECT. *Eur. Phys. J.*, A38:17–26, 2008, doi:10.1140/epja/i2008-10660-0.
- [17] F.E. Wietfeldt, B.M. Fisher, C. Trull, G.L. Jones, B. Collet, et al. A method for an improved measurement of the electron–antineutrino correlation in free neutron beta decay. *Nucl. Instrum. Meth.*, A545:181–193, 2005, doi:10.1016/j.nima.2005.01.339.
- [18] K. P. Hickerson. The Fierz Interference Term in Beta-Decay Spectrum of UCN, 2009, http://neutron.physics.ncsu.edu/UCN_Workshop_09/Hickerson_SantaFe_2009.pdf. UCN Workshop, November 6–7 2009, Santa Fe, New Mexico.
- [19] Stefano Profumo, Michael J. Ramsey-Musolf, and Sean Tulin. Supersymmetric contributions to weak decay correlation coefficients. *Phys. Rev.*, D75:075017, 2007, doi:10.1103/PhysRevD.75.075017, [arXiv:hep-ph/0608064](https://arxiv.org/abs/hep-ph/0608064).
- [20] P. Herczeg. Beta decay beyond the standard model. *Prog. Part. Nucl. Phys.*, 46:413–457, 2001, doi:10.1016/S0146-6410(01)00149-1.
- [21] Vincenzo Cirigliano, James Jenkins, and Martin Gonzalez-Alonso. Semileptonic decays of light quarks beyond the Standard Model. *Nucl. Phys.*, B830:95–115, 2010, doi:10.1016/j.nuclphysb.2009.12.020, [arXiv:0908.1754](https://arxiv.org/abs/0908.1754).
- [22] W. Buchmuller and D. Wyler. Effective Lagrangian Analysis of New Interactions and Flavor Conservation. *Nucl. Phys.*, B268:621, 1986, doi:10.1016/0550-3213(86)90262-2.
- [23] Michael Carpentier and Sacha Davidson. Constraints on two-lepton, two quark operators. *Eur. Phys. J.*, C70:1071–1090, 2010, doi:10.1140/epjc/s10052-010-1482-4, [arXiv:1008.0280](https://arxiv.org/abs/1008.0280).
- [24] M.B. Voloshin. Upper bound on tensor interaction in the decay $\pi \rightarrow e\nu\gamma$. *Phys. Lett.*, B283:120–122, 1992, doi:10.1016/0370-2693(92)91439-G.
- [25] P. Herczeg. On the question of a tensor interaction in $\pi \rightarrow e\nu\gamma$ decay. *Phys. Rev.*, D49:247–253, 1994, doi:10.1103/PhysRevD.49.247.
- [26] Bruce A. Campbell and David W. Maybury. Constraints on scalar couplings from $\pi \rightarrow e\nu$. *Nucl. Phys.*, B709:419–439, 2005, doi:10.1016/j.nuclphysb.2004.12.015, [arXiv:hep-ph/0303046](https://arxiv.org/abs/hep-ph/0303046).

- [27] Steven Weinberg. Charge symmetry of weak interactions. *Phys. Rev.*, 112:1375–1379, 1958, doi:10.1103/PhysRev.112.1375.
- [28] Barry R. Holstein. Recoil Effects in Allowed beta Decay: The Elementary Particle Approach. *Rev. Mod. Phys.*, 46:789, 1974, doi:10.1103/RevModPhys.46.789.
- [29] M. Ademollo and Raoul Gatto. Nonrenormalization Theorem for the Strangeness Violating Vector Currents. *Phys. Rev. Lett.*, 13:264–265, 1964, doi:10.1103/PhysRevLett.13.264.
- [30] John F. Donoghue and D. Wyler. Isospin breaking and the precise determination of V_{ud} . *Phys. Lett.*, B241:243, 1990, doi:10.1016/0370-2693(90)91287-L.
- [31] T.D. Lee and Chen-Ning Yang. Question of Parity Conservation in Weak Interactions. *Phys. Rev.*, 104:254–258, 1956, doi:10.1103/PhysRev.104.254.
- [32] J. D. Jackson, S. B. Treiman, and H. W. Wyld. Possible tests of time reversal invariance in Beta decay. *Phys. Rev.*, 106:517–521, 1957, doi:10.1103/PhysRev.106.517.
- [33] Vincenzo Cirigliano, Martin Gonzalez-Alonso, and Michael L. Graesser, 2011. Work in preparation.
- [34] Denys H. Wilkinson. Analysis of neutron beta decay. *Nucl. Phys.*, A377:474–504, 1982, doi:10.1016/0375-9474(82)90051-3.
- [35] F. Gluck, I. Joo, and J. Last. Measurable parameters of neutron decay. *Nucl. Phys.*, A593:125–150, 1995, doi:10.1016/0375-9474(95)00354-4.
- [36] S. Ando et al. Neutron beta decay in effective field theory. *Phys. Lett.*, B595:250–259, 2004, doi:10.1016/j.physletb.2004.06.037, arXiv:nucl-th/0402100.
- [37] Vladimir P. Gudkov, G.L. Greene, and J.R. Calarco. General classification and analysis of neutron β -decay experiments. *Phys. Rev.*, C73:035501, 2006, doi:10.1103/PhysRevC.73.035501, arXiv:nucl-th/0510012.
- [38] Andrzej Czarnecki, William J. Marciano, and Alberto Sirlin. Precision measurements and CKM unitarity. *Phys. Rev.*, D70:093006, 2004, doi:10.1103/PhysRevD.70.093006, arXiv:hep-ph/0406324.
- [39] Susan Gardner and C. Zhang. Sharpening low-energy, standard model tests via correlation coefficients in neutron beta decay. *Phys. Rev. Lett.*, 86:5666–5669, 2001, doi:10.1103/PhysRevLett.86.5666, arXiv:hep-ph/0012098.
- [40] S.K.L. Sjue. Polarized neutron beta-decay: The Proton asymmetry and recoil-order currents. *Phys. Rev.*, C72:045501, 2005, doi:10.1103/PhysRevC.72.045501, 10.1103/PhysRevC.83.019901, arXiv:nucl-th/0507041.
- [41] Albert Young, 2011. Private communication.

- [42] H. Abele, M. Astruc Hoffmann, S. Baessler, D. Dubbers, F. Gluck, et al. Is the unitarity of the quark mixing CKM matrix violated in neutron β -decay? *Phys. Rev. Lett.*, 88:211801, 2002, doi:10.1103/PhysRevLett.88.211801, arXiv:hep-ex/0206058.
- [43] J. Liu et al., UCNA Collaboration. Determination of the Axial-Vector Weak Coupling Constant with Ultracold Neutrons. *Phys. Rev. Lett.*, 105:181803, 2010, doi:10.1103/PhysRevLett.105.181803, arXiv:1007.3790.
- [44] M. Schumann, T. Soldner, M. Deissenroth, F. Gluck, J. Krempel, et al. Measurement of the neutrino asymmetry parameter B in neutron decay. *Phys. Rev. Lett.*, 99:191803, 2007, doi:10.1103/PhysRevLett.99.191803, arXiv:0706.3788.
- [45] J. Byrne, P.G. Dawber, M.G.D. van der Grinten, C.G. Habeck, F. Shaikh, et al. Determination of the electron anti-neutrino angular correlation coefficient a_0 and the parameter $|\lambda| = |G_A/G_V|$ in free neutron β -decay from measurements of the integrated energy spectrum of recoil protons stored in an ion trap. *J. Phys.*, G28:1325–1349, 2002, doi:10.1088/0954-3899/28/6/314.
- [46] G. Konrad, W. Heil, S. Baessler, D. Pocanic, and F. Gluck. Impact of Neutron Decay Experiments on non-Standard Model Physics. 2010, arXiv:1007.3027.
- [47] A. Serebrov, V. Varlamov, A. Kharitonov, A. Fomin, Yu. Pokotilovski, et al. Measurement of the neutron lifetime using a gravitational trap and a low-temperature Fomblin coating. *Phys. Lett.*, B605:72–78, 2005, doi:10.1016/j.physletb.2004.11.013, arXiv:nucl-ex/0408009.
- [48] A. Pichlmaier, V. Varlamov, K. Schreckenbach, and P. Geltenbort. Neutron lifetime measurement with the UCN trap-in-trap MAMBO II. *Phys. Lett.*, B693:221–226, 2010, doi:10.1016/j.physletb.2010.08.032.
- [49] William J. Marciano and Alberto Sirlin. Improved calculation of electroweak radiative corrections and the value of V_{ud} . *Phys. Rev. Lett.*, 96:032002, 2006, doi:10.1103/PhysRevLett.96.032002, arXiv:hep-ph/0510099.
- [50] J.C. Hardy and I.S. Towner. Superallowed $0^+ \rightarrow 0^+$ nuclear β decays: A New survey with precision tests of the conserved vector current hypothesis and the standard model. *Phys. Rev.*, C79:055502, 2009, doi:10.1103/PhysRevC.79.055502, arXiv:0812.1202.
- [51] M. Bychkov, D. Pocanic, B.A. VanDevender, V.A. Baranov, Wilhelm H. Bertl, et al. New Precise Measurement of the Pion Weak Form Factors in $\pi \rightarrow e\nu\gamma$ Decay. *Phys. Rev. Lett.*, 103:051802, 2009, doi:10.1103/PhysRevLett.103.051802, arXiv:0804.1815.
- [52] V. Mateu and J. Portoles. Form-factors in radiative pion decay. *Eur. Phys. J.*, C52:325–338, 2007, doi:10.1140/epjc/s10052-007-0393-5, arXiv:0706.1039.

- [53] F. Wauters, I.S. Kraev, D. Zakoucky, M. Beck, M. Breitenfeldt, et al. Precision measurements of the ^{60}Co β -asymmetry parameter in search for tensor currents in weak interactions. *Phys. Rev.*, C82:055502, 2010, doi:10.1103/PhysRevC.82.055502, arXiv:1005.5034.
- [54] F. Wauters, I. Kraev, M. Tandecki, E. Traykov, S. Van Gorp, et al. β asymmetry parameter in the decay of ^{114}In . *Phys. Rev.*, C80:062501, 2009, doi:10.1103/PhysRevC.80.062501, arXiv:0901.0081.
- [55] A.S. Carnoy, J. Deutsch, T.A. Girard, and R. Prieels. Limits on nonstandard weak currents from the polarization of ^{14}O and ^{10}C decay positrons. *Phys. Rev.*, C43:2825–2834, 1991, doi:10.1103/PhysRevC.43.2825.
- [56] V.A. Wichers, T.R. Hageman, J. Van Klinken, H.W. Wilschut, and D. Atkinson. Bounds on Right-handed Currents from Nuclear Beta Decay. *Phys. Rev. Lett.*, 58:1821–1824, 1987, doi:10.1103/PhysRevLett.58.1821.
- [57] N. Severijns et al. Fundamental Weak Interaction Studies using Polarised Nuclei and Ion Traps. *Hyperfine Interactions*, 129:223–236, 2000, doi:10.1023/A:1012665917625.
- [58] P.A. Vetter, J.R. Abo-Shaeer, S.J. Freedman, and R. Maruyama. Measurement of the β - ν correlation of ^{21}Na using shakeoff electrons. *Phys. Rev.*, C77:035502, 2008, doi:10.1103/PhysRevC.77.035502, arXiv:0805.1212.
- [59] A. Gorelov, D. Melconian, W.P. Alford, D. Ashery, G. Ball, et al. Scalar interaction limits from the β - ν correlation of trapped radioactive atoms. *Phys. Rev. Lett.*, 94:142501, 2005, doi:10.1103/PhysRevLett.94.142501, arXiv:nucl-ex/0412032.
- [60] E.G. Adelberger et al., ISOLDE Collaboration. Positron neutrino correlation in the $0^+ \rightarrow 0^+$ decay of ^{32}Ar . *Phys. Rev. Lett.*, 83:1299–1302, 1999, doi:10.1103/PhysRevLett.83.1299, arXiv:nucl-ex/9903002.
- [61] C.H. Johnson, Frances Pleasonton, and T.A. Carlson. Precision Measurement of the Recoil Energy Spectrum from the Decay of ^6He . *Phys. Rev.*, 132:1149–1165, 1963, doi:10.1103/PhysRev.132.1149.
- [62] D.I. Britton, S. Ahmad, D.A. Bryman, R.A. Burnbam, E.T.H. Clifford, et al. Measurement of the $\pi^+ \rightarrow e^+\nu$ branching ratio. *Phys. Rev. Lett.*, 68:3000–3003, 1992, doi:10.1103/PhysRevLett.68.3000.
- [63] G. Czapek, A. Federspiel, A. Fluckiger, D. Frei, B. Hahn, et al. Branching ratio for the rare pion decay into positron and neutrino. *Phys. Rev. Lett.*, 70:17–20, 1993, doi:10.1103/PhysRevLett.70.17.
- [64] Vincenzo Cirigliano and Ignasi Rosell. $\pi/K \rightarrow e\bar{\nu}_e$ branching ratios to $O(e^2 p^4)$ in Chiral Perturbation Theory. *JHEP*, 0710:005, 2007, doi:10.1088/1126-6708/2007/10/005, arXiv:0707.4464.

- [65] Vincenzo Cirigliano and Ignasi Rosell. Two-loop effective theory analysis of $\pi(K) \rightarrow e\bar{\nu}_e[\gamma]$ branching ratios. *Phys. Rev. Lett.*, 99:231801, 2007, doi:10.1103/PhysRevLett.99.231801, [arXiv:0707.3439](#).
- [66] Jack Laiho, Enrico Lunghi, and Ruth S. Van de Water. Lattice QCD inputs to the CKM unitarity triangle analysis. *Phys. Rev.*, D81:034503, 2010, doi:10.1103/PhysRevD.81.034503, [arXiv:0910.2928](#).
- [67] Christopher Sachrajda. Phenomenology from the Lattice. *PoS*, LATTICE2010:018, 2010, [arXiv:1103.5959](#).
- [68] Gilberto Colangelo, Stephan Durr, Andreas Juttner, Laurent Lellouch, Heinrich Leutwyler, et al. Review of lattice results concerning low energy particle physics. *Eur. Phys. J.*, C71:1695, 2011, doi:10.1140/epjc/s10052-011-1695-1, [arXiv:1011.4408](#).
- [69] S. Durr, Z. Fodor, J. Frison, C. Hoelbling, R. Hoffmann, et al. Ab Initio Determination of Light Hadron Masses. *Science*, 322:1224–1227, 2008, doi:10.1126/science.1163233, [arXiv:0906.3599](#).
- [70] S. Durr et al. Precision computation of the kaon bag parameter. 2011, [arXiv:1106.3230](#).
- [71] David B. Kaplan. A Method for simulating chiral fermions on the lattice. *Phys. Lett.*, B288:342–347, 1992, doi:10.1016/0370-2693(92)91112-M, [arXiv:hep-lat/9206013](#).
- [72] D.B. Kaplan. Chiral fermions on the lattice. *Nucl. Phys. Proc. Suppl.*, 30:597–600, 1993, doi:10.1016/0920-5632(93)90282-B.
- [73] Yigal Shamir. Chiral fermions from lattice boundaries. *Nucl. Phys.*, B406:90–106, 1993, doi:10.1016/0550-3213(93)90162-I, [arXiv:hep-lat/9303005](#).
- [74] Vadim Furman and Yigal Shamir. Axial symmetries in lattice QCD with Kaplan fermions. *Nucl. Phys.*, B439:54–78, 1995, doi:10.1016/0550-3213(95)00031-M, [arXiv:hep-lat/9405004](#).
- [75] Herbert Neuberger. Exactly massless quarks on the lattice. *Phys. Lett.*, B417:141–144, 1998, doi:10.1016/S0370-2693(97)01368-3, [arXiv:hep-lat/9707022](#).
- [76] B. Sheikholeslami and R. Wohlert. Improved Continuum Limit Lattice Action for QCD with Wilson Fermions. *Nucl. Phys.*, B259:572, 1985, doi:10.1016/0550-3213(85)90002-1.
- [77] Roberto Frezzotti, Pietro Antonio Grassi, Stefan Sint, and Peter Weisz, Alpha collaboration. Lattice QCD with a chirally twisted mass term. *JHEP*, 0108:058, 2001, doi:10.1088/1126-6708/2001/08/058, [arXiv:hep-lat/0101001](#).
- [78] Satchidananda Naik. On-shell Improved Lattice Action for QCD with Susskind Fermions and Asymptotic Freedom Scale. *Nucl. Phys.*, B316:238, 1989, doi:10.1016/0550-3213(89)90394-5.

- [79] Kostas Orginos and Doug Toussaint, MILC collaboration. Testing improved actions for dynamical Kogut-Susskind quarks. *Phys. Rev.*, D59:014501, 1999, doi:10.1103/PhysRevD.59.014501, [arXiv:hep-lat/9805009](https://arxiv.org/abs/hep-lat/9805009).
- [80] E. Follana et al., HPQCD. Highly Improved Staggered Quarks on the Lattice, with Applications to Charm Physics. *Phys. Rev.*, D75:054502, 2007, doi:10.1103/PhysRevD.75.054502, [arXiv:hep-lat/0610092](https://arxiv.org/abs/hep-lat/0610092).
- [81] A.Ali Khan, M. Gockeler, Ph. Hagler, T.R. Hemmert, R. Horsley, et al. Axial coupling constant of the nucleon for two flavours of dynamical quarks in finite and infinite volume. *Phys. Rev.*, D74:094508, 2006, doi:10.1103/PhysRevD.74.094508, [arXiv:hep-lat/0603028](https://arxiv.org/abs/hep-lat/0603028).
- [82] D. Pleiter et al., QCDSF/UKQCD Collaboration. Nucleon form factors and structure functions from $N_f = 2$ Clover fermions. *PoS*, LATTICE2010:153, 2010, [arXiv:1101.2326](https://arxiv.org/abs/1101.2326).
- [83] B.B. Brandt, S. Capitani, M. Della Morte, D. Djukanovic, J. Gegelia, et al. Form factors in lattice QCD. 2011, [arXiv:1106.1554](https://arxiv.org/abs/1106.1554).
- [84] C. Alexandrou et al., ETM Collaboration. Axial Nucleon form factors from lattice QCD. *Phys. Rev.*, D83:045010, 2011, doi:10.1103/PhysRevD.83.045010, [arXiv:1012.0857](https://arxiv.org/abs/1012.0857).
- [85] Huey-Wen Lin, Tom Blum, Shigemi Ohta, Shoichi Sasaki, and Takeshi Yamazaki. Nucleon structure with two flavors of dynamical domain-wall fermions. *Phys. Rev.*, D78:014505, 2008, doi:10.1103/PhysRevD.78.014505, [arXiv:0802.0863](https://arxiv.org/abs/0802.0863).
- [86] T. Yamazaki et al., RBC+UKQCD Collaboration. Nucleon axial charge in 2+1 flavor dynamical lattice QCD with domain wall fermions. *Phys. Rev. Lett.*, 100:171602, 2008, doi:10.1103/PhysRevLett.100.171602, [arXiv:0801.4016](https://arxiv.org/abs/0801.4016).
- [87] Yasumichi Aoki, Tom Blum, Huey-Wen Lin, Shigemi Ohta, Shoichi Sasaki, et al. Nucleon isovector structure functions in (2+1)-flavor QCD with domain wall fermions. *Phys. Rev.*, D82:014501, 2010, doi:10.1103/PhysRevD.82.014501, [arXiv:1003.3387](https://arxiv.org/abs/1003.3387).
- [88] R.G. Edwards et al., LHPC Collaboration. The Nucleon axial charge in full lattice QCD. *Phys. Rev. Lett.*, 96:052001, 2006, doi:10.1103/PhysRevLett.96.052001, [arXiv:hep-lat/0510062](https://arxiv.org/abs/hep-lat/0510062).
- [89] R.G. Edwards, G. Fleming, Ph. Hagler, John W. Negele, K. Orginos, et al. Nucleon structure in the chiral regime with domain wall fermions on an improved staggered sea. *PoS*, LAT2006:121, 2006, [arXiv:hep-lat/0610007](https://arxiv.org/abs/hep-lat/0610007).
- [90] J.D. Bratt et al., LHPC Collaboration. Nucleon structure from mixed action calculations using 2+1 flavors of asqtad sea and domain wall valence fermions. *Phys. Rev.*, D82:094502, 2010, doi:10.1103/PhysRevD.82.094502, [arXiv:1001.3620](https://arxiv.org/abs/1001.3620).

- [91] M. Gockeler et al., QCDSF/UKQCD Collaboration. Baryon Axial Charges and Momentum Fractions with $N_f = 2+1$ Dynamical Fermions. *PoS*, LATTICE2010:163, 2010, [arXiv:1102.3407](#).
- [92] Huey-Wen Lin and Saul D. Cohen. Nucleon and Pion Form Factors from $N_f = 2+1$ Anisotropic Lattices. 2011, [arXiv:1104.4319](#).
- [93] G. Martinelli, C. Pittori, Christopher T. Sachrajda, M. Testa, and A. Vladikas. A General method for nonperturbative renormalization of lattice operators. *Nucl. Phys.*, B445:81–108, 1995, doi:10.1016/0550-3213(95)00126-D, [arXiv:hep-lat/9411010](#).
- [94] M. Göckeler et al. Perturbative and Nonperturbative Renormalization in Lattice QCD. *Phys. Rev.*, D82:114511, 2010, doi:10.1103/PhysRevD.82.114511, [arXiv:1003.5756](#).
- [95] Yasumichi Aoki. Non-perturbative renormalization in lattice QCD. *PoS*, LAT2009:012, 2009, [arXiv:1005.2339](#).
- [96] K. Nakamura et al., Particle Data Group. Review of particle physics. *J. Phys.*, G37:075021, 2010, doi:10.1088/0954-3899/37/7A/075021.
- [97] Huey-Wen Lin and Konstantinos Orginos. First Calculation of Hyperon Axial Couplings from Lattice QCD. *Phys. Rev.*, D79:034507, 2009, doi:10.1103/PhysRevD.79.034507, [arXiv:0712.1214](#).
- [98] G.R. Young et al. Scientific grand challenges: forefront questions in nuclear science and the role of computing at the extreme scale, http://extremecomputing.labworks.org/nuclearphysics/PNNL_18739_onlineversion_opt.pdf. Workshop held January 26–28, 2009, sponsored by the U.S. Department of Energy, Office of Nuclear Physics and the Office of Advanced Scientific Computing.
- [99] V.A. Andreev et al., MuCap Collaboration. Measurement of the rate of muon capture in hydrogen gas and determination of the proton’s pseudoscalar coupling g_P . *Phys. Rev. Lett.*, 99:032002, 2007, doi:10.1103/PhysRevLett.99.032002, [arXiv:0704.2072](#).
- [100] Andrzej Czarnecki, William J. Marciano, and Alberto Sirlin. Electroweak radiative corrections to muon capture. *Phys. Rev. Lett.*, 99:032003, 2007, doi:10.1103/PhysRevLett.99.032003, [arXiv:0704.3968](#).
- [101] Veronique Bernard, Latifa Elouadrhiri, and Ulf.G. Meissner. Axial structure of the nucleon: Topical Review. *J. Phys.*, G28:R1–R35, 2002, doi:10.1088/0954-3899/28/1/201, [arXiv:hep-ph/0107088](#).
- [102] Tim Gorringe and Harold W. Fearing. Induced pseudoscalar coupling of the proton weak interaction. *Rev. Mod. Phys.*, 76:31–91, 2004, doi:10.1103/RevModPhys.76.31, [arXiv:nucl-th/0206039](#).

- [103] G. Jonkmans, S. Ahmad, D.S. Armstrong, G. Azuelos, Wilhelm H. Bertl, et al. Radiative muon capture on hydrogen and the induced pseudoscalar coupling. *Phys. Rev. Lett.*, 77:4512–4515, 1996, doi:10.1103/PhysRevLett.77.4512, arXiv:nucl-ex/9608005.
- [104] J.H.D. Clark, D.S. Armstrong, T.P. Gorrige, M.D. Hasinoff, P.M. King, et al. Ortho-para transition rate in mu-molecular hydrogen and the proton’s induced pseudoscalar coupling g_P . *Phys. Rev. Lett.*, 96:073401, 2006, doi:10.1103/PhysRevLett.96.073401, arXiv:nucl-ex/0509025.
- [105] Shoichi Sasaki, Kostas Orginos, Shigemi Ohta, and Tom Blum, the RIKEN-BNL-Columbia-KEK Collaboration. Nucleon axial charge from quenched lattice QCD with domain wall fermions. *Phys. Rev.*, D68:054509, 2003, doi:10.1103/PhysRevD.68.054509, arXiv:hep-lat/0306007.
- [106] Takeshi Yamazaki, Yasumichi Aoki, Tom Blum, Huey-Wen Lin, Shigemi Ohta, et al. Nucleon form factors with 2+1 flavor dynamical domain-wall fermions. *Phys. Rev.*, D79:114505, 2009, doi:10.1103/PhysRevD.79.114505, arXiv:0904.2039.
- [107] M. Anselmino, M. Boglione, U. D’Alesio, A. Kotzinian, F. Murgia, et al. Update on transversity and Collins functions from SIDIS and e^+e^- data. *Nucl. Phys. Proc. Suppl.*, 191:98–107, 2009, doi:10.1016/j.nuclphysbps.2009.03.117, arXiv:0812.4366.
- [108] M. Alekseev et al., COMPASS Collaboration. Collins and Sivers asymmetries for pions and kaons in muon-deuteron DIS. *Phys. Lett.*, B673:127–135, 2009, doi:10.1016/j.physletb.2009.01.060, arXiv:0802.2160.
- [109] Markus Diefenthaler, HERMES Collaboration. HERMES measurements of Collins and Sivers asymmetries from a transversely polarised hydrogen target. pages 579–582, 2007, arXiv:0706.2242.
- [110] R. Seidl et al., Belle Collaboration. Measurement of Azimuthal Asymmetries in Inclusive Production of Hadron Pairs in e^+e^- Annihilation at $\sqrt{s} = 10.58$ GeV. *Phys. Rev.*, D78:032011, 2008, doi:10.1103/PhysRevD.78.032011, arXiv:0805.2975.
- [111] I.C. Cloet, Wolfgang Bentz, and Anthony William Thomas. Transversity quark distributions in a covariant quark-diquark model. *Phys. Lett.*, B659:214–220, 2008, doi:10.1016/j.physletb.2007.09.071, arXiv:0708.3246.
- [112] M. Wakamatsu. Comparative analysis of the transversities and the longitudinally polarized distribution functions of the nucleon. *Phys. Lett.*, B653:398–403, 2007, doi:10.1016/j.physletb.2007.08.013, arXiv:0705.2917.
- [113] Han-xin He and Xiang-Dong Ji. The Nucleon’s tensor charge. *Phys. Rev.*, D52:2960–2963, 1995, doi:10.1103/PhysRevD.52.2960, arXiv:hep-ph/9412235.
- [114] M. Gockeler et al., QCDSF Collaboration, UKQCD Collaboration. Quark helicity flip generalized parton distributions from two-flavor lattice QCD. *Phys. Lett.*, B627:113–123, 2005, doi:10.1016/j.physletb.2005.09.002, arXiv:hep-lat/0507001.

- [115] William Detmold, W. Melnitchouk, John W. Negele, Dru Bryant Renner, and Anthony William Thomas. Chiral extrapolation of lattice moments of proton quark distributions. *Phys. Rev. Lett.*, 87:172001, 2001, doi:10.1103/PhysRevLett.87.172001, [arXiv:hep-lat/0103006](https://arxiv.org/abs/hep-lat/0103006).
- [116] William Detmold, W. Melnitchouk, and Anthony William Thomas. Moments of isovector quark distributions from lattice QCD. *Phys. Rev.*, D66:054501, 2002, doi:10.1103/PhysRevD.66.054501, [arXiv:hep-lat/0206001](https://arxiv.org/abs/hep-lat/0206001).
- [117] Stephen L. Adler, E.W. Colglazier Jr., J.B. Healy, Inga Karliner, Judy Lieberman, et al. Renormalization Constants for Scalar, Pseudoscalar, and Tensor Currents. *Phys. Rev.*, D11:3309, 1975, doi:10.1103/PhysRevD.11.3309.
- [118] Robert G. Edwards, Balint Joo, and Huey-Wen Lin. Tuning for Three-flavors of Anisotropic Clover Fermions with Stout-link Smearing. *Phys. Rev.*, D78:054501, 2008, doi:10.1103/PhysRevD.78.054501, [arXiv:0803.3960](https://arxiv.org/abs/0803.3960).
- [119] Huey-Wen Lin et al., Hadron Spectrum Collaboration. First results from 2+1 dynamical quark flavors on an anisotropic lattice: Light-hadron spectroscopy and setting the strange-quark mass. *Phys. Rev.*, D79:034502, 2009, doi:10.1103/PhysRevD.79.034502, [arXiv:0810.3588](https://arxiv.org/abs/0810.3588).
- [120] Y. Aoki et al., RBC. Continuum Limit Physics from 2+1 Flavor Domain Wall QCD. *Phys. Rev.*, D83:074508, 2011, doi:10.1103/PhysRevD.83.074508, [arXiv:1011.0892](https://arxiv.org/abs/1011.0892).
- [121] J. Charles et al., CKMfitter Group. CP violation and the CKM matrix: Assessing the impact of the asymmetric B factories. *Eur. Phys. J.*, C41:1–131, 2005, doi:10.1140/epjc/s2005-02169-1, [arXiv:hep-ph/0406184](https://arxiv.org/abs/hep-ph/0406184).
- [122] F. Abe et al., CDF Collaboration. Limits on quark-lepton compositeness scales from dileptons produced in 1.8 TeV $p\bar{p}$ collisions. *Phys. Rev. Lett.*, 79:2198–2203, 1997, doi:10.1103/PhysRevLett.79.2198.
- [123] Vardan Khachatryan et al., CMS. Search for Quark Compositeness with the Dijet Centrality Ratio in pp Collisions at $\sqrt{s} = 7$ TeV. *Phys. Rev. Lett.*, 105:262001, 2010, doi:10.1103/PhysRevLett.105.262001, [arXiv:1010.4439](https://arxiv.org/abs/1010.4439).
- [124] Georges Aad et al., ATLAS. Search for New Physics in Dijet Mass and Angular Distributions in pp Collisions at $\sqrt{s} = 7$ TeV Measured with the ATLAS Detector. *New J. Phys.*, 13:053044, 2011, doi:10.1088/1367-2630/13/5/053044, [arXiv:1103.3864](https://arxiv.org/abs/1103.3864).
- [125] Vardan Khachatryan et al., CMS. Measurement of Dijet Angular Distributions and Search for Quark Compositeness in pp Collisions at 7 TeV. *Phys. Rev. Lett.*, 106:201804, 2011, doi:10.1103/PhysRevLett.106.201804, [arXiv:1102.2020](https://arxiv.org/abs/1102.2020).
- [126] Georges Aad et al., ATLAS. Search for Contact Interactions in Dimuon Events from pp Collisions at $\sqrt{s} = 7$ TeV with the ATLAS Detector. 2011, [arXiv:1104.4398](https://arxiv.org/abs/1104.4398).

- [127] David J. Broadhurst and A.G. Grozin. Matching QCD and HQET heavy - light currents at two loops and beyond. *Phys. Rev.*, D52:4082–4098, 1995, doi:10.1103/PhysRevD.52.4082, [arXiv:hep-ph/9410240](https://arxiv.org/abs/hep-ph/9410240).
- [128] R.K. Ellis, W.J. Stirling, and B.R. Webber. *QCD and Collider Physics*. Cambridge Monographs on Particle Physics, Nuclear Physics and Cosmology. Cambridge University Press, 2003.
- [129] Georges Aad et al., ATLAS. Search for a heavy gauge boson decaying to a charged lepton and a neutrino in 1 fb^{-1} of pp collisions at $\sqrt{s} = 7 \text{ TeV}$ using the ATLAS detector. 2011, [arXiv:1108.1316](https://arxiv.org/abs/1108.1316).
- [130] Vardan Khachatryan et al., CMS Collaboration. Search for W' in the leptonic channels in pp Collisions at $\sqrt{s} = 7 \text{ TeV}$, <http://cdsweb.cern.ch/record/1369201>. CERN Report number CMS-PAS-EXO-11-024, 2011.
- [131] Vardan Khachatryan et al., CMS Collaboration. Search for a heavy gauge boson W' in the final state with an electron and large missing transverse energy in pp collisions at $\sqrt{s} = 7 \text{ TeV}$. *Phys. Lett.*, B698:21–39, 2011, doi:10.1016/j.physletb.2011.02.048, [arXiv:1012.5945](https://arxiv.org/abs/1012.5945).
- [132] A. D. Martin, W. J. Stirling, R. S. Thorne, and G. Watt. Parton distributions for the LHC. *Eur. Phys. J.*, C63:189–285, 2009, doi:10.1140/epjc/s10052-009-1072-5, [arXiv:0901.0002](https://arxiv.org/abs/0901.0002).
- [133] J. Pumplin, D.R. Stump, J. Huston, H.L. Lai, Pavel M. Nadolsky, et al. New generation of parton distributions with uncertainties from global QCD analysis. *JHEP*, 0207:012, 2002, doi:10.1088/1126-6708/2002/07/012, [arXiv:hep-ph/0201195](https://arxiv.org/abs/hep-ph/0201195).